A DIVE INTO THE SKELETAL MUSCLE METABOLIC AND FUNCTIONAL ENVIRONMENT

AN INVESTIGATION OF THE SKELETAL MUSCLE METABOLIC AND FUNCTIONAL WINDOW: A MULTIMODAL NON-INVASIVE APPROACH USING ^{1}H MAGNETIC RESONANCE SPECTROSCOPY (^{1}H-MRS), MAGNETIZATION TRANSFER (MT) AND BLOOD OXYGEN LEVEL DEPENDENT (BOLD) SIGNAL

By ALEJANDRO AMADOR-TEJADA, B.A.Sc. Biomedical Physics

A Thesis Submitted to the School of Graduate Studies in Partial Fulfillment
of the Requirements for
the Degree Master's of Applied Science in Biomedical Engineering

McMaster University

Master's of Applied Science in Biomedical Engineering (2023)

Hamilton, ON, Canada (School of Biomedical Engineering)

TITLE:	An investigation of the skeletal muscle metabolic and functional window: a multimodal non-invasive approach using ^{1}H Magnetic Resonance Spectroscopy (^{1}H-MRS), Magnetization Transfer (MT) and Blood Oxygen Level Dependent (BOLD) signal
AUTHOR:	Alejandro Amador-Tejada B.A.Sc. (Biomedical Physics), National Autonomous University of Mexico, Mexico City, Mexico
SUPERVISOR:	Dr. Michael D. Noseworthy
EXAMINERS:	Dr. Hubert de Bruin, Dr. Dinesh Kumbhare
NUMBER OF PAGES:	1, 146

Lay Abstract

Skeletal muscle performs vital functions such as movement, heat generation, and posture. The impact of musculoskeletal disorders, which can disrupt these functions and cause temporary or permanent impairment of physical activity and movement, is expected to grow in the future. Correctly characterizing healthy or ‘normal’ skeletal muscle is necessary to identify diseased or injured skeletal muscle, as most muscle abnormalities cause changes in morphology and physiology. Non-invasive Magnetic Resonance Imaging techniques to assess the biochemical environment, water dynamics, blood flow and relative (de)oxy-Hb concentration have yet to be extensively explored in healthy skeletal muscle. Thus, the primary purpose of this thesis was to investigate, characterize and provide unique metrics to study the functional and metabolic profile of healthy skeletal muscle at rest and during exercise. The metrics investigated can be used to establish a baseline to detect abnormal skeletal muscle.

Abstract

Skeletal muscle performs essential functions, including movement and posture. Musculoskeletal disorders can disrupt these functions, leading to temporary or permanent impairment. As most muscle abnormalities will cause morphological and physiological changes in skeletal muscle, identifying diseased or injured skeletal muscle relies on having a frame of reference, *i.e.* a correct characterization of what is considered healthy or 'normal' skeletal muscle.

Non-invasive MRI techniques such as ^{1}H Magnetic Resonance Spectroscopy (MRS) to assess the biochemical environment, Magnetization Transfer (MT) to study water dynamics and Blood Oxygen Level Dependent (BOLD) signal to study blood flow and relative (de)oxy-Hb concentration have yet to be extensively explored in skeletal muscle. Therefore, to improve the knowledge of the biochemical environment of skeletal muscle, a series of experiments were performed using these techniques in calf muscles.

^{1}H-MRS investigations showed high repeatability of metabolite quantification within and across scanning sessions despite its challenges due to the high structural organization of skeletal muscle. Furthermore, differences in the metabolic profile between endurance vs. power-oriented participants at rest were found, suggesting ^{1}H-MRS could be used as a non-invasive technique to assess muscle fiber composition.

A multimodal MT, and BOLD study were performed on exercised skeletal muscle to complement the metabolic understanding of skeletal muscle. It was shown that high-quality data could be obtained in simultaneous studies of BOLD/EMG. In addition, during a multimodal MT and BOLD acquisition, MT signal showed a decrease after exercise and was linearly correlated to the BOLD signal activation. The ability of MT to distinguish between highly/lowly activated muscle groups during exercise opens the opportunity to non-invasively investigate muscle group recruitment with a higher spatial resolution compared to EMG, and lower scanning times compared to BOLD.

Overall, the main purpose of this thesis was to investigate, characterize and provide unique metrics to study the functional and metabolic profile of healthy skeletal muscle at rest and during exercise.

To my family

Acknowledgements

There are several people that, without them, this thesis would not have been possible. I want to start with my supervisor, Dr. Michael D. Noseworthy. I'm grateful for all your expertise, guidance, and support, not only through the development of this thesis but also through my process of arriving, adapting and living in Canada. I would like to thank Dr. Huibregt de Bruin and Dr. Dinesh Kumbhare as well, for your great guidance and expertise, and for taking some of your valuable time to help me through several steps of this thesis.

Next, I would like to thank all the support received from the staff at St. Joseph's Healthcare Hamilton. Starting with Shannon, Julie, Carol, and Suzanne, thanks for all the time you put in me, to train and supervise me to be able to run the MRI. Thanks for all the advice and recommendations that saved me so much time, and thanks for all the company and candies provided during those long scans. Thanks, Norm, for always being available to answer any questions or help me with my experiments.

I would like to thank my lab partners in Dr. Noseworthy's lab, for volunteering with all those long scans, and for your constant advice during my experiments. A special thanks to Cameron Nowikow, and Ethan Danielli for all your help and support through these 2 years. An even special thanks to Thaejaesh Sooriyakumaran and Joshua McGillivray for spending so much time putting all those experiments together, for all the support, for all those long nights working on the extremely reliable MRI system, and for all those amazing memories from ISMRM 2022. Joshua McGillivray, I want to thank you for being there when I needed it the most, I couldn't have asked for a better friend than you.

I would like to thank my support system that kept me pointing in the right direction. To my mom Liliana and my dad Rolando, who helped me through the adaptation process to this new country. I can not thank you enough for all the effort you made so that I could be where I am now. To Elyse, who watched me and dealt with my suffering through this work, and who supported me in so many ways, thanks.

Contents

List of Figures

List of Tables

List of Acronyms

AAS average artifact subtraction.
ACh Acetylcholine.
ADP Adenosine diphosphate.
ANCOVA Analysis of Covariance.
ANOVA Analysis of Variance.
ATP Adenosine triphosphate.

BMS Bulk Magnetic Susceptibility.
BOLD Blood Oxygen Level Dependent.

Car Carnosine.
CBF cerebral blood flow.
CBV cerebral blood volume.
Cho Choline.
CMRO2 cerebral metabolic rate of oxygen.
Cr Creatine.
CSA cross-sectional area.

DMD Duchenne Muscular Dystrophy.
DTI Diffusion Tensor Imaging.

EDL extensor digitorum longus.
EEG Electroencephalography.
EMCL extramyocellular lipids.
EMG Electromyography.
EMS Electrical Muscle Stimulation.
EPI Echo Planar Imaging.

FIESTA Fast Imaging Employing Steady-state Acquisition.
fMRI Functional Magnetic Resonance Imaging.
FWHM Full Width at Half Maximum.

GA gradient artifact.
GL gastrocnemius lateralis.
GM gastrocnemius medialis.

HRF Hemodynamic Response Function.

IMCL intramyocellular lipids.

MAP Muscle Action Potentials.
MPS Motor Point Stimulation.
MRI Magnetic Resonance Imaging.
MRS Magnetic Resonance Spectroscopy.
MS Multiple Sclerosis.
MSK Musculoskeletal.
MT Magnetization Transfer.
MVC Maximum Voluntary Contraction.

NBR Negative BOLD response.
NMJ Neuromuscular Junctions.
NMR Nuclear Magnetic Resonance.

OEF oxygen extraction fraction.

PCr Phosphocreatine.
PL peroneus longus.
PNS Peripheral Nerve Stimulation.
PRESS Point-Resolved Spectroscopy.

RMS root mean square.

SAR specific absorption rate.
SNR Signal-to-noise ratio.
SOL soleus.

TA tibialis anterior.
Tau Taurine.
TMA Trimethylamine complex.
TP tibialis posterior.

US Ultrasound.

VOI voxel of interest.

Introduction

Skeletal muscle is an essential tissue, as it performs a wide range of functions and activities in the human body, such as body movement, posture, joint stabilization, and heat generation. Skeletal muscle accounts for ∼40% of total body mass and consumes around ∼30% of the total available energy in the human body. Water is the main component of skeletal muscle, accounting for nearly 75% of its total mass, while the rest is composed of proteins (∼20%) and smaller amounts of fat, minerals and carbohydrates [1–4].

Skeletal muscle plays a critical role in many aspects of human life, and any damage or impairment to this tissue can significantly impact the quality of life of individuals. Musculoskeletal (MSK) disorders are common, exist globally, and contribute substantially to rates of disability and morbidity [5]. The number of individuals with MSK disorders increased worldwide by 58% between 1990 and 2017 [6], and in 2021, they were estimated to affect around 1.7 billion people [7]. Even though these conditions typically are not lethal, their prevalence and levels of induced disability are high [8], making them a significant public health concern. Over the past two decades, reports from Canada have indicated a rise in the number of individuals experiencing MSK disorders, which has resulted in significant health and economic challenges [9, 10].

The musculoskeletal system is responsible for providing the body with support, stability, and mobility. When affected by a musculoskeletal disorder, these functions can be disrupted, leading to temporary or permanent impairment of physical activity and movement like walking or standing up, which impacts the social, economic and health aspects of the individual [10], and ultimately, decrease the quality of life. MSK disorders are one of the top worldwide problems in individuals [11], having a higher incidence in elderly people. MSK disorders and their impacts are expected to keep increasing in the future [6], as the elderly population (65+ years old) is projected to grow to 1.6 billion by 2050 [12], causing a considerable burden to the health and social care systems [11, 13].

It is evident that MSK disorders are of significant concern, and they are expected to persist as society ages. To reduce the burden, a correct and early diagnosis is essential for effectively managing and treating these diseases [5]. An early diagnosis would help to slow or stop the progression of the disease, minimizing possible complications and overall increasing the likelihood of a good prognosis. The conventional diagnosis and follow-up for MSK disorders often consist of clinical examinations, blood samples, and electrophysiological and laboratory tests. Nevertheless, these disorders are easily confused and underestimated due to their vague symptoms, such as myalgia, weakness, and fatigue, thus requiring the use of biopsies as a diagnostic procedure [14]. Biopsies have been the gold standard to assess skeletal muscle since the early 1970s [15–17], nevertheless, it is an invasive technique that causes relative discomfort to the patient such as minor pain and stiffness, it is a sampling variant method, it can not be repeated often, and provides a localized rather than a global picture of the target muscle [18]. In addition, to monitor and follow up with patients, several biopsies from the diseased muscle would be required, increasing the chances of developing inflammatory reactions or muscle damage [18].

There are several classifications of MSK diseases, including muscle dystrophies and atrophies, inflammatory myopathies, neuromuscular joint diseases and metabolic diseases [19]. Regardless of the classification, myopathic-derived diseases are caused by defects of the muscle fibers, either acquired or inherited [18]. For instance, muscle dystrophies are a group of diseases mainly characterized by the progressive loss of muscle mass and strength, an example is Duchenne Muscular Dystrophy (DMD), which is clinically characterized by a decrease in the presence of type II fibers [20]. Another example is metabolic myopathies related to glucose metabolism affecting either glycolysis, glycogenolysis or glycogen synthesis [21]. The symptoms vary depending on the affected enzyme but can range from muscle weakness to exercise-induced discomfort.

The use of imaging methods to boost the diagnosis of these disorders has been proven effective, having as advantages their non-invasive nature, their ability to obtain quantitative data and provide not only anatomical but also metabolic, functional, and structural information of muscle tissue. Magnetic Resonance Imaging (MRI) methods provide excellent tissue contrast allowing the differentiation between muscle, bone, fat, and connective tissue. These make MRI suitable for studying muscle diseases such as muscle infarction, metastases, and metabolic myopathies [22]. Furthermore, MRI has gained recognition as a valuable tool for investigating neuromuscular diseases affecting skeletal muscles. Its objective and quantitative measurements can serve as biomarkers in clinical trials of novel therapies [23].

Sports medicine is another field that is interested in studying skeletal muscle. The majority of muscle injuries are sports-related, and around 40% of them are soft-tissue related [24]. Muscle injuries often increase the probability of physical incapacity, posing a challenge to healthcare and sports medicine [25]. Furthermore, as the role of skeletal muscle is to produce movement and force to complete daily life tasks, any physical work can result in injury [26]. The severity of a muscle injury can vary: from mild bruises causing little discomfort and virtually no muscle strength lost (grade I), moderate sprains causing a palpable muscle defect with mild loss of function (grade II), to severe injuries causing loss of muscle movement and ability to contract (grade III) [24, 26, 27]. The typical diagnosis and grading of muscle injury are based on the clinical history and physical examination, but this only covers the superficial part of the lesion, leaving unexamined deeper regions. Ultrasound (US) is the first alternative to assess these areas, having the advantage of being non-invasive and a real-time modality, but its main drawback is that it is operator-dependent [28].

Overall, MRI have had an important role in the diagnosing and monitoring MSK diseases and injuries. For instance, MRI T_1 and T_2-weighted images have been used primarily to assess muscle structural damage, fat infiltration, inflammation, denervation, and relative water content [29]. Special MRI techniques such as Diffusion Tensor Imaging (DTI) have been used to assess the severity in DMD [30]. Additionally, ^{31}P Magnetic Resonance Spectroscopy (MRS) has been used to assess muscle metabolism during the characterization, diagnosis, and treatment of metabolic myopathies and has been extensively used [31], such as Postpoliomyelitis syndrome (PPS), DMD, and Werdnig-Hoffmann disease [32], or metabolic diseases related to glucose metabolism [33], nevertheless the translation of ^{31}P MRS to clinical settings is hampered due to the extensive and expensive hardware required to perform MRS of this nuclei.

Altogether, the early diagnosis, correct characterization, treatment monitoring, and follow-up of MSK diseases and injuries play a vital role in increasing the probabilities of a positive prognosis, enabling the early and safe return of patients to their regular activities [14]. As the majority of muscle abnormalities will cause morphological and physiological changes in skeletal muscle, the ability to identify diseased or injured skeletal muscle relies on having a frame of reference, *i.e.* a correct characterization of what is considered healthy or 'normal' skeletal muscle. Furthermore, healthy skeletal muscle is itself a matter of interest because it shows high plasticity, *i.e.* it can adapt to external demands such as exercise training, changing its architecture, relative fiber composition, and length [34].

1.1 Objective

So far, MRI has taken the role of 'static' (*i.e.* structural, no dynamic information) imaging method to diagnose MSK disorders and injuries. Inherently, there are additional non-invasive specialized MRI sequences that can provide further functional information on skeletal muscle, such as (1) ^{1}H Magnetic Resonance Spectroscopy (^{1}H-MRS), a technique to assess the biochemical environment, (2) Blood Oxygen Level Dependent (BOLD), a functional MRI contrast technique used to measure the changes in blood flow and relative oxygenation in tissues or (3) Magnetization Transfer (MT), an MRI technique whose contrast is generated through the exchange of protons between free or highly mobile and bound (to macromolecules) or highly restricted water molecules.

Skeletal muscle is composed of heterogeneous fiber groups: type I and type II, showing different metabolic, contraction speed and resistance characteristics [34–36]. These characteristics will give different properties to each muscle group. Therefore, it is hypothesized that functional approaches to studying skeletal muscle could provide new discriminators to differentiate between healthy vs. diseased skeletal muscle and between different muscle groups within the same extremity. Even more, it is hypothesized that exercise would increase these differences, as these muscle groups have a preferred type of exercise (*i.e.* endurance or power oriented).

The *general objective* of this M.A.Sc. thesis is to investigate and characterize the functional and metabolic profile of healthy skeletal muscle by looking at its (1) biochemical environment using ^{1}H-MRS, (2) water dynamics between the free and bounded pools by means of MT, and (3) blood flow and relative oxygen concentration using BOLD. The use of these techniques will provide a dynamic and functional profile of skeletal muscle that can complement the overall understanding of healthy skeletal muscle. Naturally, as the understanding of the frame of reference increases, the ability to identify and diagnose diseased skeletal muscle would be improved, overall increasing the diagnosis power of MSK disorders and injuries.

1.2 Thesis structure

The format of this document is a 'sandwich' thesis composed of 5 main research chapters, all of which are presented in a sequential manner that describes the train of experiments and ideas during the last two years. All of the research chapters were written as a research paper, including background, methods, results, discussion and limitations sections. This was done in order to simplify the future publication process. Any additional material required, such as code, was appended at the end of each research chapter, as well as its references. An overview and the specific object of each chapter are stated below.

Chapter 1 Introduction: this chapter presents the global motivation, structure, and objectives of this thesis.

Chapter 2 Background: this chapter provides the basic knowledge and explains the topics that are necessary to understand the following thesis.

Chapter 3 General Methods: this chapter introduces the general methods of this thesis. Since the focus of this thesis is on novel MRI data analysis, there is a large overlap in data collection and analysis techniques found in the 5 main research chapters. As a result, to avoid repetition, all of this shared information was condensed in this chapter. Any additional methodology required by the following experiments was added in its corresponding methodology section.

Chapter 4 Skeletal muscle proton spectroscopy quantification: a repeatability analysis: the first research chapter; a study on muscle ^{1}H-MRS repeatability. ^{1}H-MRS is one of the primary MRI techniques used in this thesis to study skeletal muscle. In contrast to ^{31}P-MRS, it has not been as well studied in muscle, so a repeatability study needed to be completed to determine the validity of the future ^{1}H-MRS investigations. Specifically, ^{1}H-MRS metabolite quantification presents challenges due to the highly structured arrangement of muscle fibres. Therefore, the objective of this chapter was to assess the repeatability of ^{1}H-MRS metabolite quantification within and across scanning sessions.

Chapter 5 An examination of the fiber composition of skeletal muscle using proton spectroscopy: the second research chapter; a study on the metabolic characteristics of muscle using ^{1}H-MRS. The skeletal muscle of the lower leg is composed of multiple muscle groups that show different metabolic and contractile characteristics. The most common method to study these characteristics is muscle biopsy, but its main disadvantage is that it is an invasive technique. Furthermore, the global metabolic characterization of skeletal muscle between predominantly endurance vs. power athletes has not been performed yet. As such, the aim of this chapter was to study the metabolic profile of the calf muscles between power/strength vs endurance participants by means of ^{1}H-MRS.

Chapter 6 An investigation of electrical stimulation exercise and its effects on metabolic changes by means of proton spectroscopy in healthy skeletal muscle: the third research chapter; a study of muscle metabolism using externally regulated muscle contraction. The study of skeletal muscle using ^{1}H-MRS during exercise is of high interest because it provides information on the dynamics of the biochemical environment. This information could be useful in identifying diseases that impair metabolic functions in skeletal muscle. Previous ^{1}H-MRS studies typically employed exercises that were highly demanding, hard to standardize the level of effort, and most of them required the subject to leave the MRI for the exercise course. Neuromuscular electrical stimulation could be an alternative, as it provides more control over the exercise and could be used to elicit muscle contraction in diseased populations who have poor muscle control/strength. Consequently, the objective of this chapter was to assess the effect of electrical stimulation exercise on the metabolic profile of the lower leg.

Chapter 7 Simultaneous Studies of Muscle Blood Oxygen Level Dependent Signal and Electromyography: a safety and quality assessment analysis: the fourth research chapter; a study of functional activation of muscle using a non-invasive multi-modal technique. An alternative to studying skeletal muscle metabolism is the use of the BOLD signal. Through this MRI technique, it is possible to indirectly evaluate muscle region activation by analyzing changes in metabolism and blood oxygenation levels. A complementary technique to assess muscle activation is electromyography, a well-established technique used to measure the electrical activity of skeletal muscle. The integration of these two techniques would be beneficial as they would simultaneously provide electrophysiological and functional skeletal muscle activation. Nevertheless, simultaneous acquisitions of BOLD/EMG have safety and quality concerns as both techniques can interfere with each other. Hence, the purpose of this chapter was to assess the safety of using EMG hardware inside the MRI environment and to evaluate the performance of a filter to denoise the EMG signal contaminated with the gradient artifact.

Chapter 8 Skeletal muscle metabolism assessment: a multimodal approach to understand water dynamics using Magnetization Transfer and muscle activation using Blood Oxygen Level Dependent Signal: the fifth and last research chapter; a study of fluids within the muscle and their dynamic change with exercise. Muscle metabolism, including ATP use or resynthesis (*i.e.* aerobic or anaerobic), involves several reactants (such as water, PCr, and glucose) and products (including ATP, ADP, and P_i). The typical method of studying these reactions is using spectroscopy, which has been explored in depth above, by looking at the evolution over time of metabolites such as ATP, inorganic phosphate, and creatine, among others. Nevertheless, spectroscopy is only half of the metabolic picture, tracking water and its movements presents a challenge due to the interaction between free water molecules and water molecules that are bound to macromolecules, *i.e.* free and bound water pools. Thus, MT is an MRI technique that was used to study water dynamics during skeletal muscle activation to complement the research in the previous chapters. BOLD, which looks at the changes in (de)oxyhemoglobin during muscle activation, also provides insight into muscle metabolism, so it was likewise explored. Therefore, the objective of this chapter was to study the water dynamics in skeletal muscle by means of MT. In addition, the MT was correlated to BOLD response to gather more comprehensive information on muscle activation.

Chapter 9 Discussion: the last chapter; an overview of the work covered in this thesis. This chapter covers the overall discussion of the presented work. The key takeaways of each research chapter are condensed, showing the sequential logic between all chapters. This chapter concluded with future research, clinical implications and the overall limitations of this thesis.

References

1. Yamada, Y. *et al.* Extracellular Water May Mask Actual Muscle Atrophy During Aging. *The Journals Gerontol. Ser. A* **65A,** 510–516. doi:`10.1093/gerona/glq001` (May 1, 2010).
2. Yamada, Y. *et al.* The Extracellular to Intracellular Water Ratio in Upper Legs is Negatively Associated With Skeletal Muscle Strength and Gait Speed in Older People. *The Journals Gerontol. Ser. A* **72,** 293–298. doi:`10.1093/gerona/glw125` (Mar. 1, 2017).
3. Lorenzo, I., Serra-Prat, M. & Yébenes, J. C. The Role of Water Homeostasis in Muscle Function and Frailty: A Review. *Nutrients* **11,** 1857. doi:`10.3390/nu11081857` (Aug. 2019).
4. Frontera, W. R. & Ochala, J. Skeletal Muscle: A Brief Review of Structure and Function. *Calcif. Tissue Int.* **96,** 183–195. doi:`10.1007/s00223-014-9915-y` (Mar. 1, 2015).
5. Vilella, R. C. & Reddivari, A. K. R. in *StatPearls* (StatPearls Publishing, Treasure Island (FL), 2022).
6. Jin, Z. *et al.* Incidence trend of five common musculoskeletal disorders from 1990 to 2017 at the global, regional and national level: results from the global burden of disease study 2017. *Ann. Rheum. Dis.* **79,** 1014–1022. doi:`10.1136/annrheumdis-2020-217050` (Aug. 2020).
7. (WHO), W. H. O. *Musculoskeletal conditions* Musculoskeletal conditions. `https://www.who.int/news-room/fact-sheets/detail/musculoskeletal-conditions` (2021).
8. Sebbag, E. *et al.* The worldwide burden of musculoskeletal diseases: a systematic analysis of the World Health Organization Burden of Diseases Database. *Ann. Rheum. Dis.* **78,** 844–848. doi:`10.1136/annrheumdis-2019-215142` (June 1, 2019).
9. Coyte, P. C. *et al.* The economic cost of musculoskeletal disorders in Canada. *Arthritis & Rheum.* **11,** 315–325. doi:`10.1002/art.1790110503` (1998).
10. Murphy, K. *et al.* *Health state descriptions for Canadians: musculoskeletal* (Statistics Canada, 2006).
11. Lewis, R. *et al.* Strategies for optimising musculoskeletal health in the 21st century. *BMC musculoskeletal disorders* **20,** 164. doi:`10.1186/s12891-019-2510-7` (Apr. 11, 2019).
12. Of Health (NIH), N. I. *World's older population grows dramatically* World's older population grows dramatically. `https://www.nih.gov/news-events/news-releases/worlds-older-population-grows-dramatically` (2021).
13. Briggs, A. M. *et al.* Musculoskeletal Health Conditions Represent a Global Threat to Healthy Aging: A Report for the 2015 World Health Organization World Report on Ageing and Health. *The Gerontol.* **56,** S243–S255. doi:`10.1093/geront/gnw002` (Suppl_2 Apr. 1, 2016).
14. Theodorou, D. J., Theodorou, S. J. & Kakitsubata, Y. Skeletal muscle disease: patterns of MRI appearances. *The Br. J. Radiol.* **85,** e1298–e1308. doi:`10.1259/bjr/14063641` (Dec. 1, 2012).
15. Baguet, A. *et al.* A New Method for Non-Invasive Estimation of Human Muscle Fiber Type Composition. *PLoS ONE* **6,** e21956. doi:`10/fvmm6p` (July 7, 2011).
16. Sattin, W., Mareci, T. H. & Scott, K. N. Exploiting the stimulated echo in nuclear magnetic resonance imaging. I. Method. *J. Magn. Reson. (1969)* **64,** 177–182. doi:`10.1016/0022-2364(85)90049-6` (Aug. 1, 1985).
17. Karp, J. R. Muscle Fiber Types and Training. *Strength & Cond. J.* **23,** 21. doi:`10.1519/00126548-200110000-00004` (Oct. 2001).
18. Ekblom, B. The muscle biopsy technique. Historical and methodological considerations. *Scand. J. Med. & Sci. Sports* **27,** 458–461. doi:`10.1111/sms.12808` (2017).
19. University, T. J. H. *Types of Muscular Dystrophy and Neuromuscular Diseases* `https://www.hopkinsmedicine.org/health/conditions-and-diseases/types-of-muscular-dystrophy-and-neuromuscular-diseases` (2023).
20. Talbot, J. & Maves, L. Skeletal muscle fiber type: using insights from muscle developmental biology to dissect targets for susceptibility and resistance to muscle disease. *WIREs Dev. Biol.* **5,** 518–534. doi:`10.1002/wdev.230` (July 1, 2016).
21. Tarnopolsky, M. A. Myopathies Related to Glycogen Metabolism Disorders. *Neurotherapeutics* **15,** 915–927. doi:`10.1007/s13311-018-00684-2` (Oct. 1, 2018).
22. Olsen, N. J., Qi, J. & Park, J. H. Imaging and skeletal muscle disease. *Curr. Rheumatol. Reports* **7,** 106–114. doi:`10.1007/s11926-005-0062-3` (Apr. 1, 2005).
23. Sinclair, C. D. J. *et al.* Quantitative magnetization transfer in in vivo healthy human skeletal muscle at 3 T. *Magn. Reson. Med.* **64,** 1739–1748. doi:`10.1002/mrm.22562` (2010).
24. Fernandes, T. L., Pedrinelli, A. & Hernandez, A. J. Muscle injury – physiopathology, diagnosis, treatment and clinical presentation. *Revista Brasileira de Ortopedia* **46,** 247–255. doi:`10.1016/S2255-4971(15)30190-7` (Dec. 8, 2015).

25. Baoge, L. *et al.* Treatment of Skeletal Muscle Injury: A Review. *Int. Sch. Res. Notices* **2012,** e689012. doi:`10.5402/2012/689012` (Apr. 26, 2012).
26. McGillivray, J. E. *et al.* The Effect of Exercise on Neural Activation and Cognition: A Review of Task-Based fMRI Studies. *Crit. Rev. Biomed. Eng.* **49.** doi:`10.1615/CritRevBiomedEng.2021038975` (2021).
27. Noonan, T. J. & Garrett, W. E. J. Muscle Strain Injury: Diagnosis and Treatment. *JAAOS - J. Am. Acad. Orthop. Surg.* **7,** 262. doi:`10.5435/00124635-199907000-00006` (Aug. 1999).
28. Clevert, D.-A. *et al.* Position statement and best practice recommendations on the imaging use of ultrasound from the European Society of Radiology ultrasound subcommittee. *Insights into Imaging* **11,** 115. doi:`10.1186/s13244-020-00919-x` (Nov. 9, 2020).
29. Simon, N. G., Noto, Y.-i. & Zaidman, C. M. Skeletal muscle imaging in neuromuscular disease. *J. Clin. Neurosci.* **33,** 1–10. doi:`10.1016/j.jocn.2016.01.041` (Nov. 1, 2016).
30. Ponrartana, S. *et al.* Effectiveness of diffusion tensor imaging in assessing disease severity in Duchenne muscular dystrophy: preliminary study. *Pediatr. Radiol.* **45,** 582–589. doi:`10.1007/s00247-014-3187-6` (Apr. 1, 2015).
31. Prompers, J. J. *et al.* Dynamic MRS and MRI of skeletal muscle function and biomechanics. *NMR Biomed.* **19,** 927–953. doi:`10.1002/nbm.1095` (2006).
32. Bárány, M. *et al.* Quantitative and qualitative fat analysis in human leg muscle of neuromuscular diseases by 1H MR spectroscopy in vivo. *Magn. Reson. Med.* **10,** 210–226. doi:`10.1002/mrm.1910100206` (1989).
33. Meyerspeer, M. *et al.* 31P magnetic resonance spectroscopy in skeletal muscle: Experts' consensus recommendations. *NMR Biomed.* **34,** e4246. doi:`10.1002/nbm.4246` (2021).
34. Lieber, R. L. *Skeletal muscle structure, function, and plasticity* (Lippincott Williams & Wilkins, 2002).
35. Scott, W., Stevens, J. & Binder–Macleod, S. A. Human Skeletal Muscle Fiber Type Classifications. *Phys. Ther.* **81,** 1810–1816. doi:`10.1093/ptj/81.11.1810` (Nov. 1, 2001).
36. Zierath, J. R. & Hawley, J. A. Skeletal Muscle Fiber Type: Influence on Contractile and Metabolic Properties. *PLOS Biol.* **2,** e348. doi:`10.1371/journal.pbio.0020348` (Oct. 12, 2004).

Background

2.1 Skeletal muscle

2.1.1 Anatomy and physiology

The essential role of skeletal muscle is body movement, posture, joint stabilization, and heat generation. It accounts for at least 40% of total body mass and consumes around 30% of the total available energy in the human body. Skeletal muscle is mainly composed of water ($\sim$75%), protein ($\sim$20%) and in minor quantities minerals, fat, and carbohydrates [1–4]. Skeletal muscle structure is highly specialized to achieve its intended functions [5]. Briefly, skeletal muscle structural macro-organization in order of smallest to largest units (shown in Fig. 2.1) are as follows [4–7]:

- *Muscle fibers* - long, cylindrical shape cells. They are multinucleated cells surrounded by connective tissue called endomysium.
- *Fascicles* - bundles of muscle fibers wrapped by a fibrous membrane called perimysium.
- *Muscle groups* - collections of several fascicles wrapped by connective tissue called epimysium. The terminal parts of the epimysium blend to form tendons. Muscle groups are attached to bone by tendons.

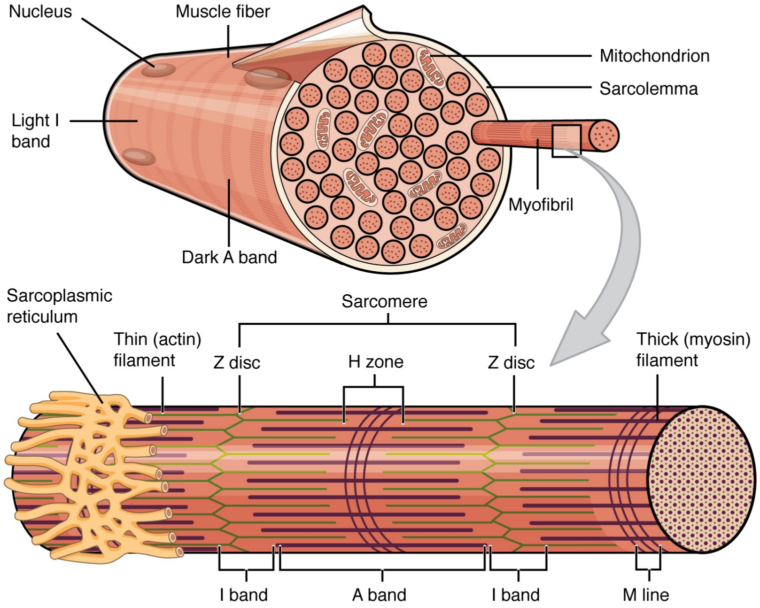

Figure 2.1: Sketch of skeletal muscle fiber, showing the highly organized structure of skeletal muscle. Image taken from [8], under a Creative Commons Attribution-ShareAlike 4.0 International License, allowing to copy and redistribute the material in any medium or format as long as appropriate credit is given.

Skeletal muscle fibers are formed by multinucleated cells in large cigar-shaped arrangements, usually extending for the length of the muscle. On a microscopic level, the muscle fibers are composed of the following [4–7]:

- *Sarcolemma* is the plasma membrane surrounding the periphery of muscle fibers.
- *Myofibrils* are contained inside muscle fibers, composed of a series of sarcomeres. They showed a striated pattern due to the presence of light (denoted with the letter I) and dark (denoted with the letter A) bands. I bands have a darker line called the Z disc. Meanwhile, A bands contain a lighter area called the H zone, with an M line in its center.
- *Sarcomeres* are the skeletal muscle structural and functional unit. They comprise two types of proteins myofilaments: the thin (actin) and the thick (myosin).
    - *Thick myofilaments* are made of the protein myosin. They extend along the A band, where the closest part to the H zone is smooth, but the outer part contains myosin heads.

  - *Thin myofilaments* are composed of actin protein. They are attached to the Z discs.

- *Sarcoplasmic reticulum* it is the muscle endoplasmic reticulum. Its composed of tubes surrounding the myofibrils and are in charge of storing and delivering calcium, which is required when the muscle is contracting.

The generation of contractions in skeletal muscle to produce force is complex as it involves the following steps [4–7]:

1. *Neural activation* generates a signal that travels to the peripheral nerves. These motor neurons are branched in a series of axon terminals that innervate different muscle fibers. A group of muscle fibers stimulated by the same motor neuron is called a motor unit.
   - *Motor neuron terminals* connect with muscle sarcolemma and are called Neuromuscular Junctions (NMJ), containing synaptic vesicles filled with Acetylcholine (ACh), a neurotransmitter.
2. *Calcium channels* are opened when an impulse reaches the axon terminal, releasing Ca^{2+}.
3. *Synaptic vesicles* release ACh, which diffuses and attaches to the ion channels in the sarcolemma. If enough ACh is attached, the channels become more permeable to sodium ions, while Na^+ is entering, potassium ions K^+ are exiting the muscle fiber.
4. *Depolarization* of the sarcolemma is caused due to the imbalance of Na^+ entering and K^+ exiting. This depolarization causes other ion channels to open and allow more Na^+ inside the cell.
5. *An action potential*, *i.e.* an electrical current, is generated due to the movement of the ions. The action potential travels along the sarcolemma through the entire muscle fiber.
6. *Acetylcholinesterase* enzyme breaks down ACh, generating only one contraction at a time. If more nerve impulses are sent, then more contractions will be produced.

Once the action potential is initiated and propagates through the muscle fibers, which causes the sarcoplasmic reticulum to release more Ca^{2+}. These ions trigger the binding between the myosin heads and the actin myofilaments, known as cross-bridge. Multiple cross-bridges are generated at a time, which generates the muscle fibers shortening, by sliding the thick and thin myofilaments together. Simultaneously, ATP is used to detach the myosin head to keep pulling toward the M line. Thus, the contraction process requires Ca^{2+} ions and ATP [5, 6]. The type of force produced depends on two factors: the frequency of muscle stimulation, *i.e.* the number of stimuli coming from the nerve, and the number of muscle fibers being recruited [6].

Skeletal muscle comprises heterogeneous fiber groups that shape its structure, composition and function, covering the wide range of tasks that skeletal muscle needs to do (from maintaining posture to performing high-intensity exercise). They are capable of adapting to external demands by changing their size, or composition [9, 10], which makes them of high interest in clinical interventions, rehabilitation, and sports training [11]. There are multiple classifications of skeletal muscle fibers based on their contractile speed, ability to maintain force, or appearance based on histochemical staining procedures. Table 2.1 shows a compilation of these classifications.

The energy required to sustain the process of muscle contractions, for instance, during exercise, is an essential need. However, because skeletal muscle does not have significant storage of ATP (about $\sim$5mM/kg WM), alternative metabolic pathways are activated to sustain ATP resynthesis. The contribution of each pathway to the overall muscle metabolism depends on the type and duration of the exercise, the training status, diet, sex, and oxygen availability, among other factors [12, 13]. Aerobic metabolism is highly dependent on oxygen availability, and it is commonly used during light-to-moderate resistance exercise, typically contributing around 95% of the total ATP resynthesis [6]. Meanwhile, anaerobic metabolism provides around 5% of the ATP produced by aerobic metabolism, but it is synthesized $\sim$3 times faster, providing enough ATP supply for a short-duration, high-intensity exercise.

Table 2.1: Skeletal muscle fiber type classification using different schemes [5, 11, 14]. First, by its metabolic preference, either oxidative phosphorylation or glycolysis. Next, from a histochemical staining perspective, from a contraction speed standpoint. Then, based on their ability to sustain exercise for long periods. Finally, by the recruitment of each fiber type accordingly to the % Maximum Voluntary Contraction (MVC). The preferred metabolism for type IIA/X fibers is a combination between oxidative phosphorylation and glycolysis. Of note, type IIB fibers (identified from the expression of myosin heavy chain) are not expressed in human skeletal muscle [15].

Classification	**Fiber type**		
Metabolism	Oxidative phosphorylation	Combined	Glycolytic
Histochemistry	Type I	Type IIA/X	Type IIB
Contraction speed	Slow	Medium/Fast	Fast
Resistance	High	Moderate	Low
Preferred MVC	Low ($\sim$ 15%)	Moderate ($\sim$ 55%)	High ($\sim$ 80%)

Anaerobic exercise can cause lactate accumulation, changing the pH of the environment, which alters muscle fibers contraction. Furthermore, the clearance of lactate from the environment requires energy, increasing the total ATP required for this type of metabolism [5]. Nevertheless, if oxygen supply is maintained during the contraction period, the preferred metabolic pathway is oxidative phosphorylation [5]. Suppose there is an oxygen deficit due to the intensity of the exercise. In that case, lactic acid accumulates in skeletal muscle due to anaerobic metabolism, which can cause muscle soreness or fatigue. Muscle fatigue is defined as the progressive decline in contraction performance during an intensive exercise [15].

The main chemical reactions involved in muscle metabolism are shown in Table 2.2, and the characteristics of both metabolic pathways are shown in Table 2.3.

Table 2.2: Metabolic pathways of ATP utilization and resynthesis in both glycolysis (anaerobic) and oxidative phosphorylation (aerobic) [13, 16, 17] pathways. ATP is the main source of energy, along with water, yielding ADP, inorganic phosphate, and hydrogen ions as products plus energy [17]. Aerobic metabolism's main reactants are carbohydrates and lipids, *i.e.* muscle glycogen, blood glucose and free fatty acids [13]. This pathway is highly dependent on oxygen availability, and its total ATP output is higher than anaerobic pathways. The main source for anaerobic metabolism is Phosphocreatine (PCr) and glycogen (the subscript *n* denotes a glycogen polymer of n glucose residues [13]). Lactate and Creatine (Cr) are among the products of this ATP resynthesis pathway.

ATP use	$\mathrm{ATP + H_2O \rightarrow ADP + P_i + H^+ + Energy}$
ATP resynthesis	
Anaerobic	$\mathrm{PCr + ADP + H^+ \rightarrow ATP + Cr}$
	$\mathrm{2\ ADP \rightarrow ATP + AMP}$
	$\mathrm{Glycogen_n + 3\ ADP + 3\ P_i \rightarrow Glycogen_{n-1} + 2\ Lactate + 3\ ATP}$
Aerobic	$\mathrm{Glucose + 6\ O_2 + 36\ ADP \rightarrow 6\ CO_2 + 6\ H_2O + 36\ ATP}$
	$\mathrm{Palmitate + 23\ O_2 + 130\ ADP \rightarrow 16\ CO_2 + 16\ H_2O + 130\ ATP}$

Table 2.3: Characteristics of anaerobic and aerobic metabolic pathways in skeletal muscle metabolism [13], including its ATP production rate, total ATP production capacities, preferred type of exercise of each, metabolic pathways (as seen in Table 2.2) and its net effects, along with the preferred type of fiber recruited and limitations. Anaerobic pathways can produce high rates of ATP but for a short period, favouring short-duration, high-intensity exercise, and the usual muscle fibers recruited are type II. On the contrary, aerobic pathways have a low ATP production rate, but the production can be sustained longer, favouring long-duration, low/moderate-intensity exercise. Hence, fiber type I is commonly recruited during aerobic pathways.

	Anaerobic (glycolysis)	**Aerobic (oxidative phosphorylation)**
ATP production rate	High	Low
Total ATP produced	Low	High
Exercise type	Short-term, high-intensity	Long-term, low/moderate-intensity
Metabolic pathways	• Degradation of PCr • Glycogen breakdown	• Lipids (free fatty acids) • Carbohydrates (glycogen, glucose) • Amino acids (proteins)
Fiber type preference	Type II – large sized, high energy consumption, glycolytic. Less fatigue resistant	Type I – short sized, low energy consumption, oxidative. More fatigue resistant
Limited by	Muscle acidification	Oxygen delivery

2.1.2 Electrical muscle stimulation

Electrical Muscle Stimulation (EMS) consists of applying electrical currents to skeletal muscle to induce muscular contractions. EMS can be delivered in two principal modes: Peripheral Nerve Stimulation (PNS) and Motor Point Stimulation (MPS) [18, 19]. PNS is delivered at a superficial site of the nerve (not necessarily close to the muscle) that innervates the target muscle. On the other hand, MPS is delivered at the motor point of the muscle, which is defined as the site of the muscle with the highest electrical excitability with the lowest amount of electrical stimulation [20], *i.e.* the location on the muscle belly where muscle contractions can be observed with the minimum EMS intensity, and duration [18]. EMS is used in clinical rehabilitation, known as functional electrical stimulation, with the aim of minimizing the effects of atrophy or loss of muscle mass following muscle immobilization in patients with injury [19, 21]. On the other hand, the application of EMS in healthy muscle, named therapeutic electrical stimulation, has been used mainly to improve muscle strength and performance [22].

EMS is a technique used as a research tool to assess the state and function of skeletal muscle in healthy and impaired patients. The effects of EMS depend on the electrical stimulation parameters, such as waveform, frequency, pulse width and amplitude, and the physical characteristics of the electrodes, their size and the distance between them. A field of interest regarding muscle function focuses on the effects and differences between voluntary and electrically induced contraction. Some of these parameters are described below [22–27].

- *Frequency* is the number of electrical pulses produced per second. The frequency value is selected according to the application, but the typical frequency ranges in clinical settings are within 20-50Hz. Higher frequency values will increase muscle force at the expense of causing fatigue or patient discomfort.

- *Pulse duration* is the amount of time that each electrical pulse is applied. Studies have shown that longer pulse duration can potentially increase the number and the depth of muscle fiber recruitment.

- *Amplitude* of the electrical pulses. As the current amplitude increases, there is an increase in generated force due to higher muscle fiber recruitment. The effects of EMS amplitude on fatigue are unclear [22, 27]

- *Electrode placement* is an essential factor that will affect the performance of muscle contractions. For instance, a gel is required to decrease the impedance between the electrodes and the skin. The spacing between the electrodes can also affect muscle contraction, as a greater distance between the electrodes will recruit muscle fibers located deeper in the muscle. Nevertheless, similar to EMS amplitude, there is some debate regarding the placement of electrodes between muscle belly, motor point, or peripheral nerve [22].

The main advantage of involuntary contractions through EMS over voluntary contractions is that EMS-induced stimulation selectively trains muscles and can change the relative magnitude of muscle group recruitment. Contrarily, involuntary contractions have the disadvantage of causing possible levels of discomfort and the limitation of spatial recruitment of muscle fibers, mainly on the surface of the muscle. A comparison between the two types of contractions is shown in Table 2.4. It is believed that the characteristics of both contractions can help improve the treatment and follow-up of athletes and patients with muscle diseases [23].

Table 2.4: Comparison between voluntary vs electrically evoked contractions. *A point to note is the controversy around the recruitment pattern in EMS contractions, where some authors suggest that it is inverse recruitment (compared to voluntary contractions) [23, 24]. In contrast, other authors suggest non-selective random recruitment [25]. The temporal activation for EMS contractions is naturally synchronous, as they followed the stimulation protocol. The spatial activation between voluntary vs EMS contractions also differs, as EMS only excites a particular group of muscle fibers associated with the motor points or the peripheral nerves closer to the electrodes. In addition, as the electrodes are not moving, there is no rotation of muscle fibers, *i.e.* they are spatially fixed. A study made in 1993 showed that EMS muscle activation measure by changes in T_2 cross-sectional area images is at most ~60% for 100% MVC, suggesting that EMS contractions are incomplete [28]. Finally, due to the altered recruitment pattern and the inability to rotate muscle fibers, EMS contractions tend to be more energetically demanding than voluntary contractions.

	Voluntary contractions	**EMS contractions**
Recruitment pattern	Selective and ordered motor unit recruitment: type I ⟶ type II	Selective and inverse motor unit recruitment*: type II ⟶ type I
Temporal Activations	Asynchronous	Synchronous
Spatial Activations	• Profound (far from electrodes) • Rotation is possible • Nearly complete	• Superficial (close to electrodes) • Spatially fixed • Incomplete
Fatigue	Causes some fatiguing	High metabolic demand, causing fatigue faster

2.1.3 Surface electromyography

Surface Electromyography (EMG) is a non-invasive technique that measures the electrical activity of skeletal muscle. As described in Chapter 2.1, the ability of a muscle to contract and generate force is possible due to the propagation of Muscle Action Potentials (MAP) along a muscle fiber [29, 30]. A motor unit innervates several muscle fibers. Multiple muscle fibres are recruited simultaneously when an action potential is sent to the motor unit. The superposition of many MAP arising from muscle fibers in a motor unit causes changes in the electromagnetic field that extends to the skin, which is detected by EMG [29]. Although EMG has clinical value, its immediate limitations are that the signal is a superposition of multiple MAP, increasing the chances of cross-talking (*i.e.* detect electrical signals from other muscles) and that only muscles below the skin can be studied.

Thus, EMG is a measure of the overall neuromuscular activity due to contractions, tension generation and movement of skeletal muscle [31]. EMG is used extensively in clinical applications to diagnose and follow-up muscle diseases, monitor the effects of rehabilitation programs, assess muscle function, and study the correlation between muscle metabolic and electrical changes [32].

Relevant EMG signals are in the range of 1-500Hz and have a typical amplitude of 0-10mV. EMG requires thorough planning, hardware design, and pre-processing because the signal contains electrophysiological information and artifacts such as motion and ambient and electronic equipment noise. Some of the significant factors that influence EMG signal are [33]:

- Technical: environmental conditions (ambient noise), and hardware design (electrode characteristics, electrodes-skin interface, amplifiers, filters).
- Experimental: skin preparation, electrode configuration, and contraction conditions (type and duration of contraction).
- Descriptive: signal acquisition, signal processing, and data analysis.
- Physiological: training status and muscle characteristics (structural and functional).

Standard methods to analyze EMG signals include time domain (mean root square, averaged rectified value), frequency domain (median frequency, mean frequency) techniques, wavelet analysis, and specialized statistics, which are mainly used to analyze and interpret the characteristics of an EMG signal modelled as a random process [34].

2.2 Magnetic resonance imaging

2.2.1 Magnetic resonance spectroscopy

Magnetic Resonance Spectroscopy (MRS) is a technique that provides information on the biochemical environment within the body, thereby allowing the identification and quantification of relevant metabolites [35]. MRS relies on the presence of an ensemble of nuclei with a non-zero spin that will precess at a particular rate (called the Larmor frequency) around a static magnetic field B_0. Each nuclei species will have a slightly shifted frequency compared to the Larmor frequency due to modulation of the local magnetic field (B_0+B_{loc}) caused by the interactions of the nucleus with its surrounding electronic environment [36–38]. Thus, each molecule within a voxel of interest (VOI) will show a distinct resonant frequency (or chemical shift) as in the ^{1}H-MRS muscle spectra shown in Figure 2.2.

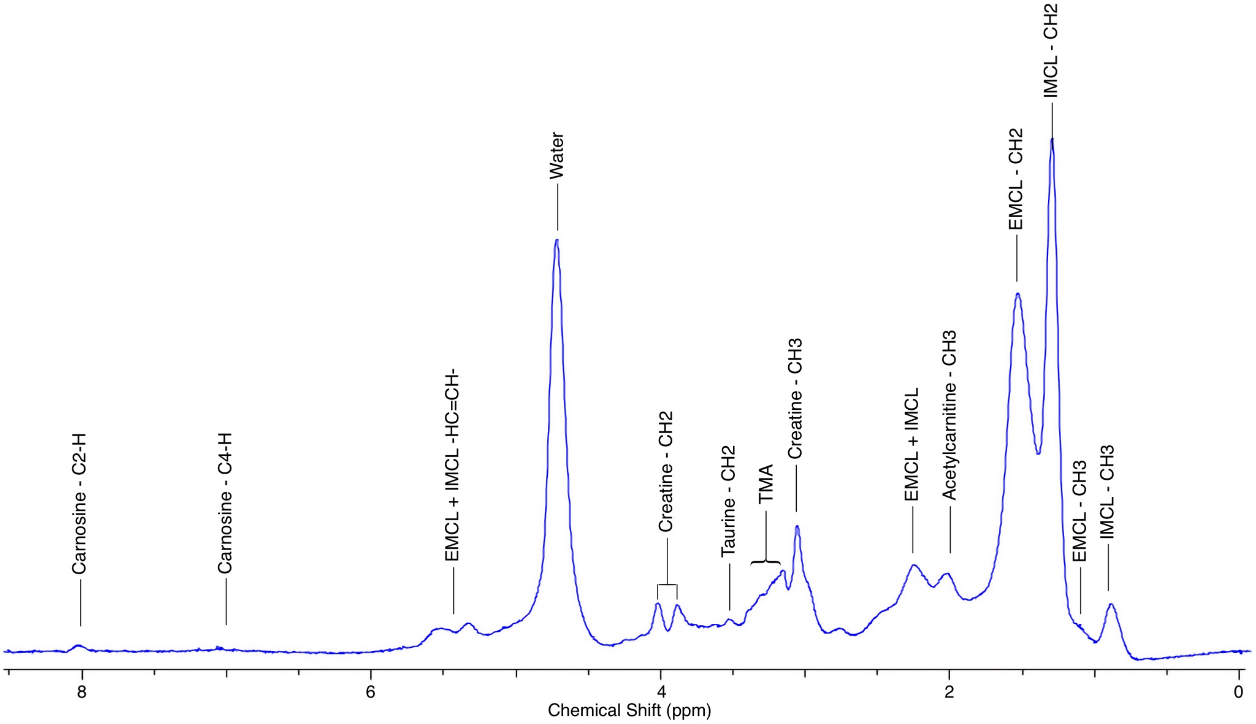

Figure 2.2: ^{1}H-MRS muscle spectra of tibialis anterior (TA) using a Point-Resolved Spectroscopy sequence (Sequence B.). Metabolites present in spectra were identified and labelled. The chemical shift (δ) is expressed in ppm to allow comparison between MRS experiments performed at different magnetic field strengths (B_0). Trimethylamine complex (TMA): includes Choline + Carnitine + Acetylcarnitine.

The main advantage of MRS compared to other biochemical quantification methods, such as blood samples or biopsies, is its non-invasive nature which allows a fast and painless way of studying the biochemical properties of tissue. The most common nucleus used in MRS is ^{1}H, ^{31}P and ^{13}C with relative sensitivities (with respect to ^{1}H) of 1, 0.066 and 0.016. In general, ^{1}H-MRS is the main clinical MRS tool in the human brain, and ^{31}P-MRS in muscle [39].

After data collection of the time domain Nuclear Magnetic Resonance (NMR) signal, and the transformation to the frequency domain, the following information can be extracted from a typical MRS spectrum [38]:

- Metabolite identification: due to the chemical shift (δ) of each molecule with respect to B_0, a unique frequency shift (in ppm) can be assigned to each type of nuclear spin that is part of a molecule. Peaks can sometimes also be associated with a particular metabolite as long as there is no co-resonant between metabolites, *i.e.* two metabolites present a similar chemical shift, thus, causing overlapping or 'hiding' of one of the co-resonant metabolites.

- Metabolite concentration: each peak area is associated with the metabolite concentration within the VOI. Internal or external reference standards are needed to measure the relative or absolute metabolite concentration. MRS can detect metabolite concentrations higher than $\sim 5\mu$M.

- Metabolite T_2 relaxation times: the Full Width at Half Maximum (FWHM) of each peak provides information about the T_2 relaxation time of the given spins within a metabolite. The narrower the peak, the longer the T_2 time of that molecule (assuming a Lorentzian line shape).

- Peak Splitting: this occurs when there are interactions between different spin types within the same molecule. The splitting patterns help understand molecular structure.

Special attention is needed regarding metabolite relaxation times, B_0 field inhomogeneities, pulse sequence parameters, motion artifacts, water suppression efficiency, VOI localization methods and data pre-processing since they will all influence the signal intensity, chemical shift, line width and fit of the MRS spectra, which then add complexity to data analysis and absolute quantification of the metabolites [40]. Moreover, *in vivo* MRS experiments add an extra layer of variability because the metabolic window is influenced by diet, medications, training status, and fasting, among others, [37, 41].

Magnetic susceptibility

Magnetic susceptibility is the degree to which a material can be magnetized in response to an externally applied magnetic field. This effect will cause interactions and distortions in the local magnetic field of the material. The magnetic susceptibility is defined as:

$$\chi = \mu_0 \frac{M}{B_0}$$

Where:

M = magnetization induced inside the material

χ = magnetic susceptibility of the material

μ_0 = vacuum permeability

B_0 = external magnetic field (in vacuum)

The value of χ is dimensionless. It exhibits the magnetic properties of the material when interacting with an external magnetic field: diamagnetism ($\chi < 0$) with M aligned opposite to B_0. In contrast, paramagnetism ($\chi \sim 0$), superparamagnetism ($\chi > 0$) and ferromagnetism ($\chi >> 0$) have M aligned in the same direction as B_0 [42].

Bulk Magnetic Susceptibility (BMS) shift arises due to the partial alignment of the magnetic moments (induced by B_0) that generates a magnetic field in the opposite direction of B_0, called the demagnetizing field. When a continuous and homogeneous material is placed in a uniform magnetic field, the effective magnetic field (B_{effec}) surrounding the material is [43]:

$$B_{effec} = (1 + D)B_0 + I \tag{2.1}$$

Where the homogeneous (D) and inhomogeneous (I) BMS components depend on the magnetic susceptibility of the material (χ), its geometry and orientation relative to the uniform magnetic field B_0. Thus, BMS will modify the local magnetic field of a group of molecules depending on its spatial distribution, which ultimately alters the chemical shift in an MRS experiment. This means that the overall frequency shift of a given group of molecules experiencing BMS shifts will have two components:

$$\delta = \delta_\sigma + \delta_\chi$$

Where:

δ_σ = interactions of the nucleus with its surrounding electronic environment
δ_χ = Bulk Magnetic Susceptibility

Geometry examples Two geometries of interest while studying BMS shifts in MRS are the spherical and cylindrical shapes where the homogeneous and inhomogeneous components of Equation 2.1 are [44, 45]:

Spherical geometry

$$D = \frac{\chi_w}{3}$$

$$I = 0$$

Then, B_{effec} of a spherical geometry is:

$$B_{effec} = \left(1 + \frac{\chi_w}{3}\right) B_0 \tag{2.2}$$

Cylindrical geometry

$$D = \frac{\chi_w}{2} - \frac{\chi_m}{6}$$

$$I \propto \frac{\cos 2\theta}{r^2}$$

Then, B_{effec} of a cylindrical geometry is:

$$B_{effec} \propto \left(\frac{\chi_w}{2} - \frac{\chi_m}{6}\right) B_0 + \frac{\cos 2\theta}{r^2} \tag{2.3}$$

Where the magnetic susceptibility of the medium surrounding the molecule is denoted by χ_w while χ_m is the magnetic susceptibility of the molecule itself. The B_{loc} for both geometries are altered due to magnetic susceptibilities. However, in the cylindrical geometry, B_{loc} also depends on the angle between the z-axis of the cylinder and the direction of B_0 as seen in Equation 2.3.

Dipolar coupling

The precession of spins forms current loops (i) of cross-sectional area (A) where the associated magnetic dipole moment (μ) of the spin precession is defined as:

$$\mu = iA$$

In MRI, the magnetic dipoles that experience the static magnetic field B_0 will align parallel (lowest energy state) or antiparallel (highest energy state) to B_0. The overall interaction between these magnetic dipole moments through space is known as dipolar coupling or dipole-dipole interaction, and it is responsible for the main relaxation mechanisms (T_1 and T_2) in MRI and MRS [38]. The magnitude of these interactions relies on spin characteristics such as [45]:

- Interaction type: between proton-proton or electron-proton spins. Because electrons have a higher gyromagnetic ratio (γ), electron-proton is stronger than proton-proton dipolar coupling.
- Relative motion: the spatial freedom of the involved spins will affect the strength of the interaction as well as the relaxation mechanisms (T_1 or T_2).
- Distance: the strength of the dipolar coupling is proportional to r^{-6} where r is the distance between the magnetic dipole moments.
- Angle: the magnitude of dipolar coupling is modulated by the angle between the dipoles (θ) in the form of:

$$3\cos^2\theta - 1 \tag{2.4}$$

In a typical MRI study, the random and fast tumbling of the spins causes annihilation of the dipolar interactions (*i.e.* they average to zero) so that no direct effects are seen. Nevertheless, in highly structured tissues such as skeletal muscle, the tumbling of the spins is restricted, causing a net residual dipolar coupling effect that will alter the local magnetic field.

J-coupling

J-coupling, or scalar coupling, results from the interaction between two spins A and X (denoted as $J_{A,X}$) mediated by chemical bonds, as opposed to dipolar coupling, where the interaction is through space. Among its properties, j-coupling is field-independent (does not depend on the strength of B_0), its magnitude depends on the gyromagnetic ratio of the involved spins, is mutual (*i.e.* $J_{A,X} = J_{X,A}$) and can be classified either as homonuclear (between protons with different chemical shifts) or heteronuclear (between proton and other nuclei such as ^{13}C). Since j-coupling is mediated through chemical bonds, its magnitude decreases as the number of bonds between spins increases. Overall, j-coupling helps identify the proximity among different nuclei on the bonding framework, thus allowing to study of the through-bond connectivity and stereochemistry in molecules.

J-coupling is of interest in NMR experiments because it plays a role in the magnetization transfer between nuclear spins in specific pulse sequences [38, 46]. The main effect of such coupling in NMR is the splitting of spectral lines of coupled spins into multiplets. The distance (measured in Hz) between the split peaks is known as the coupling constant J, and typically in the homonuclear interaction, the coupling constant is within the range of 0-20Hz. The most common type of j-coupling in NMR is the weak one, which is present when the coupling constant is smaller than the difference between the chemical shifts of the molecules interacting, *i.e.* when $J_{A,X} << \Delta\nu = | \nu_A - \nu_X |$. Examples of weak coupling are heteronuclear j-couplings, such as lactate and GABA metabolites.

MRS of skeletal muscle

The use of MRS in clinical applications of skeletal muscle has increased in the diagnosis and follow-up of patients with muscle myopathies [47]. An anatomical image is used to correctly select the VOI in an MRS study by taking advantage of the high contrast within tissues in MRI images. An example of the exceptional contrast is shown in Figure 2.3, which shows an axial proton-density weighted fat-saturated scan of the lower leg, where it is easy to distinguish muscle groups.

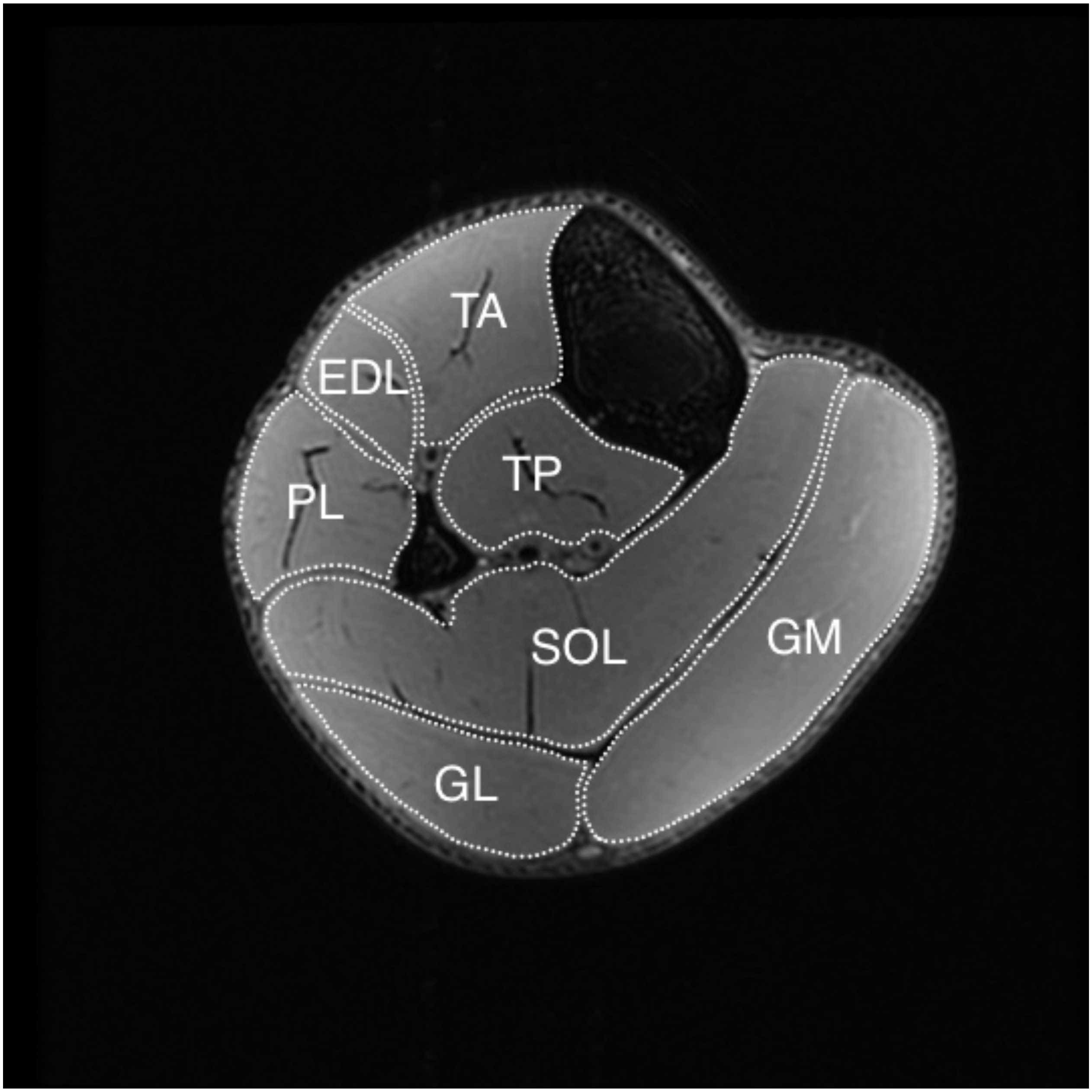

Figure 2.3: Ax proton-density weighted fat saturated showing the lower leg muscle groups. tibialis anterior (TA), tibialis posterior (TP), extensor digitorum longus (EDL), peroneus longus (PL), soleus (SOL), gastrocnemius lateralis (GL), and gastrocnemius medialis (GM). The image shows the ability of MRI to provide good tissue contrast to differentiate muscle tissue groups.

Proton Compared to the brain, proton spectroscopy of skeletal muscle presents a series of challenges due to the highly structured arrangement of muscle fibers, such as degraded spectral line widths (around 15Hz), BMS shifts, and residual dipolar coupling effects. Thus, the characteristics of the ^{1}H-MRS spectra of skeletal muscle will change depending on the overall direction of the muscle, and its fiber arrangement with respect to B_0 [41, 45, 48]. The metabolites most often seen in skeletal ^{1}H-MRS are listed in Table 2.6.

The extramyocellular lipids (EMCL) and intramyocellular lipids (IMCL) are visible in ^{1}H-MRS of skeletal muscle as shown in Figure 2.2 with their dominant peaks around 1.3ppm. EMCL has been found as macroscopically visible septa surrounding the fascicles [44, 48, 49] of ∼0.5-2mm thickness, stored as bulk fat layers that reflect the particular arrangement of EMCL in the form of tubes of lipids within the muscle. These fat deposits are thought to be metabolically inactive, and their peak amplitude does not scale with the size of the voxel, suggesting a non-uniform distribution of this class of lipids in skeletal muscle [50]. On the other hand, IMCL is stored inside myocytes in the cytoplasm as spherical droplets. The closeness to mitochondria inside the cell shows a primary role as a metabolically active molecule for energy supply during long-lasting exercises [50]. As opposed to EMCL, IMCL does scale with the size of the voxel, suggesting a uniform distribution across the skeletal muscle. IMCL depends on sex, diet, physical condition, fasting and training level. Furthermore, it has been studied more than EMCL due to its relationship between insulin resistance, and exercise [51].

The difference in storage geometry between EMCL (as cylinders) and IMCL (as spheres) induces changes in the local magnetic field and produces BMS shifts (as described in section 2.2.1). The final result is a change in the frequency shift of EMCL (of up to 0.2ppm relative to IMCL) as a function of the angle between the muscle fibers direction and B_0 [48], even though the chemical structure of both lipids are identical. Furthermore, metabolites such as taurine at 3.02ppm or creatine at 4ppm showed a peak splitting pattern while changing the direction of the muscle relative to B_0. This behaviour has been attributed to residual dipolar coupling effects due to the restricted motion (section 2.2.1) of these metabolites in skeletal muscle [52, 53].

Table 2.5: Muscle orientation and fiber type content in human calf muscle on the lower leg. Muscle fibers extend parallel (fusiform) or with a certain angle (pennate) to the tendon [5, 54]. More information regarding the pennation angle of several muscles can be found in [5].

	Orientation	**Characteristics**
tibialis anterior (TA)	Parallel to the axis of leg (fusiform)	Predominantly fast twitching glycolytic type II muscle fibers
soleus (SOL)	Crossing fibers to the axis of leg (pennate)	Predominantly slow twitching oxidative type I muscle fibers
gastrocnemius medialis (GM)	Crossing fibers to the axis of leg (pennate)	Mixed muscle fibers I and II (∼50%)
gastrocnemius lateralis (GL)	Crossing fibers to the axis of leg (pennate)	Slightly higher proportion of muscle fibers I than II

Thus, skeletal muscle proton spectra are expected to change as a function of orientation relative to B_0. Even more, muscle groups within skeletal muscle have different fiber orientations than the overall extremity. One example is the calf muscle in the lower leg, where SOL and GM have a pennation relative to the tendon, but tibialis anterior runs parallel to the lower leg (Tbl. 2.5), meaning that, even for the same position of the lower leg in the MRI, ^{1}H-MRS will change depending on the muscle group being studied. The concentration of metabolites in proton spectroscopy will also depend on the studied muscle. For the case of the calf muscle in the lower leg, an average concentration of each metabolite is given in Table 2.6.

Phosphorous ^{31}P-MRS has been the most used nucleus to study skeletal muscle since the early 1980s. Its use has focused primarily on the dynamics of high-energy phosphates and intracellular pH, which provides useful *in vivo* muscle metabolism information at rest, during exercise and the application of electrical stimulation within a time scale of seconds to minutes [47, 72–74]. ^{31}P-MRS has also been used to investigate metabolic myopathies [32] such as McArdle's syndrome [75, 76], Huntington's disease [77], glycogen storage diseases, mitochondrial diseases, among others [41]. The common metabolites found in skeletal muscle employing phosphorous spectroscopy include ATP, PCr, and P_i with average concentrations in the calf muscle of 8.2mM, 33mM and 4.5mM, respectively [78]. Altogether, the main interest of ^{31}P-MRS relies on the role that these metabolites play in muscle metabolism.

Table 2.6: ^{1}H-MRS metabolites typically found in skeletal muscle. The concentration of each metabolite depends on the studied muscle group (TA, GM, SOL, among others) and conditions (rest, exercise). An average value across studies is given for each metabolite at rest. Lactate has been reported to be detectable in ischemic exercise protocols, but at rest, its peak amplitude is considered to be at background levels (*i.e.* not detectable). EMCL is considered to be inconsistent (depending on the VOI position and size) to be measured.

Metabolite	**Concentration (mM)**	**Reference**
Acetylcarnitine (AcCtn)	2.5	[55, 56]
Carnitine (Ctn)	7	[55, 57, 58]
Carnosine (Car)	6	[59–62]
Choline (Cho)	12	[63]
Creatine (Cr)	40	[64, 65]
EMCL	-	[53, 66]
IMCL	10	[67, 68]
Lactate (Lac)	-	[69, 70]
Taurine (Tau)	12	[65, 71]

$$\mathrm{PCr} + \mathrm{ADP} + \mathrm{H}^+ \rightarrow \mathrm{ATP} + \mathrm{Cr} \tag{2.5}$$

The creatine kinase reaction (Equation 2.5) describes the production of ATP utilizing PCr and ADP. The reaction is at equilibrium when the muscle is at rest, but during exercise, ATP is used and degraded (as described in Table 2.2) to ADP and $\mathrm{P_i}$. Nevertheless, while ADP is reused for ATP resynthesis, $\mathrm{P_i}$ increases, and PCr decreases. Thus, the net reaction is:

$$\mathrm{PCr} + \mathrm{H}^+ \leftrightarrow \mathrm{Cr} + \mathrm{P_i} \tag{2.6}$$

Similarly, the intracellular pH can be quantified non-invasively by looking at the relative chemical shift of $\mathrm{P_i}$, which allows studying the effects of H^+ in muscle fatigue, performance and glycolysis [41].

2.2.2 Functional Magnetic Resonance Imaging

Since the earliest 1900s, it was suggested that cerebral blood flow (CBF) could be related to neuronal activity because glucose metabolism and CBF are related [79]. Functional Magnetic Resonance Imaging (fMRI) techniques were initially developed to study brain function. One

MRI contrast method that took advantage of this concept was Blood Oxygen Level Dependent (BOLD) imaging, which is a non-invasive fMRI contrast technique used to measure the changes in blood flow and oxygenation in tissues, first described in animal models in 1990 by Seji Ogawa [80]. This technique is based on a complex interaction between the changes and magnetic properties of oxyhemoglobin (oxy-Hb) and deoxyhemoglobin (deoxy-Hb) within the microvasculature [81], and tissue blood flow and volume [82].

The first BOLD signals from the brain were obtained with a gradient-echo (GE) MRI pulse sequence, which in contrast to a spin-echo (SE), GE sequences are sensitive to local magnetic field inhomogeneities, a property that BOLD studies take advantage of. The mechanism to generate contrast with BOLD-fMRI is shown in Fig. 2.4 and consists of the following steps:

1. A task or stimuli is applied to the tissue of interest, for example, a visual stimulus for the brain or a motor task for skeletal muscle
2. The brain will move from a baseline to an active state, increasing its metabolism
3. To adjust for the current metabolic demands, the CBF, the cerebral metabolic rate of oxygen (CMRO2), and cerebral blood volume (CBV) will increase. In particular, the increase of CBF will surpass the CMRO2 increase [83] (by x2-3), which will cause an increase of oxygen in capillaries and veins. The two-fold increase in CBF secures oxygen delivery from the bloodstream to the active tissue by increasing the pressure gradient.
4. While CBF and CMRO2 increase, the oxygen extraction fraction (OEF), *i.e.* the ratio of O_2 molecules that tissue extract and metabolize from the blood flow (to maintain function and morphological integrity) decreases, which causes an imbalance in the (deoxy/oxy)-Hb ratio.
5. Hemoglobin shows different magnetic properties accordingly to its state. For instance, oxy-Hb is diamagnetic, while deoxy-Hb is paramagnetic. Paramagnetic or diamagnetic substances will show magnetic susceptibility when exposed to a magnetic field, either aligning in/against the direction of the main magnetic field B_0, and thus changing the local magnetic field [42] (Section 2.2.1). These minor differences will affect the T_2^* of

the local environment, causing a change in the signal intensity, thus generating the contrast in BOLD-fMRI.

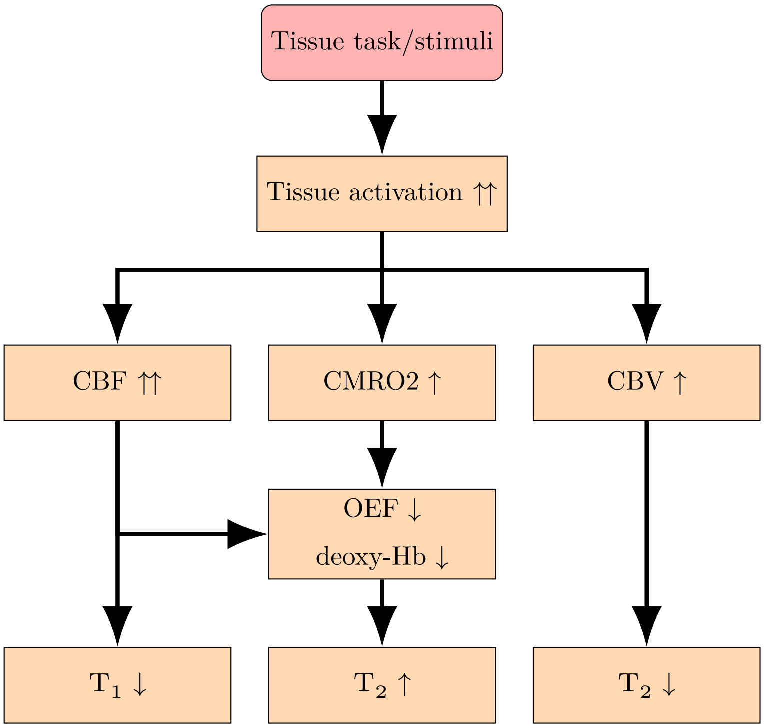

Figure 2.4: Flowchart of the fundamental process for BOLD-fMRI signal generation. When tissue is stimulated or performs a task, it will go from a rest state to an active state, changing its metabolism to adjust to the current demands. These changes will influence the magnetic properties of the surroundings, altering the MRI signal. cerebral blood flow (CBF), cerebral metabolic rate of oxygen (CMRO2), cerebral blood volume (CBV), and oxygen extraction fraction (OEF). T_1 and T_2: MRI longitudinal and transversal relaxation constants.

Thus, during brain activation, there is a relative increase of oxy-Hb, and a decrease of deoxy-Hb, generating an increase in the signal intensity. Although the first BOLD-fMRI studies were performed on the brain, BOLD-fMRI can be used to study the activation of other tissues, such as skeletal muscle [84, 85]. The physical mechanism that gives rise to the BOLD signal in skeletal muscle is similar to the brain. However, the physiological basis for muscle BOLD includes muscle blood volume, perfusion, metabolic characteristics, and vasculature architecture [84].

Similarly to the brain, muscle BOLD will show a change in the signal over time when the (oxy/deoxy)-Hb ratio changes. For example, at rest state, there is a transient equilibrium between deoxy-Hb and oxy-Hb, which is the baseline of the signal over time. An increase in deoxy-Hb will augment the spin dephasing due to small field inhomogeneities (*i.e.* $T_2^* \uparrow$), thus reflecting as a drop in the signal intensity. On the contrary, an increase in oxy-Hb will show as an increase in signal intensity [84]. The first BOLD studies on skeletal muscle started in the early 90s, where a change in the signal intensity of T_2-weighted Echo Planar Imaging (EPI) was observed during rest, ischemia, and reactive hyperemia [86]. Generally speaking, muscle BOLD is assumed to reflect mainly the changes in blood oxygenation [87], which physiologically is related to an increase in muscle metabolic activity. Skeletal muscle BOLD has been used to study muscle microperfusion, and metabolic disturbances in diseases such as peripheral arterial occlusive disease and chronic compartment syndrome [81, 87–89].

2.2.3 Magnetization Transfer

Magnetization Transfer (MT) imaging is an MRI technique whose contrast is generated through the exchange of protons between 'free' or highly mobile and bound (to macromolecules) or highly restricted water molecules. MT was discovered by accident by Dr. Balaban in 1989 by studying the exchange rate between free vs bound water using NMR saturation transfer methods [90].

The mechanism behind MT is well-understood [91], in a typical MRI scan, most of the detected signal comes from the free pool, *i.e.* water molecules or transient protons binding with similar molecules. Their lack of structure and rapid rotation provides them with long relaxation times (T_1 and T_2) and a narrower range of frequencies ($\sim$100Hz) around the Larmor frequency. On the contrary, the bound pool, *i.e.* water molecules associated with the surface of macromolecules and macromolecules themselves. This pool is highly restricted in motion, resulting in shorter T_2 values (T_2 <5ms) and a wider frequency range ($\sim$40kHz) around the Larmor frequency. The T_2 values of the bound pool are too short that a routine MRI scan would not be able to record the signal arising from these molecules.

Nevertheless, the free and bound water pools are not isolated from each other. They can interact through dipole-dipole cross-relaxation mechanism or chemical exchange, contributing significantly to the relaxation phenomena [92], which MT takes advantage of to generate contrast [91, 93]. The mechanism of MT can be described as follows:

1. An off-resonance (with respect to the Larmor frequency) B_1 pulse is applied, which aims to saturate the bound pool. If the B_1 pulse is placed in the right off-resonance frequency, the bound pool spins have a broader absorption lineshape, thus, they are more sensitive to the off-resonance RF pulse.
2. Both the free (^1H_f) and bound pools (^1H_b) interact with each other through chemical exchange and/or dipolar cross-relaxation. This means that saturated protons move to the free pool (from the bound pool), and unsaturated protons (from the free pool) move to the bound pool, which eventually will be saturated and exchanged. These exchange cycles can be expressed as shown in Eqn. 2.7.

$$^1H_b \underset{\text{saturated}}{\overset{\text{unsaturated}}{\rightleftharpoons}} {}^1H_f \tag{2.7}$$

3. After enough exchanges, the free pool will show a decrease in signal (due to the receipt of the saturated protons coming from the bound pool). Thus, MT indirectly measures the interaction between the free and bound pools through the exchange rate of (un)saturated protons [92].

MT has been shown helpful in Magnetic Resonance Angiography to enhance blood vessel visibility by suppressing the signal from soft tissue such as the brain or muscle [94, 95], showing significant improvements in the contrast between soft tissue and blood vessels. Another application of MT is in Multiple Sclerosis (MS), where white matter tissue typically shows an MT ratio of ∼45% with a small variability (<2.5%) in healthy subjects, however, MT of patients with MS showed a decreased MT ratio of ∼20% [96, 97], which is attributed to the demyelinated lesions. Furthermore, MT has been used to indicate the severity of tissue damage in MS [98].

References

1. Yamada, Y. *et al.* Extracellular Water May Mask Actual Muscle Atrophy During Aging. *The Journals Gerontol. Ser. A* **65A,** 510–516. doi:`10.1093/gerona/glq001` (May 1, 2010).
2. Yamada, Y. *et al.* The Extracellular to Intracellular Water Ratio in Upper Legs is Negatively Associated With Skeletal Muscle Strength and Gait Speed in Older People. *The Journals Gerontol. Ser. A* **72,** 293–298. doi:`10.1093/gerona/glw125` (Mar. 1, 2017).
3. Lorenzo, I., Serra-Prat, M. & Yébenes, J. C. The Role of Water Homeostasis in Muscle Function and Frailty: A Review. *Nutrients* **11,** 1857. doi:`10.3390/nu11081857` (Aug. 2019).
4. Frontera, W. R. & Ochala, J. Skeletal Muscle: A Brief Review of Structure and Function. *Calcif. Tissue Int.* **96,** 183–195. doi:`10.1007/s00223-014-9915-y` (Mar. 1, 2015).
5. Lieber, R. L. *Skeletal muscle structure, function, and plasticity* (Lippincott Williams & Wilkins, 2002).
6. Marieb, E. N. & Hoehn, K. *Human anatomy & physiology* (Pearson education, 2007).
7. Schmalbruch, H. *Skeletal Muscle* doi:`10.1007/978-3-642-82551-4` (Springer Berlin Heidelberg, Berlin, Heidelberg, 1985).
8. Biga, L. M. *et al. Anatomy & Physiology* (OpenStax/Oregon State University, Sept. 26, 2019).
9. Pette, D. & Staron, R. S. in *International Review of Cytology* (ed Jeon, K. W.) 143–223 (Academic Press, Jan. 1, 1997). doi:`10.1016/S0074-7696(08)61622-8`.
10. Grossman, E. J. *et al.* Effects of inactivity on myosin heavy chain composition and size of rat soleus fibers. *Muscle & Nerve* **21,** 375–389. doi:`10.1002/(SICI)1097-4598(199803)21:3<375::AID-MUS12>3.0.CO;2-Z` (1998).
11. Scott, W., Stevens, J. & Binder–Macleod, S. A. Human Skeletal Muscle Fiber Type Classifications. *Phys. Ther.* **81,** 1810–1816. doi:`10.1093/ptj/81.11.1810` (Nov. 1, 2001).
12. Westerblad, H., Bruton, J. D. & Katz, A. Skeletal muscle: Energy metabolism, fiber types, fatigue and adaptability. *Exp. Cell Res. Special Issue: Myogenesis* **316,** 3093–3099. doi:`10.1016/j.yexcr.2010.05.019` (Nov. 1, 2010).
13. Hargreaves, M. & Spriet, L. L. Skeletal muscle energy metabolism during exercise. *Nat. Metab.* **2,** 817–828. doi:`10.1038/s42255-020-0251-4` (Sept. 2020).
14. Zierath, J. R. & Hawley, J. A. Skeletal Muscle Fiber Type: Influence on Contractile and Metabolic Properties. *PLOS Biol.* **2,** e348. doi:`10.1371/journal.pbio.0020348` (Oct. 12, 2004).
15. Allen, D. G., Lamb, G. D. & Westerblad, H. Skeletal Muscle Fatigue: Cellular Mechanisms. *Physiol. Rev.* **88,** 287–332. doi:`10.1152/physrev.00015.2007` (Jan. 2008).
16. Hargreaves, M. Skeletal Muscle Metabolism During Exercise In Humans. *Clin. Exp. Pharmacol. Physiol.* **27,** 225–228. doi:`10.1046/j.1440-1681.2000.03225.x` (2000).
17. Dunn, J. & Grider, M. H. in *StatPearls* (StatPearls Publishing, Treasure Island (FL), 2022).
18. Nakagawa, K. *et al.* Motor point stimulation primarily activates motor nerve. *Neurosci. Lett.* **736,** 135246. doi:`10.1016/j.neulet.2020.135246` (Sept. 25, 2020).
19. Bergquist, A. J. *et al.* Neuromuscular electrical stimulation: implications of the electrically evoked sensory volley. *Eur. J. Appl. Physiol.* **111,** 2409. doi:`10.1007/s00421-011-2087-9` (July 30, 2011).
20. Moon, J.-Y. *et al.* Surface Mapping of Motor Points in Biceps Brachii Muscle. *Ann. Rehabil. Med.* **36,** 187–196. doi:`10.5535/arm.2012.36.2.187` (Apr. 2012).
21. Vanderthommen, M. *et al.* Human Muscle Energetics During Voluntary and Electrically Induced Isometric Contractions as Measured by 31P NMR Spectroscopy. *Int. J. Sports Med.* **20,** 279–283. doi:`10.1055/s-2007-971131` (July 1999).
22. Doucet, B. M., Lam, A. & Griffin, L. Neuromuscular Electrical Stimulation for Skeletal Muscle Function. *The Yale J. Biol. Med.* **85,** 201–215 (2012).
23. Deligianni, X. *et al.* Synchronous MRI of muscle motion induced by electrical stimulation. *Magn. Reson. Med.* **77,** 664–672. doi:`10.1002/mrm.26154` (2017).
24. Maffiuletti, N. A. Physiological and methodological considerations for the use of neuromuscular electrical stimulation. *Eur. J. Appl. Physiol.* **110,** 223–234. doi:`10.1007/s00421-010-1502-y` (2010).
25. Paillard, T. *et al.* Electrical Stimulation Superimposed onto Voluntary Muscular Contraction. *Sports Med.* **35,** 951–966. doi:`10.2165/00007256-200535110-00003` (2005).
26. Bhadra, N. & Peckham, P. H. Peripheral nerve stimulation for restoration of motor function. *J. clinical neurophysiology* **14,** 378–393. doi:`10.1097/00004691-199709000-00004` (1997).

27. Gorgey, A. S. *et al.* Effects of Electrical Stimulation Parameters on Fatigue in Skeletal Muscle. *J. Orthop. & Sports Phys. Ther.* **39,** 684–692. doi:`10.2519/jospt.2009.3045` (Sept. 2009).
28. Adams, G. R. *et al.* Mapping of electrical muscle stimulation using MRI. *J. Appl. Physiol.* **74,** 532–537. doi:`10.1152/jappl.1993.74.2.532` (Feb. 1, 1993).
29. Cifrek, M. *et al.* Surface EMG based muscle fatigue evaluation in biomechanics. *Clin. Biomech.* **24,** 327–340. doi:`10.1016/j.clinbiomech.2009.01.010` (May 1, 2009).
30. Criswell, E. *Cram's Introduction to Surface Electromyography* 436 pp. (Jones & Bartlett Publishers, Mar. 16, 2010).
31. Tassinary, L. G., Cacioppo, J. T. & Vanman, E. J. in *Handbook of psychophysiology, 3rd ed* 267–299 (Cambridge University Press, New York, NY, US, 2007). doi:`10.1017/CBO9780511546396.012`.
32. Taylor, D. J. Clinical Utility of Muscle MR Spectroscopy. *Semin. Musculoskelet. Radiol.* **4,** 481–502. doi:`10.1055/s-2000-13172` (2000).
33. Hogrel, J.-Y. Clinical applications of surface electromyography in neuromuscular disorders. *Neurophysiol. Clinique/Clinical Neurophysiol.* **35,** 59–71. doi:`10.1016/j.neucli.2005.03.001` (July 1, 2005).
34. Reaz, M. B. I., Hussain, M. S. & Mohd-Yasin, F. Techniques of EMG signal analysis: detection, processing, classification and applications. *Biol. Proced. Online* **8,** 11–35. doi:`10.1251/bpo115` (Dec. 1, 2006).
35. De Graaf, R. A. *In vivo NMR spectroscopy: principles and techniques* (2019).
36. Prost, R. W. Magnetic resonance spectroscopy. *Med. Phys.* **35,** 4530–4544. doi:`10.1118/1.2975225` (2008).
37. Tognarelli, J. M. *et al.* Magnetic Resonance Spectroscopy: Principles and Techniques: Lessons for Clinicians. *J. Clin. Exp. Hepatol.* **5,** 320–328. doi:`10.1016/j.jceh.2015.10.006` (Dec. 1, 2015).
38. Keeler, J. *Understanding NMR Spectroscopy* 2nd edition. 528 pp. (Wiley, Chichester, U.K, May 24, 2010).
39. Van der Graaf, M. In vivo magnetic resonance spectroscopy: basic methodology and clinical applications. *Eur. biophysics journal: EBJ* **39,** 527–540. doi:`10.1007/s00249-009-0517-y` (Mar. 2010).
40. Near, J. *et al.* Preprocessing, analysis and quantification in single-voxel magnetic resonance spectroscopy: experts' consensus recommendations. *NMR Biomed.* **34,** e4257. doi:`10/ghz45z` (2021).
41. Boesch, C. Musculoskeletal spectroscopy. *J. Magn. Reson. Imaging* **25,** 321–338. doi:`10.1002/jmri.20806` (2007).
42. Schenck, J. F. The role of magnetic susceptibility in magnetic resonance imaging: MRI magnetic compatibility of the first and second kinds. *Med. Phys.* **23,** 815–850. doi:`10.1118/1.597854` (1996).
43. Chu, K. C. *et al.* Bulk magnetic susceptibility shifts in nmr studies of compartmentalized samples: use of paramagnetic reagents. *Magn. Reson. Med.* **13,** 239–262. doi:`10.1002/mrm.1910130207` (1990).
44. Boesch, C. *et al.* In vivo determination of intra-myocellular lipids in human muscle by means of localized 1H-MR-spectroscopy. *Magn. Reson. Med.* **37,** 484–493. doi:`10.1002/mrm.1910370403` (1997).
45. Machann, J. *et al.* In Vivo Proton NMR Studies in Skeletal Musculature. *Annu. Reports on NMR Spectrosc.* **50,** 1–74. doi:`10.1016/S0066-4103(03)50001-1` (2003).
46. Bagby, S. in *Encyclopedia of Biophysics* (ed Roberts, G. C. K.) 1163–1168 (Springer, Berlin, Heidelberg, 2013). doi:`10.1007/978-3-642-16712-6_306`.
47. Weber, M.-A. *et al.* Quantitative Imaging in Muscle Diseases with Focus on Non-proton MRI and Other Advanced MRI Techniques. *Semin. Musculoskelet. Radiol.* **24,** 402–412. doi:`10.1055/s-0040-1712955` (Aug. 2020).
48. Krššák, M. *et al.* Proton magnetic resonance spectroscopy in skeletal muscle: Experts' consensus recommendations. *NMR Biomed.* **34,** e4266. doi:`10/gg4qn4` (2021).
49. Machann, J., Stefan, N. & Schick, F. 1H MR spectroscopy of skeletal muscle, liver and bone marrow. *Eur. J. Radiol. Clinical H MR Spectroscopy* **67,** 275–284. doi:`10.1016/j.ejrad.2008.02.032` (2008).
50. Boesch, C. *et al.* Role of proton MR for the study of muscle lipid metabolism. *NMR Biomed.* **19,** 968–988. doi:`10.1002/nbm.1096` (2006).
51. Krssak, M. *et al.* Intramyocellular lipid concentrations are correlated with insulin sensitivity in humans: a 1H NMR spectroscopy study. *Diabetologia* **42,** 113–116. doi:`10.1007/s001250051123` (Jan. 1, 1999).
52. Ntziachristos, V. *et al.* Dipolar resonance frequency shifts in 1H MR spectra of skeletal muscle: Confirmation in rats at 4.7 T in Vivo and observation of changes postmortem. *Magn. Reson. Med.* **38,** 33–39. doi:`10.1002/mrm.1910380107` (1997).
53. Boesch, C. & Kreis, R. Dipolar coupling and ordering effects observed in magnetic resonance spectra of skeletal muscle. *NMR Biomed.* **14,** 140–148. doi:`10.1002/nbm.684` (2001).
54. Edgerton, V. R., Smith, J. L. & Simpson, D. R. Muscle fibre type populations of human leg muscles. *The Histochem. J.* **7,** 259–266. doi:`10.1007/BF01003594` (May 1, 1975).

55. Ren, J. *et al.* Dynamic monitoring of carnitine and acetylcarnitine in the trimethylamine signal after exercise in human skeletal muscle by 7T 1H-MRS. *Magn. Reson. Med.* **69,** 7–17. doi:`10.1002/mrm.24249` (2013).
56. Klepochová, R. *et al.* Muscle Specific Relation of Acetylcarnitine and Intramyocellular Lipids to Chronic Hyperglycemia: A Pilot 3T 1H MRS Study. *Obes. (Silver Spring, Md.)* **28,** 1405–1411. doi:`10.1002/oby.22846` (2020).
57. Boss, A. *et al.* Skeletal muscle 1H MRSI before and after prolonged exercise. II. visibility of free carnitine. *Magn. Reson. Med.* **68,** 1368–1375. doi:`10.1002/mrm.24167` (2012).
58. Bruhn, H. *et al.* Localized Proton NMR spectroscopy using stimulated echoes: Applications to human skeletal muscle invivo. *Magn. Reson. Med.* **17,** 82–94. doi:`10.1002/mrm.1910170113` (Jan. 1991).
59. Da Eira Silva, V. *et al.* Magnetic Resonance Spectroscopy as a Non-invasive Method to Quantify Muscle Carnosine in Humans: a Comprehensive Validity Assessment. *Sci. Reports* **10,** 4908. doi:`10.1038/s41598-020-61587-x` (Mar. 17, 2020).
60. Lievens, E. *et al.* CORP: quantification of human skeletal muscle carnosine concentration by proton magnetic resonance spectroscopy. *J. Appl. Physiol.* **131,** 250–264. doi:`10/gqcfz6` (2021).
61. Baguet, A. *et al.* A New Method for Non-Invasive Estimation of Human Muscle Fiber Type Composition. *PLoS ONE* **6,** e21956. doi:`10/fvmm6p` (July 7, 2011).
62. Özdemir, M. S. *et al.* Absolute quantification of carnosine in human calf muscle by proton magnetic resonance spectroscopy. *Phys. Med. Biol.* **52,** 6781–6794. doi:`10.1088/0031-9155/52/23/001` (Nov. 2007).
63. Fayad, L. M. *et al.* Quantification of Muscle Choline Concentrations by Proton MR Spectroscopy at 3 T: Technical Feasibility. *Am. J. Roentgenol.* **194,** W73–W79. doi:`10.2214/AJR.09.3125` (Jan. 1, 2010).
64. Gao, F. *et al.* The effect of orientation on quantification of muscle creatine by 1H MR spectroscopy. *Magn. Reson. Imaging* **21,** 561–566. doi:`10.1016/S0730-725X(03)00073-0` (June 1, 2003).
65. Bottomley, P. A., Lee, Y. & Weiss, R. G. Total creatine in muscle: imaging and quantification with proton MR spectroscopy. *Radiology.* doi:`10.1148/radiology.204.2.9240527` (Aug. 1, 1997).
66. Boesch, C. & Kreis, R. Observation of Intramyocellular Lipids by 1H-Magnetic Resonance Spectroscopy. *Ann. New York Acad. Sci.* **904,** 25–31. doi:`10.1111/j.1749-6632.2000.tb06417.x` (2000).
67. Schrauwen-Hinderling, V. B. *et al.* Intramyocellular lipid content is increased after exercise in nonexercising human skeletal muscle. *J. Appl. Physiol.* **95,** 2328–2332. doi:`10.1152/japplphysiol.00304.2003` (Dec. 1, 2003).
68. Ren, J., Sherry, A. D. & Malloy, C. R. 1H MRS of intramyocellular lipids in soleus muscle at 7 T: Spectral simplification by using long echo times without water suppression. *Magn. Reson. Med.* **64,** 662–671. doi:`10.1002/mrm.22345` (2010).
69. Meyerspeer, M. *et al.* Direct noninvasive quantification of lactate and high energy phosphates simultaneously in exercising human skeletal muscle by localized magnetic resonance spectroscopy. *Magn. Reson. Med.* **57,** 654–660. doi:`10.1002/mrm.21188` (2007).
70. Ren, J., Sherry, A. D. & Malloy, C. R. Noninvasive monitoring of lactate dynamics in human forearm muscle after exhaustive exercise by 1H-magnetic resonance spectroscopy at 7 tesla. *Magn. Reson. Med.* **70,** 610–619. doi:`10.1002/mrm.24526` (2013).
71. MacMillan, E. L. *et al.* Influence of muscle fiber orientation on water and metabolite relaxation times, magnetization transfer, and visibility in human skeletal muscle. *Magn. Reson. Med.* **75,** 1764–1770. doi:`10.1002/mrm.25778` (2016).
72. Prompers, J. J. *et al.* Dynamic MRS and MRI of skeletal muscle function and biomechanics. *NMR Biomed.* **19,** 927–953. doi:`10.1002/nbm.1095` (2006).
73. Akbari, A. *et al.* Safe MRI-Compatible electrical muscle stimulation (EMS) system: Concurrent MRI and Electrical Stimulation. *J. Magn. Reson. Imaging* **44,** 1530–1538. doi:`10.1002/jmri.25316` (Dec. 2016).
74. Vanderthommen, M. *et al.* A comparison of voluntary and electrically induced contractions by interleaved 1H- and 31P-NMRS in humans. *J. Appl. Physiol.* **94,** 1012–1024. doi:`10.1152/japplphysiol.00887.2001` (Mar. 1, 2003).
75. Aisen, A. M. & Chenevert, T. L. MR spectroscopy: clinical perspective. *Radiology* **173,** 593–599. doi:`10.1148/radiology.173.3.2682768` (Dec. 1, 1989).
76. Zange, J. *et al.* Breakdown of adenine nucleotide pool in fatiguing skeletal muscle in McArdle's disease: A noninvasive 31P-MRS and EMG study. *Muscle & Nerve* **27,** 728–736. doi:`10.1002/mus.10377` (2003).
77. Lodi, R. *et al.* Abnormal in vivo skeletal muscle energy metabolism in Huntington's disease and dentatorubropallidoluysian atrophy. *Ann. Neurol.* **48,** 72–76. doi:`10.1002/1531-8249(200007)48:1<72::AID-ANA11>3.0.CO;2-I` (2000).
78. Kemp, G. J., Meyerspeer, M. & Moser, E. Absolute quantification of phosphorus metabolite concentrations in human muscle in vivo by 31P MRS: a quantitative review. *NMR Biomed.* **20,** 555–565. doi:`10.1002/nbm.1192` (2007).
79. Faro, S. H. & Mohamed, F. B. *Functional MRI: Basic Principles and Clinical Applications* 543 pp. (Springer Science & Business Media, Nov. 22, 2006).

80. Ogawa, S. & Lee, T.-M. Magnetic resonance imaging of blood vessels at high fields: In vivo and in vitro measurements and image simulation. *Magn. Reson. Med.* **16,** 9–18. doi:`10.1002/mrm.1910160103` (1990).
81. Noseworthy, M. D., Bulte, D. P. & Alfonsi, J. BOLD Magnetic Resonance Imaging of Skeletal Muscle. *Semin. Musculoskelet. Radiol.* **7,** 307–316. doi:`10.1055/s-2004-815678` (2003).
82. Logothetis, N. K. The Underpinnings of the BOLD Functional Magnetic Resonance Imaging Signal. *J. Neurosci.* **23,** 3963–3971. doi:`10.1523/JNEUROSCI.23-10-03963.2003` (May 15, 2003).
83. Buxton, R. B. The physics of functional magnetic resonance imaging (fMRI). *Reports on progress physics. Phys. Soc. (Great Britain)* **76,** 096601. doi:`10.1088/0034-4885/76/9/096601` (Sept. 2013).
84. Jacobi, B. *et al.* Skeletal muscle BOLD MRI: From underlying physiological concepts to its usefulness in clinical conditions. *J. Magn. Reson. Imaging* **35,** 1253–1265. doi:`10/gqcfz4` (2012).
85. Joyce, N. C., Oskarsson, B. & Jin, L.-W. Muscle Biopsy Evaluation in Neuromuscular Disorders. *Phys. Med. Rehabil. Clin. North Am. Neuromuscular Disease Management and Rehabilitation, Part I: Diagnostic and Therapy Issues* **23,** 609–631. doi:`10/gqcfz5` (Aug. 1, 2012).
86. Toussaint, J.-F. *et al.* Perfusion changes in human skeletal muscle during reactive hyperemia measured by echo-planar imaging. *Magn. Reson. Med.* **35,** 62–69. doi:`10.1002/mrm.1910350109` (1996).
87. Ledermann, H. .-P. *et al.* Blood Oxygenation Level–Dependent Magnetic Resonance Imaging of the Skeletal Muscle in Patients With Peripheral Arterial Occlusive Disease. *Circulation* **113,** 2929–2935. doi:`10.1161/CIRCULATIONAHA.105.605717` (June 27, 2006).
88. Noseworthy, M. D., Davis, A. D. & Elzibak, A. H. Advanced MR Imaging Techniques for Skeletal Muscle Evaluation. *Semin. Musculoskelet. Radiol.* **14,** 257–268. doi:`10.1055/s-0030-1253166` (June 2010).
89. Partovi, S. *et al.* Blood oxygenation level-dependent (BOLD) MRI of human skeletal muscle at 1.5 and 3 T. *J. Magn. Reson. Imaging* **35,** 1227–1232. doi:`10.1002/jmri.23583` (2012).
90. Wolff, S. D. & Balaban, R. S. Magnetization transfer contrast (MTC) and tissue water proton relaxation in vivo. *Magn. Reson. Med.* **10,** 135–144. doi:`10.1002/mrm.1910100113` (1989).
91. Henkelman, R. M., Stanisz, G. J. & Graham, S. J. Magnetization transfer in MRI: a review. *NMR Biomed.* **14,** 57–64. doi:`10.1002/nbm.683` (2001).
92. Zhu, X. P., Zhao, S. & Isherwood, I. Magnetization transfer contrast (MTC) imaging of skeletal muscle at 0.26 Tesla — changes in signal intensity following exercise. *The Br. J. Radiol.* **65,** 39–43. doi:`10.1259/0007-1285-65-769-39` (Jan. 1992).
93. De Boer, R. Magnetization transfer contrast Part 1: MR physics. *Medicamundi* **40,** 64–73 (1995).
94. Pike, G. B. *et al.* Magnetization transfer time-of-flight magnetic resonance angiography. *Magn. Reson. Med.* **25,** 372–379. doi:`10.1002/mrm.1910250217` (1992).
95. Parker, D. L. *et al.* The application of magnetization transfer to MR angiography with reduced total power. *Magn. Reson. Med.* **34,** 283–286. doi:`10.1002/mrm.1910340221` (1995).
96. Dousset, V. *et al.* Experimental allergic encephalomyelitis and multiple sclerosis: lesion characterization with magnetization transfer imaging. *Radiology.* doi:`10.1148/radiology.182.2.1732968` (Feb. 1, 1992).
97. Grossman, R. I. *et al.* Magnetization transfer: theory and clinical applications in neuroradiology. *RadioGraphics* **14,** 279–290. doi:`10.1148/radiographics.14.2.8190954` (Mar. 1994).
98. Ropele, S. & Fazekas, F. Magnetization Transfer MR Imaging in Multiple Sclerosis. *Neuroimaging Clin. North Am. Multiple Sclerosis, Part II: Nonconventional MRI Techniques* **19,** 27–36. doi:`10.1016/j.nic.2008.09.004` (Feb. 1, 2009).

General Methods

3.1 MRI Acquisitions

The following procedures were applied to all experiments that required the use of a MRI system in this thesis:

- Experiments were performed on a GE Discovery MR750 3T MRI (General Electric Healthcare, Milwaukee, WI) scanner using a GE 16-channel transmit/receive extremity coil.

- Volunteers rested for a period of 30 min laid on a bed located in the MRI patient dressing/holding room prior to any scanning. This is to allow for the normalization of muscle compartment size and blood flow, which have been shown to affect skeletal muscle metabolism, and MRI signals such as ^{1}H-MRS or BOLD techniques [1, 2]. Subjects were moved to the MRI scanner table using an MRI-compatible wheelchair once the rest period finished, always avoiding any strain, movement or weight loading of the leg to be scanned.

- All experiments focused on the right lower leg, looking at the muscle groups shown in Fig. 2.3, the 16-channel T/R coil was wrapped around the lower leg of the participant. Motion artifacts can decrease the data quality by leading to poor ^{1}H-MRS quality due to inhomogeneous excitation and relatively lower resolution and quality of BOLD acquisitions. Therefore, padding was added (including sandbags under the leg and feet and Velcro straps bracing the leg) to reduce the participant's motion during the data acquisition.

- All subjects recruited consented to participate in the experiments under the HiREB-approved research protocol. Subjects received a ∼10 min talk to explain the protocol prior to scanning, including the objectives of the study, the procedure to follow and potential benefits/risks associated with their participation. Subsequently, subjects were preliminarily screened for MRI safety and compatibility with the help of an MRI screening tool assessed by St. Joseph's MRI technologists.

- Prior to MRI scanning, subjects were asked to refrain from performing high-intensity exercise (48h prior to scanning) [2], consuming alcohol (24h prior to scanning) [3], caffeine (24h prior to scanning) [4] as it has been shown to affect the skeletal muscle metabolism and vascular system, hence affecting scans such as ^{1}H-MRS or BOLD.

3.1.1 Sequences

A. **Anatomical reference**: 2D proton density-weighted, fat-suppressed sequence with 15 slices, 256×256 matrix, 4mm thickness, TE/TR/flip = 30/3000ms/111^o, RB = 41.67kHz. The anatomical reference was used as a guide to locating the slices (MT, BOLD) or VOI (^{1}H-MRS) of all other MRI sequences.

B. **Proton spectroscopy**: PRESS sequence, VOI = $20 \times 20 \times 20$mm^3, TE/TR = 30/1500ms, 256 averages, CHESS water suppression. VOI location was placed in the tibialis anterior, guided using an anatomical reference (Sequence A.) to avoid any large fat fascia or other muscle groups (Fig. 3.2).

   Preprocessing: ^{1}H-MRS data was preprocessed using LCModel software [5] (version 6.3). Data was transiently averaged, eddy-current corrected (using the unsuppressed water acquisition) and frequency and phase-corrected with reference to the water peak located at 4.65ppm [6]. Additionally, a 2x zero-filling and Fast Fourier Transform (FFT) was performed.

   Quantification: Further quantification using LCModel used water as internal reference [6] and metabolite ratios were presented as a ratio relative to this peak. The proton

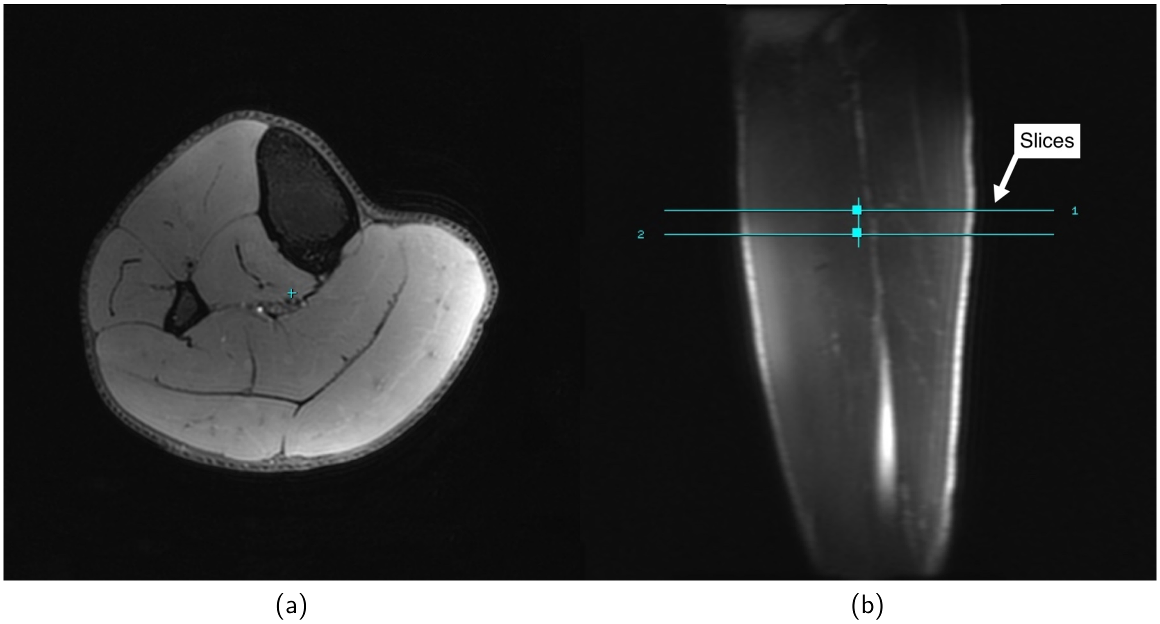

Figure 3.1: Example of the positioning of two slices of interest using an anatomical scan as reference. (Left) Axial and (Right) Sagittal view.

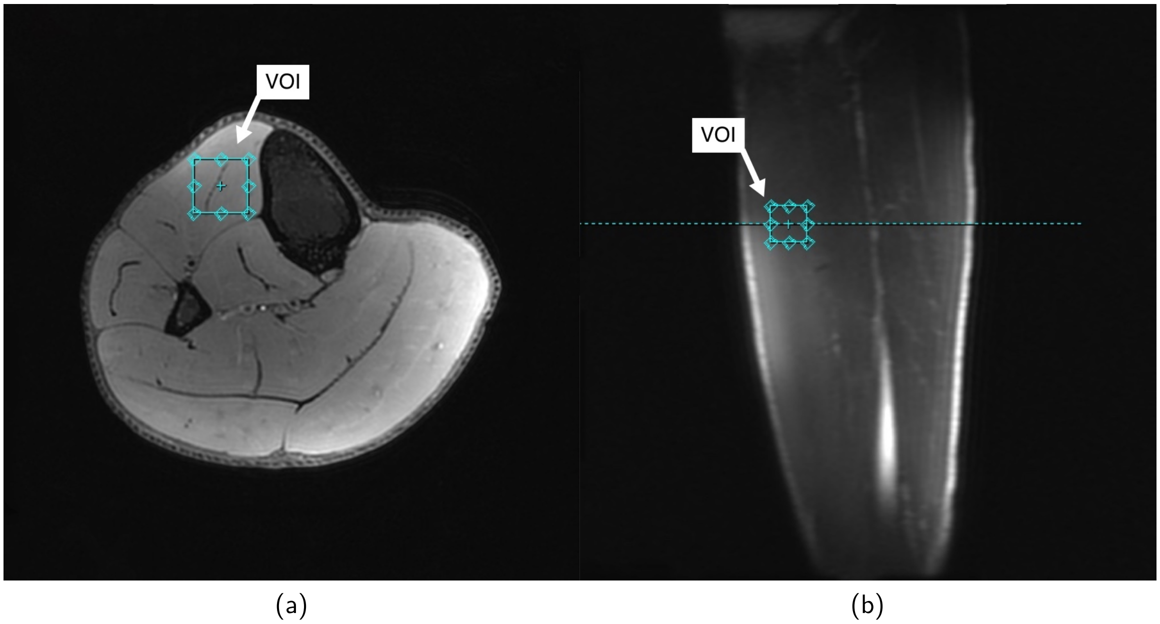

Figure 3.2: Example of the positioning of the VOI in the tibialis anterior muscle using an anatomical scan as reference. (Left) Axial and (Right) Sagittal view.

basis sets used were those included with the LCModel package, specifically for skeletal muscle. All ^{1}H-MRS scans were performed on the TA muscle group (shown in Fig. 2.3) because of its fusiform characteristics (Tbl. 2.5), which decreases the effects of BMS (Chapter 2.2.1) and residual dipolar coupling shifts (Chapter 2.2.1). LCModel is not able to consider the Cr @3.9ppm splitting due to residual dipolar coupling (Section 2.2.1) during the quantification process, which resulted in the exclusion of the Cr @3.9ppm from all experiments analyses.

C. **Magnetization transfer**: 2D spoiled gradient recalled echo, magnetization transfer with 2 slices, 126 × 126 matrix, 10mm thickness, TE/TR/flip = 4.4/100ms/70°, RB = 31.25kHz, with a frequency offset (for M_{SAT}) of 1.5kHz. Additionally, an unsaturated (M_0, no frequency offset) scan was acquired.

D. **BOLD fMRI (TR 110ms)**: 2D gradient echo, EPI, BOLD with 2 slices, 64 × 64 matrix, 10mm thickness, TE/TR/flip = 35/110ms/70°.

E. **BOLD Functional MRI (TR 250ms)**: 2D gradient echo, EPI, BOLD with 2 slices, 64 × 64 matrix, 10mm thickness, TE/TR/flip = 35/250ms/70°.

F. **B_0 mapping**: 2D double gradient-echo, B_0 mapping with 2 slices NO SPACING, 128 × 128 matrix, 10mm thickness, TR/flip = 100ms/20°, RB = 31.25kHz.
Use: the acquired B_0 map was used to correct EPI images, such as the BOLD scans used in this thesis (Sequence D. and E.). This correction is needed because EPI images are sensitive to B_0 inhomogeneities [7, 8].

3.2 EMG acquisition

3.2.1 Disclosure

The design and development of the MRI-compatible EMG acquisition system were done by Joshua Ethan McGillivray. The technical development, characteristics as well as performance tests of the system can be found in [9].

The in-house MRI-compatible EMG acquisition system used for the experiments performed in this thesis has the following characteristics:

- **Frequency bandwidth:** 20-500Hz [10]. Typical EMG recordings can have frequencies of interest up to 1000Hz. The used range is optimized considering the inherent movement of subjects while recording the EMG that will introduce low-frequency motion artifact (<15Hz) and the high-frequency components induced by the MR environment.

- **Amplification:** variable gain to adjust the EMG amplitude within 5V for ADC conversion. The variable gain was configured accounting for an EMG signal between $0.1 - 1\text{mV}$.

- **Sampling rate:** 5kHz. A value higher than the minimum acceptable sampling rate, which is at least twice the highest frequency of the frequency bandwidth [11] (*i.e.* $500\text{Hz} \times 2 = 1\text{kHz}$).

The EMG system included the acquisition circuit, power supplies (Analog Discovery's ±5V) and ADC (National Instruments USB-6221 ADC). The EMG acquisition system required a 30-cm RF-translucent clip electrode leads (Biopac, LEAD108C, Montreal, Quebec, Canada), MRI-compatible EMG adhesive gel carbon electrodes (Cleartrace REF2700-003, Danlee Medical Products, Syracuse, NY), 9-meter long coaxial cable, and a computer (Fig. 3.3). The EMG recordings were taken from the TA muscle of the right leg. The EMG preparation and acquisition pipeline consisted in:

1. Cleaning the skin using alcohol wipes and abrasive gel to improve the impedance matching between the electrodes and the skin.

2. Subject performed a series of plantar/dorsiflexion contractions to palpate and identify the insertion points of the tibialis anterior.

3. MRI-compatible carbon electrodes were placed in the muscle insertion points. The top electrode was placed at the TA superior insertion point close to the proximal tibiofibular joint (avoiding the bone). The other active electrode was placed 7cm apart. This was required as it would leave enough space to place the VOI (from ^{1}H-MRS) or the imaging slices (from MT or BOLD), otherwise, the electrodes could distort the local magnetic field, which would affect image quality.

4. The ground electrode was placed at half the distance between the two active electrodes (3.5cm) but displaced towards the anteroir border of the tibia. The reference electrode was placed on the bone to minimize the electrical signals received during the rest and exercise periods.

5. All electrodes were secured using Micropore paper tape to secure the position of the electrodes through the scanning session.

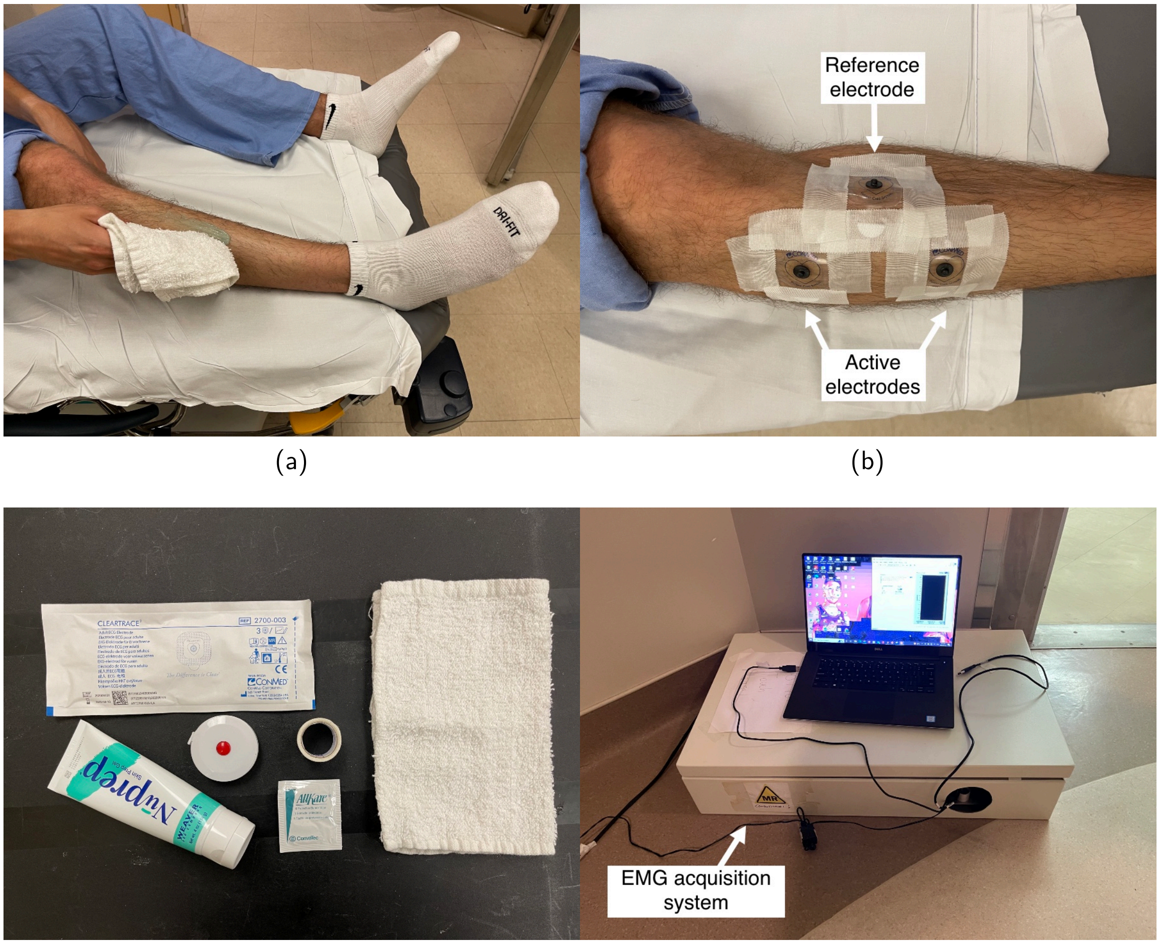

(a) (b)

(c) (d)

Figure 3.3: Set-up of the MRI-compatible EMG acquisition system for the experiments performed (Chapter 8 and 7) in this thesis. The set-up consisted of (a) the application of alcohol and abrasive gel to improve impedance matching between the skin and electrodes. (b) the positioning of the two active and one reference electrodes. (c) the materials used included abrasive gel, alcohol wipes, MRI-compatible electrodes and Micropore paper tape. (d) the positioning of the EMG acquisition system along with the computer used to control, acquire and store the EMG.

3.3 MRI-compatible leg ergometer

3.3.1 Disclosure

The design and development of the MRI-compatible leg ergometer were done by Joshua Ethan McGillivray. The technical development, characteristics as well as performance tests of the system can be found in [9].

As an alternative to electrical stimulation-induced exercise, controlled voluntary exercise can be used to evaluate the metabolic muscle environment by means of MRI. In contrast to the exercise protocol presented in Chapter 6, the use of an MRI-compatible leg ergometer would benefit skeletal muscle research by allowing the use of the ergometer while scanning. The in-house MRI-compatible ergometer used has the following characteristics:

- Its MRI-compatible and fits inside the MRI bore, allowing the use of the ergometer while scanning
- Bilateral feet set-up
- Able to perform plantar/dorsiflexion exercise, extending the range of muscles that can be targeted
- Configurable weight to provide resistance to the plantar/dorsiflexion exercise for each foot, allowing to change the relative effort that each subject will have during the exercise. This will allow the standardization of the exercise to the Maximum Voluntary Contraction (MVC), thus making the analysis comparable between subjects
- Accommodates subjects with height up to 185cm.

The MRI-compatible ergometer used is shown in Fig. 3.4, where the full set-up is shown, including sandbags and Velcro strap to reduce leg motion, extra padding along the subject's back and head to increase comfort, the position of the GE 16-channel T/R extremity coil and the placement of the electrodes for EMG recordings acquisitions.

There are two main types of skeletal muscle contraction: isotonic and isometric [12]. Isotonic contractions (*i.e.* ‘equal tension’) are generated when the muscle shortens and moves. An example of isotonic contractions is lifting weights. On the contrary, isometric contractions (*i.e.* ‘same length’) are developed when the muscle does not shorten, but tension increases. This type of contraction is seen when pushing a pedal or a wall sit. Specific experiments performed in this thesis involved running the MRI while performing the exercise, but because MRI is sensitive to patient motion, the exercise protocol is required to minimize motion. Therefore, isometric exercise was chosen as the muscle length did not change.

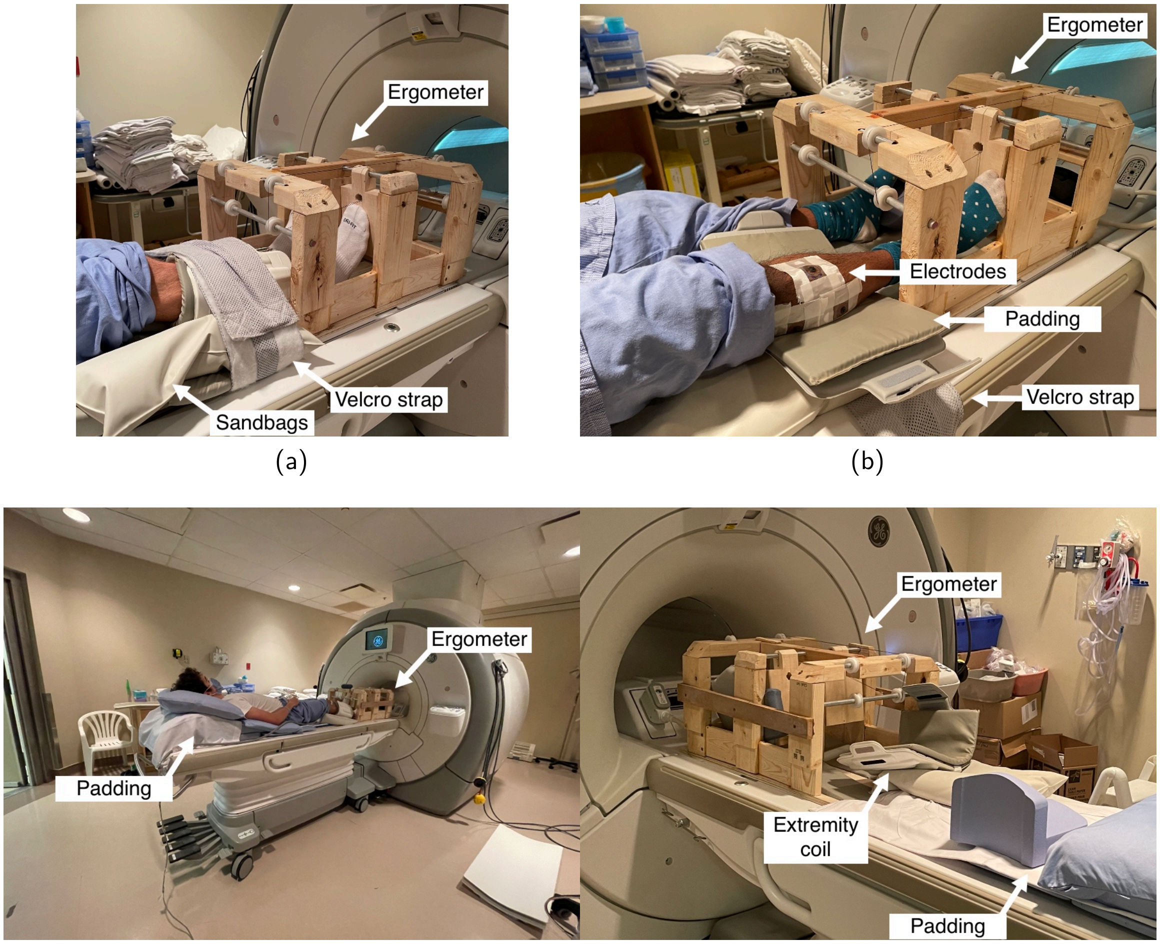

(a) (b)

(c) (d)

Figure 3.4: Set-up of the MRI-compatible leg ergometer inside the MRI magnet room for the experiments performed (Chapter 8 and 7) in this thesis. The set-up consisted of (a) the placement of sandbags and Velcro straps around the leg to reduce motion during scanning. (b) The positioning of the GE 16-channel T/R coil around the lower leg wrapped around the EMG electrodes and leads. (c,d) the extra padding in the back and head to increase comfort.

3.3.2 Maximum Voluntary Contraction measurement

Muscle strength quantification is essential to standardize the experiments that involve the use of exercise. This way, accurate and reliable comparisons can be made across subjects. The Maximum Voluntary Contraction (MVC) level is a measurement commonly used to standardize muscle strength in clinical and research environments, typically being a quick and inexpensive method [13, 14]. A typical MVC measurement consists of exerting the maximum amount of force against a resistance, such as a dynamometer or resistance band, while a specific muscle movement is performed (such as ankle plantarflexion).

The MVC of each subject was measured to standardize the isometric exercise performed on the experiments presented in this thesis at least 24h prior to the MRI scanning. The subject was placed in the supine position on an in-house MRI-compatible exercise device for the lower extremities where, by pushing a pedal, a box containing different weight loads is raised above the ground level. Starting from the lowest weight load available, each subject was asked to push the pedal as far as they were able to. This process was repeated while increasing the weight loads until each subject was not able to fully push the pedal. The previous weight load before the subject was not able to fully push the pedal was considered its MVC measurement (Fig. 3.5).

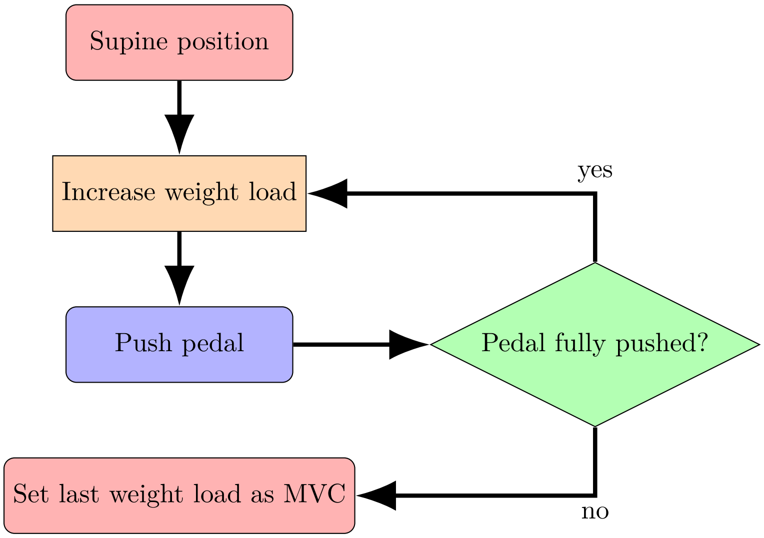

Figure 3.5: Flowchart of the MVC measurement. MVC measurements were performed outside of the MRI environment in the multipurpose IRC room. Estimated measuring time: 5min.

3.4 Data analysis

Unless otherwise mentioned, all data was processed using Matlab (The MathWorks Inc., Natick, USA), and all statistical analyses were performed using R [15]. MRI images that required further preprocessing (such as motion corrections, B_0 corrections, voxel resampling, among others) were performed using the FSL [16–18] and AFNI [19, 20] packages.

References

1. Elzibak, A. H. & Noseworthy, M. D. Assessment of diffusion tensor imaging indices in calf muscles following postural change from standing to supine position. *Magma* **27,** 387–395. doi:`10/f6h87p` (2014).
2. Vermathen, P. *et al.* Skeletal muscle 1H MRSI before and after prolonged exercise. I. muscle specific depletion of intramyocellular lipids. *Magn. Reson. Med.* **68,** 1357–1367. doi:`10/fznjv8` (2012).
3. Esposito, F. *et al.* Alcohol increases spontaneous BOLD signal fluctuations in the visual network. *NeuroImage* **53,** 534–543. doi:`10.1016/j.neuroimage.2010.06.061` (Nov. 1, 2010).
4. Yang, H.-C. *et al.* Vascular effects of caffeine found in BOLD fMRI. *J. Neurosci. Res.* **97,** 456–466. doi:`10.1002/jnr.24360` (2019).
5. Provencher, S. W. Estimation of metabolite concentrations from localized in vivo proton NMR spectra. *Magn. Reson. Med.* **30,** 672–679. doi:`10.1002/mrm.1910300604` (1993).
6. Krššák, M. *et al.* Proton magnetic resonance spectroscopy in skeletal muscle: Experts' consensus recommendations. *NMR Biomed.* **34,** e4266. doi:`10/gg4qn4` (2021).
7. Durand, E. *et al.* Artifact due to B0 fluctuations in fMRI: Correction using the k-space central line. *Magn. Reson. Med.* **46,** 198–201. doi:`10.1002/mrm.1177` (2001).
8. Vardal, J. *et al.* Correction of B0-Distortions in Echo-Planar-Imaging–Based Perfusion-Weighted MRI. *J. Magn. Reson. Imaging* **39,** 722–728. doi:`10.1002/jmri.24213` (2014).
9. McGillivray, J. *A Non Invasive Complex Representation of Muscle: A Description through BOLD Fractal Dimension, Phase Space, and Concurrent EMG Metrics* Thesis (McMaster University, Nov. 2022).
10. Van Duinen, H. *et al.* Surface EMG measurements during fMRI at 3T: Accurate EMG recordings after artifact correction. *NeuroImage* **27,** 240–246. doi:`10.1016/j.neuroimage.2005.04.003` (Aug. 1, 2005).
11. Merletti, R. & Di Torino, P. Standards for reporting EMG data. *J Electromyogr Kinesiol.* **9,** 3–4. doi:`10.1016/s1050-6411(97)90001-8` (1999).
12. Marieb, E. N. & Hoehn, K. *Human anatomy & physiology* (Pearson education, 2007).
13. Meldrum, D. *et al.* Maximum voluntary isometric contraction: Reference values and clinical application. *Amyotroph. Lateral Scler.* **8,** 47–55. doi:`10.1080/17482960601012491` (Jan. 1, 2007).
14. Conable, K. M. & Rosner, A. L. A narrative review of manual muscle testing and implications for muscle testing research. *J. Chiropr. Med.* **10,** 157–165. doi:`10.1016/j.jcm.2011.04.001` (Sept. 2011).
15. Team, R. C. *R: The R Project for Statistical Computing* `https://www.r-project.org/` (2023).
16. Jenkinson, M. *et al.* FSL. *NeuroImage. 20 YEARS OF fMRI* **62,** 782–790. doi:`10.1016/j.neuroimage.2011.09.015` (Aug. 15, 2012).
17. Smith, S. M. *et al.* Advances in functional and structural MR image analysis and implementation as FSL. *NeuroImage. Mathematics in Brain Imaging* **23,** S208–S219. doi:`10.1016/j.neuroimage.2004.07.051` (Jan. 1, 2004).
18. Woolrich, M. W. *et al.* Bayesian analysis of neuroimaging data in FSL. *NeuroImage. Mathematics in Brain Imaging* **45,** S173–S186. doi:`10.1016/j.neuroimage.2008.10.055` (Mar. 1, 2009).
19. Cox, R. W. AFNI: Software for Analysis and Visualization of Functional Magnetic Resonance Neuroimages. *Comput. Biomed. Res.* **29,** 162–173. doi:`10.1006/cbmr.1996.0014` (June 1, 1996).
20. Cox, R. W. & Hyde, J. S. Software tools for analysis and visualization of fMRI data. *NMR Biomed.* **10,** 171–178. doi:`10.1002/(SICI)1099-1492(199706/08)10:4/5<171::AID-NBM453>3.0.CO;2-L` (1997).

Skeletal muscle proton spectroscopy quantification: a repeatability analysis

4.1 Disclosure

This chapter was written by Alejandro Amador-Tejada and is part of a collaboration with Dr. Michael D. Noseworthy. This chapter has been accepted as a conference abstract for the *2023 ISMRM & ISMRT Annual Meeting & Exhibition* from the $03^{\text{th}} - 08^{\text{th}}$ June 2023 in Toronto, ON, Canada.

4.2 Background

^{1}H-MRS has been used to study the IMCL and EMCL content in healthy populations [1, 2], the relationship of IMCL to insulin sensitivity [3, 4], as well as its evolution during exercise [5, 6]. In addition to lipids, other metabolites such as creatine [7–9], carnosine [10–12], and acetyl-carnitine [5, 6] have been studied. Nevertheless, skeletal muscle ^{1}H-MRS presents a series of challenges, such as Bulk Magnetic Susceptibility shifts and residual dipolar coupling effects due to the highly ordered structure of skeletal muscle. These make visibility and quantification of metabolites orientation-dependent (relative to B_0), muscle-dependent and voxel sensitive [13, 14]. Ensuring an accurate metabolite quantification is crucial as ^{1}H-MRS is increasingly utilized in research and clinical settings to study muscle metabolism, MSK disorders and sports science [13].

4.2.1 Bulk magnetic susceptibility shifts

Bulk Magnetic Susceptibility (BMS) shifts on lipids in ^{1}H-MRS of skeletal muscle were first reported in the early 1990s [15], where the existence of two lipid compartments was suggested with a chemical shift of $\sim$ 0.2ppm between them. These observations were confirmed by studying the angular dependence relative to B_0 of the two metabolites peaks in the tibialis anterior muscle showing that EMCL and IMCL are stored in different geometries within the muscle, results that were demonstrated through electron micrographs [2, 16–18].

4.2.2 Residual dipolar coupling

Another effect seen on proton spectroscopy of skeletal muscle is residual dipolar coupling, which was first observed in *in vivo* ^{1}H-MRS in the early 1990s [19]. This was observed by investigating the frequency shift of certain metabolites in response to an increase in the angle of the tibialis anterior muscle relative to B_0, and by means of 2D J-resolved spectroscopy and double-quantum filtered spectrally editing sequences. This effect was later confirmed with a rat model [20], where the main metabolite showing this effect was creatine at 4ppm.

Overall, the metabolites in skeletal muscle that have demonstrated an orientation-dependent behaviour attributable to dipolar coupling are creatine [21], carnosine [22], taurine [23], and lactate [24]. This effect disappears at the magic angle, thus causing a collapse of the splittings of multiplets into singlets [14].

4.2.3 Need to Assess Proton MRS Stability

Therefore, considering all the challenges that ^{1}H-MRS faces, the overall study of the biochemical environment of skeletal muscle by means of this technique is troublesome. Previous research on specific ^{1}H-MRS metabolites did not assess the stability and reproducibility of the ^{1}H-MRS spectra of skeletal muscle. This lack of stability and reproducibility may compromise the results or findings of studies, specifically those requiring spectra acquisition at multiple time points.

Consequently, the aim of this study was to assess the repeatability of ^{1}H-MRS metabolite quantification of skeletal muscle in healthy subjects by means of a test-retest study. To the authors' knowledge, this has only been performed on lipids [25], which have been reported to vary with diet and training status [26].

4.3 Methods

Five healthy male volunteers (age $= 25 \pm 3$yrs, height $= 178 \pm 2$cm, weight $= 77 \pm 8$kg) were recruited. Experiments were performed accordingly to the MRI general methods (Chapter 3.1). The protocol consisted of the acquisition of six ^{1}H-MRS spectra acquired from the tibialis anterior muscle group, using a ^{1}H-MRS sequence (described in Sequence B.). The prescan values (shim, centre frequency, transmit/receive gains) were kept constant for all spectra based on values obtained from the first acquisition, as any adjustments could alter the field homogeneity between scans and thus affect the inter-scan linewidth and spectra quality [27]. A second scan was performed on two of the volunteers 1-2 days after the first scan, the remaining volunteers had a second scan performed 120 minutes after the first (1.5 hours free + 30 min of supine resting) to simulate two independent scans. Similar to the first scan, six more ^{1}H-MRS were acquired during the second scan (Fig. 4.1). To reproduce the same VOI for ^{1}H-MRS in both sessions, a vitamin E pill was placed on the skin of the calf muscle (at the muscle belly) as a landmark (as shown in the example of the VOI positioning in Fig. 4.2).

Data were analyzed and quantified as described in Sequence B.. A repeated measures Analysis of Covariance (ANCOVA) was performed to assess the differences in the mean metabolite ratio across scanning sessions, with the unsuppressed water peak Full Width at Half Maximum (FWHM), a metric indicative of shim quality, used as a covariate.

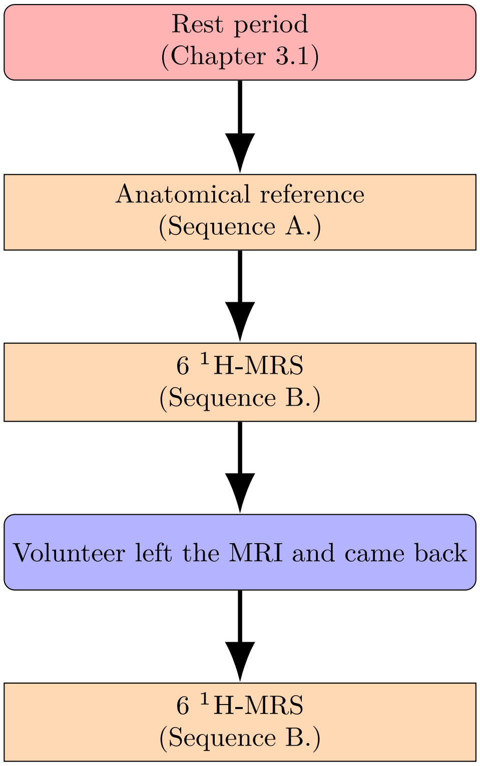

Figure 4.1: Flowchart of the data acquisition protocol. Estimated scanning time: 2 independent scans of 60min.

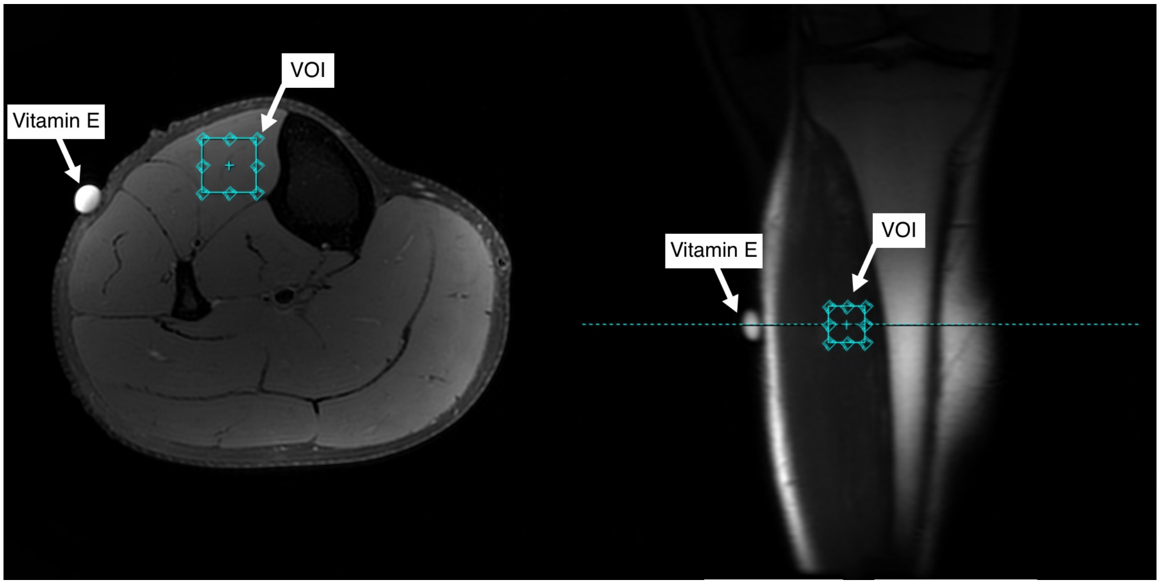

(a) (b)

Figure 4.2: ^{1}H-MRS VOI positioning using an anatomical scan as reference (Sequence A.) in the tibialis anterior muscle of the lower leg. To reproduce the VOI position across experiment sessions, a vitamin E pill was placed on the skin of the calf muscle as a landmark.

4.4 Results

A total of 90 ^{1}H-MRS spectra were collected from five volunteers across two sessions. The average FWHM for the unsuppressed water peak was 13 ± 0.5Hz across all spectra, meaning that data had a good spectral resolution. The maximum acceptable water linewidth is $\sim$25Hz for skeletal muscle on a 3T scanner [10, 13]. A boxplot of the 12 metabolites included in the analysis is shown in Fig. 4.3. Repeated measures ANCOVA were performed with metabolite, experimental session (*i.e.* two) and subject as factors, and the FWHM as confounding variable. Results showed no significant difference in the mean ratio of metabolites across experiment sessions ($p = 0.185$) and in the interaction between experiments and metabolite ($p = 0.939$). On the other hand, the mean metabolite ratio between metabolites and subjects was statistically significant ($p < 0.001$), as shown in Fig. 4.4. Furthermore, multiple comparisons between scanning sessions for each metabolite showed a statistical difference only for the EMCL peak at 1.5ppm ($p < 0.05$) as shown in Fig. 4.5, with the estimated marginal means for each metabolite for both experimental conditions shown in Table 4.1. Finally, the FWHM covariate was not significant ($p = 0.950$).

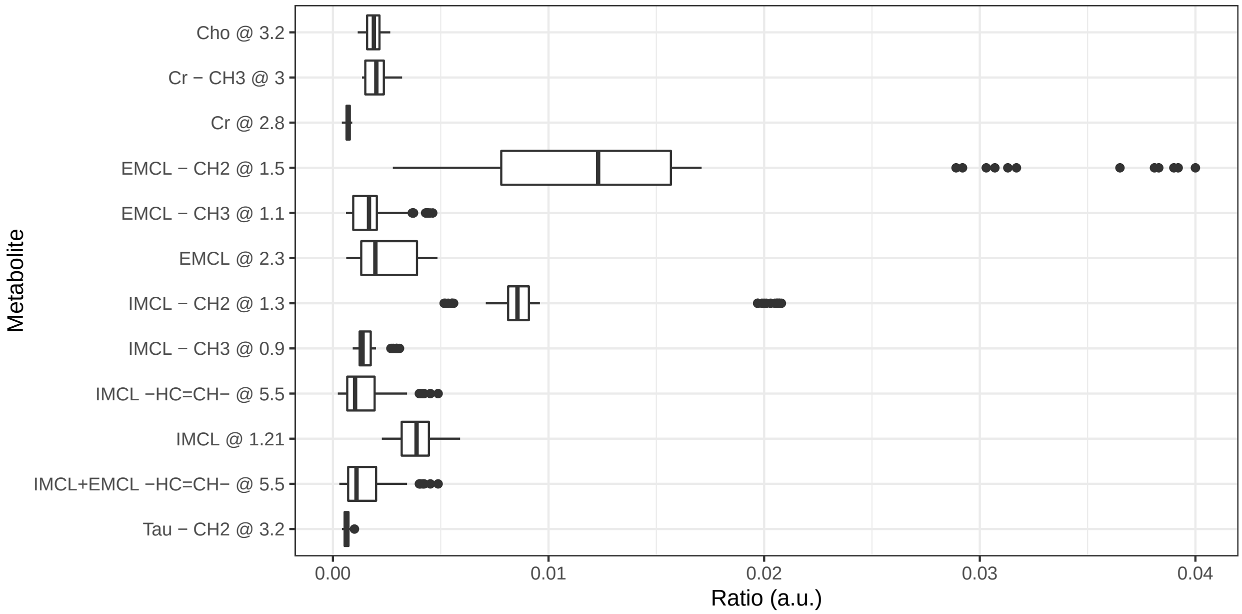

Figure 4.3: Exploratory boxplot for each metabolite ratio across subjects and experiments. The metabolites that showed high variability were both IMCL and EMCL. On the other hand, Tau, Cr and Cho showed low variability.

```
## Type III Analysis of Variance Table
##                           Sum Sq    Mean Sq DF F value    Pr(>F)
## metabolite            0.0123503 0.00112276 11 85.8122 < 2.2e-16 ***
## experiment            0.0000231 0.00002306  1  1.7627    0.1848
## fwhm                  0.0000001 0.00000005  1  0.0039    0.9502
## subject               0.0006492 0.00016231  4 12.4054 1.026e-09 ***
## metabolite:experiment 0.0000631 0.00000573 11  0.4383    0.9388
## ---
## Signif. codes:  0 '***' 0.001 '**' 0.01 '*' 0.05 '.' 0.1 ' ' 1
```

Figure 4.4: Repeated measurements ANCOVA results. The model included the metabolites, experimental sessions, subjects and the interaction between metabolites and experimental sessions as factors while the peak FWHM was included in the model as a covariate. Results show no statistical difference in the mean metabolite ratio between experiments 1 and 2 ($p = 0.185$), and the interaction between metabolites and experimental sessions ($p = 0.950$). The peak FWHM covariate was not significant ($p = 0.939$). On the contrary, the mean metabolite ratio was significant between metabolites and subjects ($p < 0.001$).

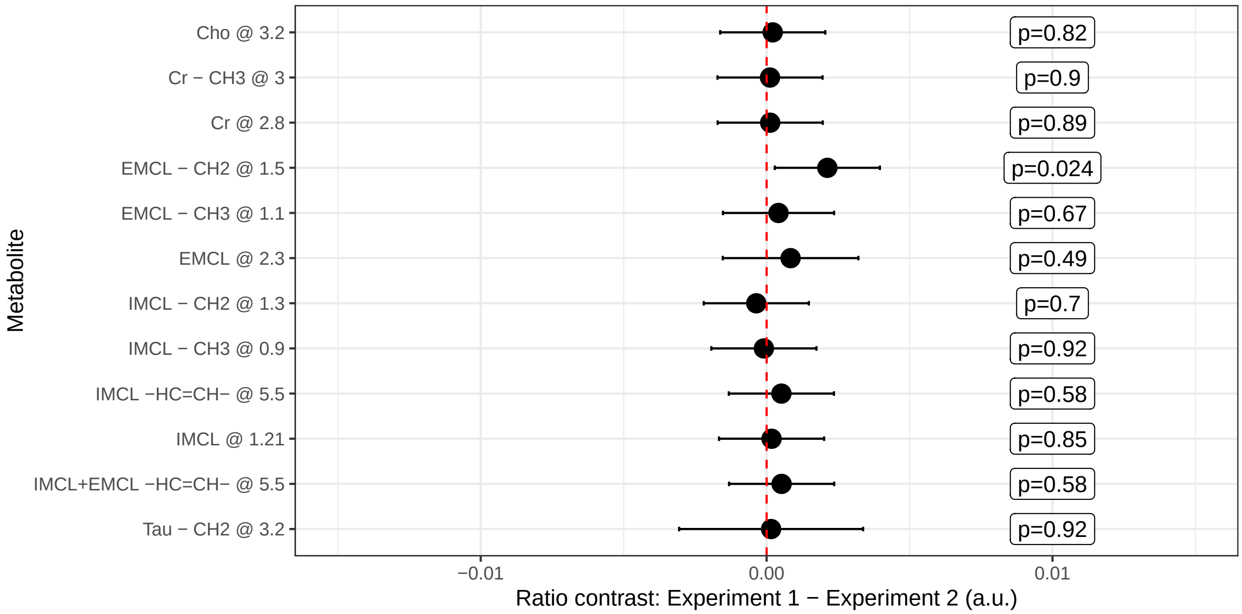

Figure 4.5: Post hoc analysis of the mean metabolite ratio between experiments. It is seen that EMCL – CH2 at 1.5ppm shows a significant difference between experiments ($p < 0.05$).

Table 4.1: Estimated mean and standard error of the metabolite ratio between experiment 1 and experiment 2.

Metabolite	Experiment 1	Experiment 2
Cho @ 3.2	0.00197 ± 7e-04	0.00176 ± 7e-04
Cr - CH3 @ 3	0.00213 ± 7e-04	0.00201 ± 7e-04
Cr @ 2.8	0.00075 ± 7e-04	0.00063 ± 7e-04
EMCL - CH2 @ 1.5	0.01596 ± 7e-04	0.01384 ± 7e-04
EMCL - CH3 @ 1.1	0.00209 ± 7e-04	0.00168 ± 7e-04
EMCL @ 2.3	0.00246 ± 7e-04	0.00162 ± 0.001
IMCL - CH2 @ 1.3	0.01029 ± 7e-04	0.01065 ± 7e-04
IMCL - CH3 @ 0.9	0.00162 ± 7e-04	0.00172 ± 7e-04
IMCL -HC=CH- @ 5.5	0.00175 ± 7e-04	0.00123 ± 7e-04
IMCL @ 1.21	0.00392 ± 7e-04	0.00374 ± 7e-04
IMCL+EMCL -HC=CH- @ 5.5	0.0018 ± 7e-04	0.00127 ± 7e-04
Tau - CH2 @ 3.2	0.0017 ± 0.0011	0.00155 ± 0.0012

4.5 Discussion

The statistical difference between metabolites was expected since each metabolite shows a different concentration in skeletal muscle. Furthermore, previous studies have shown that metabolites change according to a person's habits (e.g. diet and exercise), which explains the statistical difference between subjects. The FWHM (a measurement of the system shim and subsequent data quality) did not influence the experimental design and thus can be disregarded. The mean metabolite ratios showed no statistical difference between scans, attributed to our robust and repeatable data acquisition strategy. However, even with our robust approach, a statistical difference between scans for the EMCL – CH2 at 1.5ppm was noted, which has been reported to be highly dependent on VOI positioning. The non-significance from the ANCOVA test and the significance for EMCL – CH2 at 1.5ppm between experiments might appear contradictory. Nevertheless, the ANCOVA tests for differences in the mean ratio across experiments, accounting for the variance of the metabolites included in the analysis, which states that the overall mean ratio was not significant between experiments. On the other hand, post hoc analysis of the mean ratio for each metabolite between experiments showed that EMCL – CH2 at 1.5ppm is significant.

This chapter showed high repeatability of skeletal muscle metabolites across scans of ^{1}H-MRS in healthy subjects. It is thought that this was achieved by using a proper set-up, including the prevention of any leg motion and reproducible landmarks to place the VOI in the same location across sessions. Even more, the stability of the MRI system used while scanning a ^{1}H-MRS was seen to be reliable due to the FWHM not contributing to the experimental variability.

Further studies should be conducted with a larger and sex-equilibrated population, with a longer time gap between sessions and controlling external factors such as diet and exercise to assess the overall repeatability and variability of ^{1}H-MRS of skeletal muscle. Overall, the results in this chapter encourage the study of all visible ^{1}H-MRS metabolites in skeletal muscle to look at its biochemical environment.

References

1. Nakagawa, Y. & Hattori, M. Intramyocellular lipids of muscle type in athletes of different sport disciplines. *Open Access J. Sports Med.* **8,** 161–166. doi:`10.2147/OAJSM.S139801` (2017).
2. Szczepaniak, L. S. *et al.* Bulk magnetic susceptibility effects on the assessment of intra- and extramyocellular lipids in vivo. *Magn. Reson. Med.* **47,** 607–610. doi:`10.1002/mrm.10086` (2002).
3. Boesch, C. *et al.* Role of proton MR for the study of muscle lipid metabolism. *NMR Biomed.* **19,** 968–988. doi:`10.1002/nbm.1096` (2006).
4. Klepochová, R. *et al.* Muscle Specific Relation of Acetylcarnitine and Intramyocellular Lipids to Chronic Hyperglycemia: A Pilot 3T 1H MRS Study. *Obes. (Silver Spring, Md.)* **28,** 1405–1411. doi:`10.1002/oby.22846` (2020).
5. Ren, J. *et al.* Dynamic monitoring of carnitine and acetylcarnitine in the trimethylamine signal after exercise in human skeletal muscle by 7T 1H-MRS. *Magn. Reson. Med.* **69,** 7–17. doi:`10.1002/mrm.24249` (2013).
6. Vermathen, P. *et al.* Skeletal muscle 1H MRSI before and after prolonged exercise. I. muscle specific depletion of intramyocellular lipids. *Magn. Reson. Med.* **68,** 1357–1367. doi:`10/fznjv8` (2012).
7. Kreis, R. *et al.* Effect of Exercise on the Creatine Resonances in 1H MR Spectra of Human Skeletal Muscle. *J. Magn. Reson.* **137,** 350–357. doi:`10.1006/jmre.1998.1683` (1999).
8. Subhawong, T. K. *et al.* 1H Magnetic Resonance Spectroscopy Findings in Idiopathic Inflammatory Myopathies at 3 T: Feasibility and First Results. *Investig. Radiol.* **48,** 509–516. doi:`10.1097/RLI.0b013e3182823562` (July 2013).
9. Bottomley, P. A., Lee, Y. & Weiss, R. G. Total creatine in muscle: imaging and quantification with proton MR spectroscopy. *Radiology.* doi:`10.1148/radiology.204.2.9240527` (Aug. 1, 1997).
10. Lievens, E. *et al.* CORP: quantification of human skeletal muscle carnosine concentration by proton magnetic resonance spectroscopy. *J. Appl. Physiol.* **131,** 250–264. doi:`10/gqcfz6` (2021).
11. Louie, E. A. *et al.* Transverse relaxation and magnetization transfer in skeletal muscle: Effect of pH. *Magn. Reson. Med.* **61,** 560–569. doi:`10.1002/mrm.21847` (2009).
12. Özdemir, M. S. *et al.* Absolute quantification of carnosine in human calf muscle by proton magnetic resonance spectroscopy. *Phys. Med. Biol.* **52,** 6781–6794. doi:`10.1088/0031-9155/52/23/001` (Nov. 2007).
13. Krššák, M. *et al.* Proton magnetic resonance spectroscopy in skeletal muscle: Experts' consensus recommendations. *NMR Biomed.* **34,** e4266. doi:`10/gg4qn4` (2021).
14. Machann, J. *et al.* In Vivo Proton NMR Studies in Skeletal Musculature. *Annu. Reports on NMR Spectrosc.* **50,** 1–74. doi:`10.1016/S0066-4103(03)50001-1` (2003).
15. Schick, F. *et al.* Comparison of localized proton NMR signals of skeletal muscle and fat tissue in vivo: Two lipid compartments in muscle tissue. *Magn. Reson. Med.* **29,** 158–167. doi:`10.1002/mrm.1910290203` (1993).
16. Boesch, C. & Kreis, R. MR-Spectroscopy (MRS) of Different Nuclei Applied to Human Muscle: Additional Information Obtained by 1H-MRS. *Int. J. Sports Med.* **18,** S310–S312. doi:`10.1055/s-2007-972739` (S 4 Oct. 1997).
17. Boesch, C. & Kreis, R. Observation of Intramyocellular Lipids by 1H-Magnetic Resonance Spectroscopy. *Ann. New York Acad. Sci.* **904,** 25–31. doi:`10.1111/j.1749-6632.2000.tb06417.x` (2000).
18. Krssak, M. *et al.* Intramyocellular lipid concentrations are correlated with insulin sensitivity in humans: a 1H NMR spectroscopy study. *Diabetologia* **42,** 113–116. doi:`10.1007/s001250051123` (Jan. 1, 1999).
19. Kreis, R. & Boesch, C. Liquid-Crystal-like Structures of Human Muscle Demonstrated by in Vivo Observation of Direct Dipolar Coupling in Localized Proton Magnetic Resonance Spectroscopy. *J. Magn. Reson. Ser. B* **104,** 189–192. doi:`10.1006/jmrb.1994.1075` (June 1, 1994).
20. Ntziachristos, V. *et al.* Dipolar resonance frequency shifts in 1H MR spectra of skeletal muscle: Confirmation in rats at 4.7 T in Vivo and observation of changes postmortem. *Magn. Reson. Med.* **38,** 33–39. doi:`10.1002/mrm.1910380107` (1997).
21. Boesch, C. & Kreis, R. Dipolar coupling and ordering effects observed in magnetic resonance spectra of skeletal muscle. *NMR Biomed.* **14,** 140–148. doi:`10.1002/nbm.684` (2001).
22. Schröder, L. & Bachert, P. Evidence for a dipolar-coupled AM system in carnosine in human calf muscle from in vivo 1H NMR spectroscopy. *J. Magn. Reson.* **164,** 256–269. doi:`10.1016/S1090-7807(03)00205-2` (Oct. 1, 2003).
23. Schröder, L., Schmitz, C. & Bachert, P. Molecular dynamics and information on possible sites of interaction of intramyocellular metabolites in vivo from resolved dipolar couplings in localized 1H NMR spectra. *J. Magn. Reson.* **171,** 213–224. doi:`10.1016/j.jmr.2004.08.015` (Dec. 1, 2004).

24. Asllani, I. *et al.* Anisotropic Orientation of Lactate in Skeletal Muscle Observed by Dipolar Coupling in 1H NMR Spectroscopy. *J. Magn. Reson.* **139,** 213–224. doi:`10.1006/jmre.1999.1774` (Aug. 1, 1999).
25. Torriani, M. *et al.* Intramyocellular Lipid Quantification: Repeatability with 1H MR Spectroscopy. *Radiology* **236,** 609–614. doi:`10.1148/radiol.2362041661` (2005).
26. Machann, J., Stefan, N. & Schick, F. 1H MR spectroscopy of skeletal muscle, liver and bone marrow. *Eur. J. Radiol. Clinical H MR Spectroscopy* **67,** 275–284. doi:`10.1016/j.ejrad.2008.02.032` (2008).
27. Juchem, C. *et al.* B0 shimming for in vivo magnetic resonance spectroscopy: Experts' consensus recommendations. *NMR Biomed.* **34,** e4350. doi:`10.1002/nbm.4350` (2021).

An examination of the fiber composition of skeletal muscle using proton spectroscopy

5.1 Disclosure

This chapter was written by Alejandro Amador-Tejada with the intention of publishing as part of an original research paper in collaboration with Joshua Ethan McGillivray and Dr. Michael D. Noseworthy. The intended author's order is Joshua Ethan McGillivray, Alejandro Amador-Tejada and Dr. Michael D. Noseworthy. The planned publication is awaiting biopsy confirmation for the skeletal muscle fiber profile.

Additionally, this chapter was presented as a conference abstract for the *McMaster Engineering Technology Research and Innovation Conference (METRIC)* on October 29th, 2022, in Hamilton, ON, Canada.

5.2 Background

Skeletal muscle fiber composition is highly heterogeneous between humans due to the different training statuses and capacities of individuals [1]. Type I (slow-twitch, ST) fibers are specialized for long-duration exercise, mainly found in endurance athletes. On the contrary, type II (fast-twitch, FT, type A & X) fibers are more common in short-duration training, being dominant in strength and power athletes [2]. Skeletal muscle tissue has great plasticity, *i.e.* it has the ability to adjust to the demands imposed on it, ranging from nutritional to training changes, among others [3]. Skeletal muscle can respond to these factors in multiple ways, for instance, by changing its architecture, fiber type distribution, length or diameter [4].

The fiber composition of skeletal muscle has been extensively studied in humans. In sports science, this has been used to assess the effects of training in fiber plasticity, to personalize the exercise routines for elite athletes based on the target outcome (either endurance or power benefits), and to track the evolution of muscle fibers profiles during the training course [5, 6]. Moreover, individuals differ in the ratio of muscle fiber types that have different metabolic profiles, which not only affect the function of the muscle group but also influence its susceptibility to certain diseases [7] such as muscle atrophy, diabetes and neuromuscular diseases [8, 9]. Therefore, the investigation of muscle fiber profiles can help to understand, assess and follow the evolution of muscular diseases. For example, type II fiber degenerates in Duchenne Muscular Dystrophy (DMD) [7], and studies have suggested the promotion of endurance exercise (fiber type I) as a therapeutic approach to delay the progression of DMD [10]. Another example is diabetes, where there is a reduction in the proportion of type I and an increase in type II(X) fibers [11]; or sarcopenia, *i.e.* the loss of muscle mass due to aging, where a significant reduction of type II fiber is observed [7]. Therefore the identification of muscle fibre type ratios and how they vary from the norm could be used as a diagnostic measure for DMD, diabetes, sarcopenia and other muscular disorders.

Since the early 1970s, the most common technique to assess muscle fiber type is a biopsy [5, 12, 13], however, despite its utility, this technique is invasive and can cause discomfort to patients, such as minor pain and stiffness. Additionally, since it involves taking a sample of the muscle, it can not be repeated frequently, and it only provides a localized rather than a complete view of the targeted muscle [14]. Moreover, in order to monitor and follow up with patients, multiple biopsies from the affected muscle may be necessary, which raises the risk of developing inflammatory reactions or muscle damage [14].

Thus, a non-invasive assessment of fiber type that can be performed multiple times without causing discomfort and that provides a larger picture of the muscle group profile would be a valuable tool in sports medicine and in the study of neuromuscular diseases. ^{1}H-MRS has been proposed as an alternative, previous studies have shown that carnosine concentration is higher in power/strength (FT) vs endurance (ST) athletes [5]. Nevertheless, its low amplitude (close to baseline levels) and its pH dependence [15, 16] hampers its translation to clinic applications. Even more, a complete characterization of the metabolic profile (with metabolites such as creatine, TMA, EMCL and IMCL) between FT and ST fibers has not been investigated. As such, this chapter aimed to study the metabolic profile of the lower leg muscles between endurance and power/strength classified subjects through ^{1}H-MRS.

5.3 Methods

Eight healthy active male subjects (age = 26 ± 2.4yrs, height = 178 ± 5.6cm, weight = 71 ± 9.2kg) were recruited. Experiments were performed accordingly to the MRI general methods (Chapter 3.1). The protocol consisted of the acquisition of an ^{1}H-MRS (described in Sequence B.) placing the VOI on the tibialis anterior muscle. In addition, subjects were qualitatively classified as dominantly slow or fast-twitch based on their habitual physical activity [2, 17, 18] prior to scanning as shown in Table 5.1. The data acquisition protocol included a rest period, an anatomical reference and an ^{1}H-MRS sequence, as shown in Fig. 5.1.

After preprocessing the ^{1}H-MRS datasets (described in Sequence B.), data were exported for an in-house quantification analysis based on a metabolite ratio against water using Matlab (The MathWorks Inc., Natick, USA), which is one of the quantification methods extensively used in the research community [19]. Furthermore, Cr @3.01ppm is the usual reference peak, but it is not clearly dominant in skeletal muscle, hence supporting the use of water as the reference peak [20, 21]. The analysis included the following steps:

1. Selection of the metabolites to analyze, their peak centre frequency and their integration window (corresponding to twice the average FWHM of each peak [15]) to extract the corresponding peak signal from the spectra. The metabolites analyzed and their integration ranges are shown in Table 5.2.

2. The ^{1}H-MRS signal is a superposition of resonance frequencies from metabolites, macromolecules and proteins, among others. Macromolecules and proteins have a short T_2^*, thus they will appear on the ^{1}H-MRS spectra as broad, low amplitude

resonances peaks under the metabolite peaks [22]. A detrending procedure to suppress the macromolecules and protein amplitudes from the spectra was performed [19, 20].

3. Computation of peak integration of the absolute metabolite peak signal.

4. Computation of ratio of the metabolite of interest and the water peak as shown in Eqn. 5.1.

$$\mathrm{ratio}_{\mathrm{metabolite}} = \frac{\int_{-\delta}^{+\delta} \mid \mathrm{metabolite}_{\mathrm{detrended}} \mid \mathrm{dppm}}{\int_{-0.2\mathrm{ppm}}^{+0.2\mathrm{ppm}} \mid \mathrm{water}_{\mathrm{detrended}} \mid \mathrm{dppm}} \tag{5.1}$$

After the quantification was performed, an independent t-test was used to determine if there were statistically significant differences in the mean of the metabolite-to-water ratio between slow and fast-twitch groups.

Table 5.1: Habitual physical activities and the qualitatively assigned fiber classification of the participants.

Subject #	Physical activity	Fiber classification
1	Distance running	Slow-twitch
2	Distance running	
3	Distance running	
4	Distance running	
5	Weightlifting	Fast-twitch
6	Hockey	
7	Soccer	
8	Fencing	

Table 5.2: List of ^{1}H-MRS metabolites included in the quantification analysis with its centre frequency and the integration window.

Metabolite	Center Frequency (ppm)	Integration range (δ) (±ppm)
Water	4.65	0.2
Carnosine	8	0.3
Creatine	3.85	0.2
TMA	3.2	0.1
IMCL	1.2	0.1
EMCL	1.48	0.2

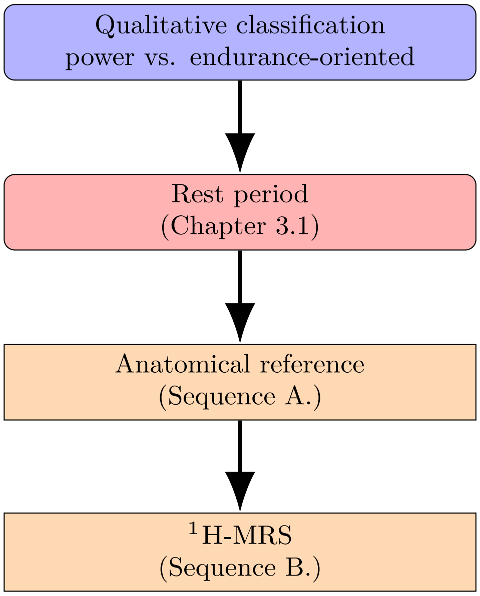

Figure 5.1: Flowchart of the data acquisition protocol for the skeletal muscle fiber composition study. Estimated scanning time: 20min.

5.4 Results

A total of eight ^{1}H-MRS spectra were collected with an average water linewidth quality of 14.5 ± 1.7Hz, meaning that data had a good spectral resolution. The maximum acceptable water linewidth is ∼25Hz for skeletal muscle on a 3T scanner [15, 20]. Because the quantification procedure involves using water as the point of reference (the denominator in Eqn. 5.1), a t-test was performed to ensure the water peak integral was comparable between FT and ST fiber groups, showing no statistical difference ($p = 0.25$) between them. The metabolite window selection, detrending and absolute integration followed by ratio quantification against water were performed as seen in Fig. 5.2.

Statistical t-tests comparing the mean ratio of each metabolite between FT and ST subjects showed statistically significant differences for carnosine, creatine, and TMA ($p < 0.05$). On the other hand, IMCL ($p = 0.70$) and EMCL ($p = 0.68$) showed no statistical difference between both groups (Fig. 5.3). The mean and standard deviation of the analyzed metabolites-to-water ratio are shown in Table 5.3, along with the peak integral from the water peak used as reference.

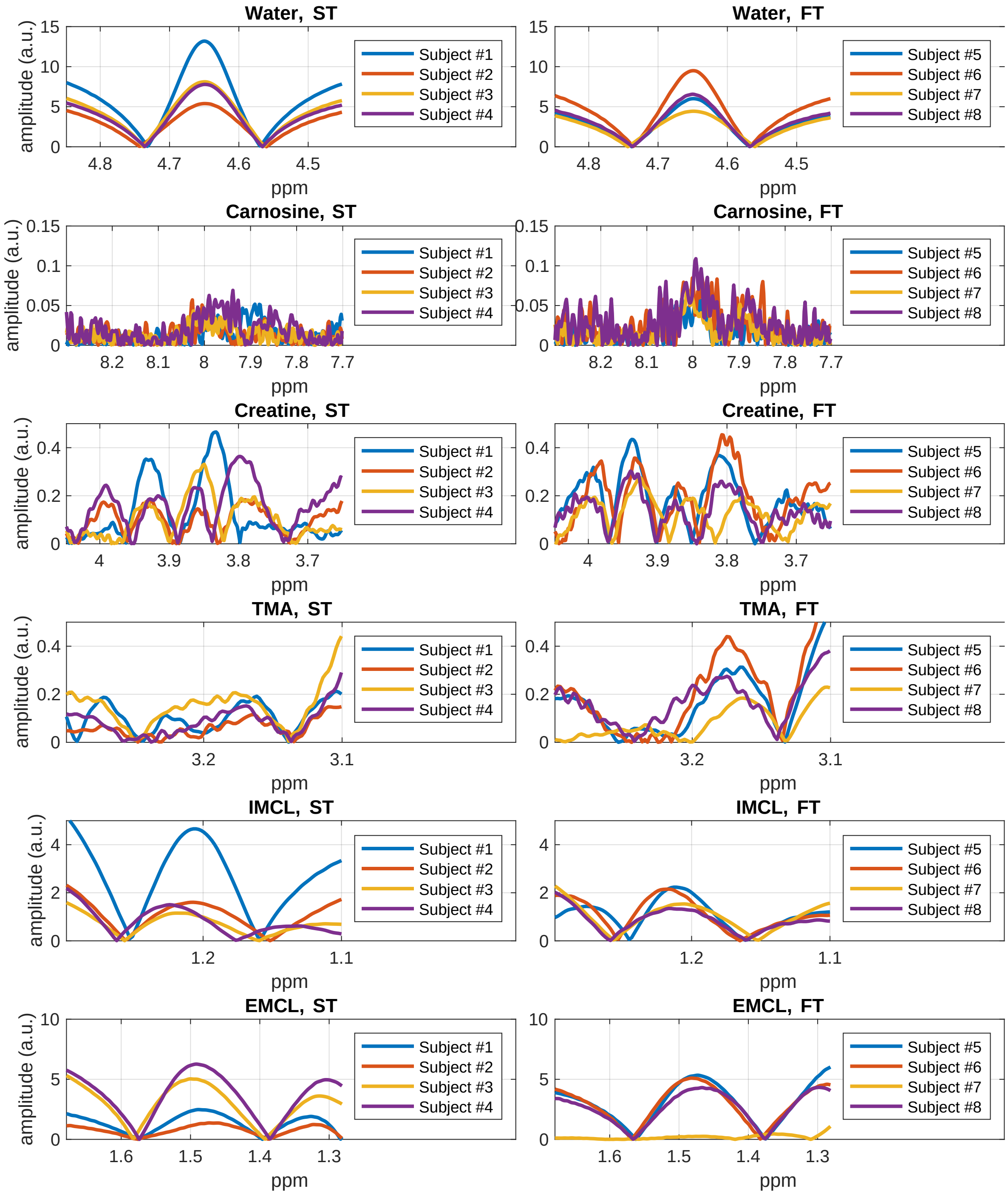

Figure 5.2: Amplification of the ^{1}H-MRS spectra for each metabolite centre frequency and window after the detrending and absolute integration procedure, for slow-twitch (left column) and fast-twitch (right column) subjects.

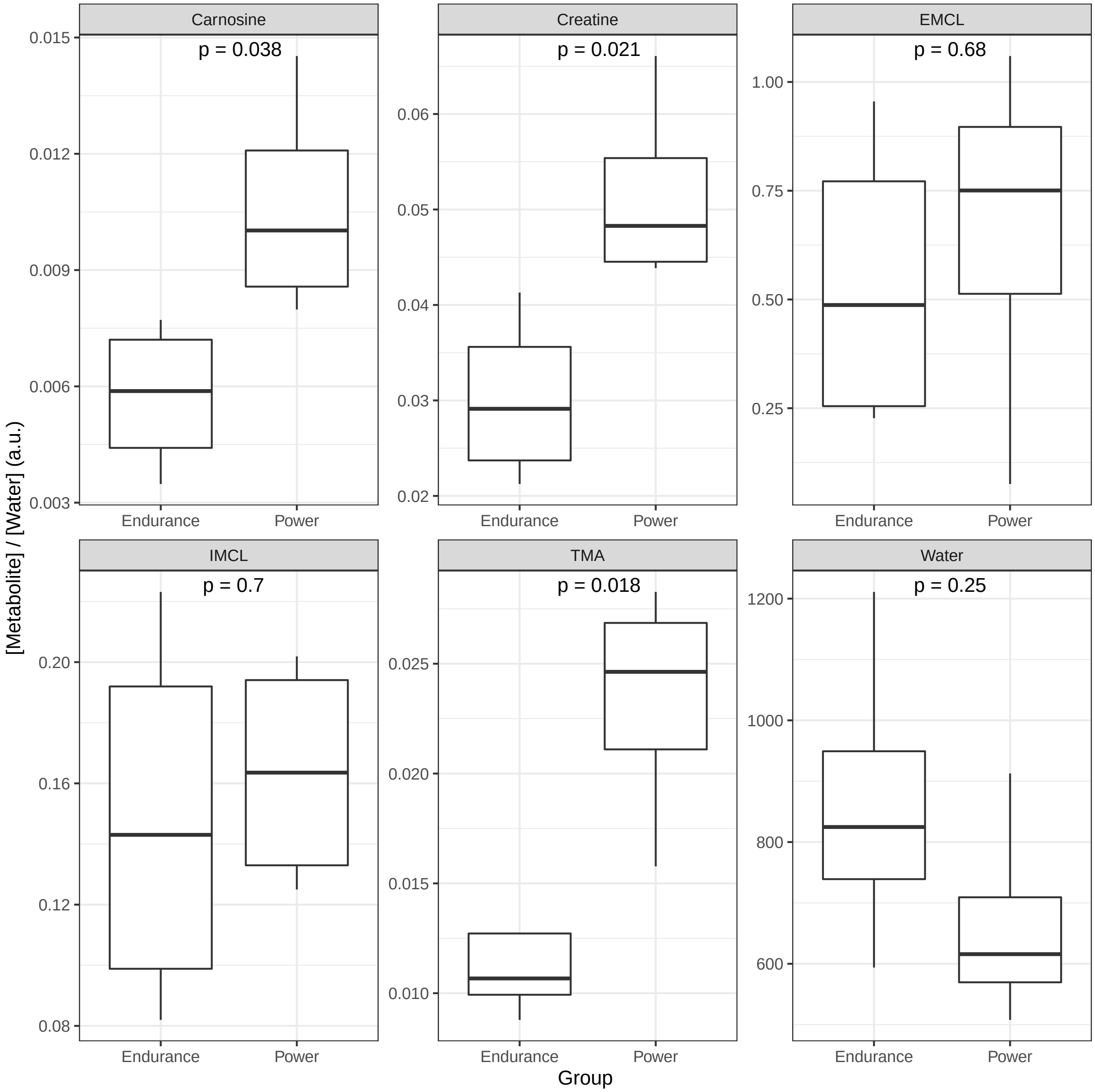

Figure 5.3: Statistical t-tests comparing the mean ratio of each metabolite between FT and ST subjects showed statistically significant differences for carnosine, creatine, and TMA ($p < 0.05$). On the other hand, IMCL ($p = 0.70$) and EMCL ($p = 0.68$) showed no statistical difference between both groups

Table 5.3: Metabolite ratio and water peak integration ^{1}mean (standard deviation). Ratio units: a.u.

Metabolite	**FT**^{1}	**ST**^{1}
Water	663.028 (175.314)	863.556 (257.743)
Carnosine	0.011 (0.003)	0.006 (0.002)
Creatine	0.052 (0.010)	0.030 (0.009)
TMA	0.023 (0.006)	0.012 (0.004)
IMCL	0.163 (0.039)	0.148 (0.066)
EMCL	0.659 (0.422)	0.539 (0.354)

5.5 Discussion

Water content in skeletal muscle under rest conditions has been shown to be constant (∼55 mmol [15]), a fact supported by the t-test of the water integral that showed no statistical difference between ST vs. FT, which suggested that the computed metabolite ratios were not biased due to the water integral (Eqn. 5.1).

A total of five ^{1}H-MRS metabolites were included in the analyses (Tbl. 5.2), the statistically significant differences of the carnosine ratio between ST and FT agrees with the literature, while the other two metabolites (creatine and TMA) showed a similar trend. It is hypothesized that the concentration differences are associated with the metabolic role of each of these metabolites; creatine is used as a source of energy during high-intensity exercise, more common in type II fibers; carnosine concentrations play a role in the buffering of H^+ arising from anaerobic metabolism in type II fibers [23, 24]; and the TMA complex, which contains choline, a metabolite that contributes to the anabolic effects on skeletal muscle [25]. On the other hand, IMCL and EMCL, metabolites that have been reported to vary with diet and type and duration of exercise, showed no statistical differences between both groups.

It was determined that carnosine, creatine and TMA values (compared to total peak water) obtained with ^{1}H-MRS could be used as discriminators between endurance and power athletes. Of note, EMCL and IMCL are inhomogeneously distributed within muscle and, as expected, showed high variability and lack of statistical significance between subjects. It is concluded that ^{1}H-MRS could be adopted as a non-invasive, fast ($\sim$8 min scan), and reliable technique to assess the predominant skeletal muscle fiber type. Further research is needed to compare this approach against muscle biopsy is necessary for validation. Provided that the presented method is proven effective, invasive biopsies for identifying muscle characteristics, diagnosing, and grading diseased muscle may become unnecessary.

5.6 Limitations

The following points are considered to be limitations of the current research:

- TA was the muscle studied for this research, due to the orientation of its fibers (*i.e.* it is a fusiform muscle), which decreased the quantification challenges introduced from BMS and dipolar coupling (Tbl. 2.5). Nevertheless, each muscle group shows a different distribution of muscle fibers, for instance, TA is predominantly fast-twitch (*i.e.* fiber type II) (Tbl. 2.5). If this study was performed in other muscle groups, a different pattern might be seen because the metabolic, contractile and endurance characteristics differ between muscle groups. Therefore, for future work, it would be ideal to analyze other muscle groups to characterize the biochemical environment of dominantly slow-twitch muscle groups.

References

1. Zierath, J. R. & Hawley, J. A. Skeletal Muscle Fiber Type: Influence on Contractile and Metabolic Properties. *PLOS Biol.* **2,** e348. doi:10.1371/journal.pbio.0020348 (Oct. 12, 2004).
2. Wilson, J. M. *et al.* The Effects of Endurance, Strength, and Power Training on Muscle Fiber Type Shifting. *The J. Strength & Cond. Res.* **26,** 1724–1729. doi:10.1519/JSC.0b013e318234eb6f (June 2012).
3. Chromiak, J. A. & Antonio, J. in *Essentials of Sports Nutrition and Supplements* (eds Antonio, J. *et al.*) 21–52 (Humana Press, Totowa, NJ, 2008). doi:10.1007/978-1-59745-302-8_2.
4. Lieber, R. L. *Skeletal muscle structure, function, and plasticity* (Lippincott Williams & Wilkins, 2002).
5. Baguet, A. *et al.* A New Method for Non-Invasive Estimation of Human Muscle Fiber Type Composition. *PLoS ONE* **6,** e21956. doi:10/fvmm6p (July 7, 2011).
6. Gollnick, P. D. & Matoba, H. The muscle fiber composition of skeletal muscle as a predictor of athletic success: An overview. *The Am. J. Sports Med.* **12,** 212–217. doi:10.1177/036354658401200309 (May 1, 1984).
7. Talbot, J. & Maves, L. Skeletal muscle fiber type: using insights from muscle developmental biology to dissect targets for susceptibility and resistance to muscle disease. *WIREs Dev. Biol.* **5,** 518–534. doi:10.1002/wdev.230 (July 1, 2016).
8. Schiaffino, S. Fibre types in skeletal muscle: a personal account. *Acta Physiol.* **199,** 451–463. doi:10.1111/j.1748-1716.2010.02130.x (2010).
9. Purves-Smith, F. M., Sgarioto, N. & Hepple, R. T. Fiber Typing in Aging Muscle. *Exerc. Sport Sci. Rev.* **42,** 45–52. doi:10.1249/JES.0000000000000012 (Apr. 2014).
10. Webster, C. *et al.* Fast muscle fibers are preferentially affected in Duchenne muscular dystrophy. *Cell* **52,** 503–513. doi:10.1016/0092-8674(88)90463-1 (Feb. 26, 1988).
11. Frankenberg, N. T. *et al.* Skeletal muscle cell-specific differences in type 2 diabetes. *Cell. Mol. Life Sci.* **79,** 256. doi:10.1007/s00018-022-04265-7 (Apr. 23, 2022).
12. Sattin, W., Mareci, T. H. & Scott, K. N. Exploiting the stimulated echo in nuclear magnetic resonance imaging. I. Method. *J. Magn. Reson. (1969)* **64,** 177–182. doi:10.1016/0022-2364(85)90049-6 (Aug. 1, 1985).
13. Karp, J. R. Muscle Fiber Types and Training. *Strength & Cond. J.* **23,** 21. doi:10.1519/00126548-200110000-00004 (Oct. 2001).
14. Ekblom, B. The muscle biopsy technique. Historical and methodological considerations. *Scand. J. Med. & Sci. Sports* **27,** 458–461. doi:10.1111/sms.12808 (2017).
15. Lievens, E. *et al.* CORP: quantification of human skeletal muscle carnosine concentration by proton magnetic resonance spectroscopy. *J. Appl. Physiol.* **131,** 250–264. doi:10/gqcfz6 (2021).
16. Da Eira Silva, V. *et al.* Magnetic Resonance Spectroscopy as a Non-invasive Method to Quantify Muscle Carnosine in Humans: a Comprehensive Validity Assessment. *Sci. Reports* **10,** 4908. doi:10.1038/s41598-020-61587-x (Mar. 17, 2020).
17. Scott, W., Stevens, J. & Binder–Macleod, S. A. Human Skeletal Muscle Fiber Type Classifications. *Phys. Ther.* **81,** 1810–1816. doi:10.1093/ptj/81.11.1810 (Nov. 1, 2001).
18. Degens, H. *et al.* Physiological comparison between non-athletes, endurance, power and team athletes. *Eur. J. Appl. Physiol.* **119,** 1377–1386. doi:10.1007/s00421-019-04128-3 (June 1, 2019).
19. Near, J. *et al.* Preprocessing, analysis and quantification in single-voxel magnetic resonance spectroscopy: experts' consensus recommendations. *NMR Biomed.* **34,** e4257. doi:10/ghz45z (2021).
20. Krššák, M. *et al.* Proton magnetic resonance spectroscopy in skeletal muscle: Experts' consensus recommendations. *NMR Biomed.* **34,** e4266. doi:10/gg4qn4 (2021).
21. Provencher, S. *LCModel's home page* http://www.lcmodel.com/lcmodel.shtml (2023).
22. Behar, K. L. & Ogino, T. Characterization of macromolecule resonances in the 1H NMR spectrum of rat brain. *Magn. Reson. Med.* **30,** 38–44. doi:10.1002/mrm.1910300107 (1993).
23. C. Harris, R., Dunnett, M. & Greenhaff, P. L. Carnosine and taurine contents in individual fibres of human vastus lateralis muscle. *J. Sports Sci.* **16,** 639–643. doi:10.1080/026404198366443 (1998).
24. Hill, C. A. *et al.* Influence of -alanine supplementation on skeletal muscle carnosine concentrations and high intensity cycling capacity. *Amino Acids* **32,** 225–233. doi:10.1007/s00726-006-0364-4 (2007).
25. Moretti, A. *et al.* Choline: An Essential Nutrient for Skeletal Muscle. *Nutrients* **12,** 2144. doi:10.3390/nu12072144 (July 18, 2020).

An investigation of electrical stimulation exercise and its effects on metabolic changes by means of proton spectroscopy in healthy skeletal muscle

6.1 Background

There has been a growing need for studying skeletal muscle metabolism *in vivo* in recent years [1], intending to understand its biochemical environment properties and dynamics during ordinary activity. Musculoskeletal disorders have been shown to affect or damage particular muscle functions, resulting in an abnormal state or behaviour, often followed by some physical disability [2, 3]. The ability to establish and compare healthy vs. disordered muscle would be beneficial to understand, diagnose, follow-up, and treat musculoskeletal diseases [1, 4], which ultimately increases the necessity of understanding the metabolism of healthy skeletal muscle *in vivo*.

One of the principal methods to differentiate between healthy vs. diseased muscle is by looking at its biochemical environment. For instance, inflammatory myopathies have shown metabolic alterations pointing to potential oxidative metabolism difficulties [5]. Comparing the metabolic profile during physical activity would amplify the potential differences between healthy vs. diseased muscle [6, 7]. Nevertheless, to assess these differences, it is required to characterize the biochemical environment of healthy skeletal muscle under the same conditions, *i.e.* during exercise.

MRS (described in Chapter 2.2.1) is well-suited for studying the biochemical environment of skeletal muscle. ^{1}H-MRS has been used as a tool to assess the dynamics of the biochemical environment in skeletal muscle *in vivo*. For example, several authors have investigated the metabolic changes before, during and after voluntary exercise in healthy skeletal muscle, where the effects of exercise have been reported through proton (Tbl. 6.1) or both proton and phosphorous spectroscopy (Tbl. 6.2). Nevertheless, mixed results are found across studies, for example, the increase or no change in [IMCL], the decrease or increase in [TMA] or the decrease or no change in [Cr] before vs. after exercise. These differences can be attributed to the variability of all these studies regarding the studied muscle (TA, GM, GL muscle groups), the training status of the subjects (non-trained, semi-trained or trained), diet or exercise restrictions prior to the scan, the exercise protocol and the presence of ischemic exercise.

On the other hand, ^{31}P-MRS is a well-established technique that has shown consistent results in the dynamics of metabolism in skeletal muscle under exercise: [PCr], and pH decreases, [P_i] increases, and [ATP] maintains its levels during exercise [8–11]. During the recovery period, metabolites return to baseline levels at different time constants (τ), for example, under aerobic conditions, τ_{PCr} recovers as a mono-exponential function.

As mentioned early, the exercise protocols differ significantly between studies (Tbl. 6.1 and 6.2). They differed from a short and easy plantar flexion to a long three-hour bout of cycling, which the participants may or may not have correctly executed. The significant variability in the exercise protocol hinders the development of a standard test to study the metabolism of active muscle. Even more, one of the main limitations of voluntary exercise is the lack of quantification of the 'amount' of exercise performed. An alternative could be electrical stimulation, which compared to voluntary exercise, provides a repeatable and quantifiable exercise routine [12]. Furthermore, Electrical Muscle Stimulation (EMS) has been proposed to reduce subjectivity induced by the exercise protocol [13]. As with voluntary exercise, ^{31}P-MRS has been used to study the metabolic behaviour of muscle during neuromuscular electrical stimulation [14, 15], and recently, to compare the effects of voluntary vs electrically evoked contractions (as shown in Table 6.3). These studies have shown that electrically induced exercise is more energy-demanding than voluntary exercise, attributed to the recruitment pattern differences highlighted in Table 2.4.

Altogether, the effects of voluntary and electrically induced exercise on skeletal muscle metabolism are well documented with ^{31}P-MRS. However, using ^{31}P-MRS requires additional hardware (such as amplifiers and RF coils), software [16], and it shows an inferior SNR compared to ^{1}H. Altogether, these factors hamper the adoption of ^{31}P-MRS in every MRI system. On the other hand, ^{1}H-MRS is available 'out of the box' in most MRI systems. ^{1}H-MRS has been used to study voluntary exercise, with only one study using electrically induced exercise to investigate deoxymyoglobin dynamics [17]. Thus, this research aimed to study the metabolic profile of the lower leg muscles during an EMS protocol through ^{1}H-MRS. It is hypothesized that with the use of a more standardized exercise protocol and the use of ^{1}H-MRS, skeletal muscle metabolism investigation could be adopted by more research centres.

Table 6.1: Studies focused on the effects of voluntary exercise employing ^{1}H-MRS in skeletal muscle.

Ref	**Muscle**	**Metabolites**	**Exercise characteristics**	**Results (pre vs post)**	**Notes**
[18]	Calf - TA	Lac	8min plantar flexion Free MVC 10min recovery	↑ [Lac] during exercise ↓ [Lac] during recovery	Ischemic exercise @ 240 Torr DQF MRS method PRESS
[19]	Thigh - VL, VI Calf- TA	AcCtn, Ctn	4min plantar flexion until fatigue 0.2-2h with an ergometer 6h alpine ski tour 60-90% VO_{2max}	↑ [AcCtn]	↑ variability in [AcCtn] ↑ as reference PRESS
[20]	Thigh - VL Biceps	IMCL, EMCL	3h cycling 55% maximal energy 5min recovery	↓ [IMCL] in VL ↓ [IMCL] in biceps No changes [EMCL]	Trained population Standardized diet PRESS H_2O as reference
[21]	Thigh Calf	IMCL, Cr, TMA	3h with an ergometer 50% maximal speed 3h on a treadmill 40% maximal speed	↓ [IMCL] ↓ [TMA] No changes [Cr]	Trained population [IMCL] varied across subjects pre-exercise H_2O as reference PRESS
[22]	Calf - SOL	AcCtn	20min rest 2min pre-exercise 5min calf-raise	↑ [AcCtn] ↑ [Ctn]	At 7T MRI STEAM Cr @3.02ppm as reference Exercise outside MRI

Table 6.2: Studies focused on the effects of exercise by means of $^{1}H/^{31}P$-MRS in skeletal muscle. To note the interesting observation of a global chemical shift of 0.1ppm after exercise [23].

Ref	**Muscle**	**Metabolites**	**Exercise characteristics**	**Results (pre vs post)**	**Notes**
[23]	Calf - TA	Cr, TMA, PCr	1-5min plantar flexion until fatigue	↓ [Cr], [TMA] No changes in [IMCL] Correlation between ↓ of [Cr] and [PCr]	Ischemic exercise Semi-trained population 0.1ppm shift PRESS H_2O as reference
[24]	Calf - GL	Lac, PCr, P_i, ATP	2min rest 2.5min plantar flexion 50% MVC 4min recovery	↓ [PCr], pH, [Cr] ↑ [P_i] ↑ [Lac] during exercise ↓ [Lac] postexercise No changes in [TMA], [IMCL], [EMCL]	Ischemic exercise @ 230 Torr for 9min Interleaved proton/phosphorous MRS Exercise during periods without MRS STEAM External phantom reference
[25]	Calf - GM	Car, PCr, P_i, ATP	2min rest 6min plantar flexion 30% MVC 6min recovery	↓ PCr-to-ATP flux ↑ Pi-to-ATP flux ↑ [PME]	At 7T MR Elderly vs young cohorts H_2O as reference

Table 6.3: Studies focused on the differences between voluntary vs electrically induced contractions in skeletal muscle.

Reference	**Muscle**	**MRS Nuclei**	**Exercise characteristics**	**Results (VC vs EMS)**	**Notes**
[13]	Calf - GM, SOL	^{31}P	Continuous plantar flexion @40% MVC Repeated plantar flexion @75% MVC	↓ [PCr] ↓ pH (in EMS)	Motor point stimulation VC has lower ATP demand than EMS EMS: pulse width = 0.2ms, frequency = 10Hz
[14]	Thigh - VM	^{31}P	64 contractions @20% MVC 5.5s on/off	↓ P_i/PCr ratio ↓ pH	Motor point stimulation Maximum effects @5min of EMS EMS: pulse width = 0.25ms, frequency = 50Hz
[17]	Thigh - VM	^{31}P ^{1}H	64 contractions @10% MVC 6s on/off	↓ P_i/PCr ratio ↓ pH ↓ myoglobin desaturation	Motor point stimulation Tried ischemic protocol EMS: pulse width = 0.25ms, frequency = 50Hz

6.2 Methods

Four healthy male volunteers (age = 27±3yrs, height = 177±4cm, weight = 73±13kg) were recruited. Experiments were performed accordingly to the MRI general methods (Chapter 3.1). The protocol consisted of acquiring a pre-exercise ^{1}H-MRS (described in Sequence B.), afterwards, volunteers received the electrical stimulation protocol while lying in the MRI magnet bed without removing the T/R coil, the Velcro strap or padding. Finally, one more post-stimulation ^{1}H-MRS acquisition was taken (Fig. 6.1).

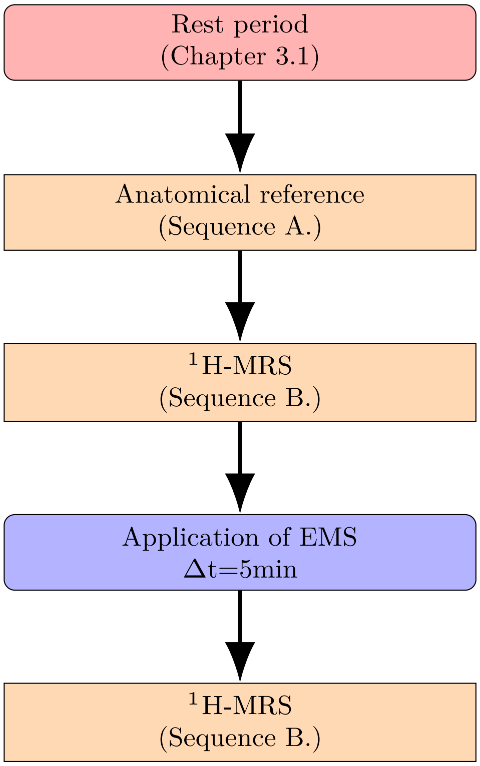

Figure 6.1: Flowchart of the data acquisition protocol. The application of EMS was performed on the MRI magnet bed without moving the volunteer, which will help maintain the landmarks and the VOI position for the ^{1}H-MRS scan. Estimated scanning time: 30min.

A Digitimer constant current stimulator (model DS7A, Garden City, UK) was used as shown in Fig. 6.2(a,b). This stimulator system does not have built-in capabilities to set up a stimulation protocol, but it can be programmed via TTL compatible trigger. Therefore, the stimulation protocol was managed using a microcontroller board based on the ATmega328P (Arduino Uno) with a program written in a subset of C/C++, loaded to the microcontroller via an external computer (Fig. 6.2(c)). Electrical stimulation was applied for 5min, with a pulse width of 200µs, frequency = 30Hz, with an ON/OFF cycle of 1s, and current adjusted for patient comfort. There is no consensus about the EMS parameters, so the parameters were carefully chosen following recommendations for EMS optimization [26–28], while maximizing the comfort of the participants. The appropriate position of the electrodes was found by exploring the skin surface in the popliteal fossa region with a stimulation pen electrode, aiming to locate the common peroneal nerve [12, 29]. Electrodes were placed and secured using Micropore paper tape from the beginning of the scanning to avoid moving artifacts (Fig. 6.2(c,d,e)). For safety reasons, the stimulation system and the external computer were placed inside the MRI magnet room but outside of the 5 Gauss line. After the pre-stimulation ^{1}H-MRS was acquired, the MRI magnet bed was pulled out of the bore, the stimulation system was connected via BNC cables with alligator ends to the electrodes, and the EMS protocol was applied. Once stimulation was finished, the BNC alligator cables were removed. The participant was introduced back into the MRI bore to keep the same landmarks and VOI position for the ^{1}H-MRS.

^{1}H-MRS data were analyzed and quantified as described in Sequence B., followed by a repeated measurements 3-way ANOVA test, assessing the differences in the mean metabolite ratio between metabolites, pre vs. post electrical stimulation, and subjects.

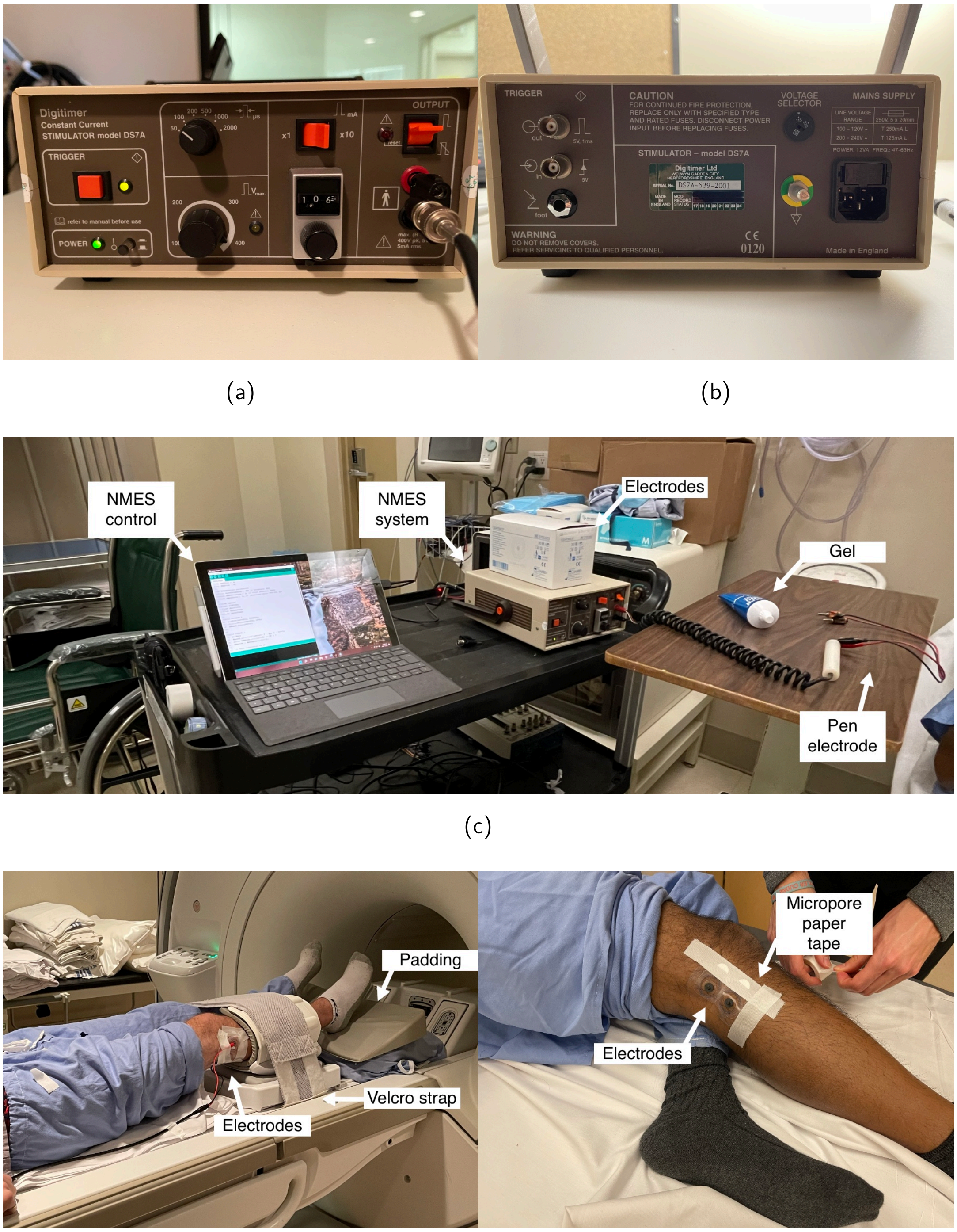

(a) (b)

(c)

(d) (e)

Figure 6.2: EMS experimental setup. (a,b) shows the Digitimer constant current stimulator (model DS7A, Garden City, UK). In (b), the TTL input trigger is seen, which was used to control the EMS protocol. (c) the overall experiment setup includes the computer used to load the stimulation protocol, the EMS system, the MRI-compatible carbon electrodes, and the gel and pen electrodes. (d,e) shows the participant setup. (d) shows the use of Velcro straps and padding to reduce movement and increase patient comfort. (e) shows the electrode placement for the EMS protocol.

6.3 Results

A total of 8 ^{1}H-MRS spectra were collected from four volunteers. The average FWHM for the unsuppressed water peak was 14 ± 0.2Hz across all spectra. A box plot of the 12 metabolites included in the analysis is shown in Fig. 6.3. The EMS protocol was successfully controlled using a microcontroller board based on the ATmega328P, allowing to customize of the frequency, duration and duty cycle of the EMS protocol to the experimental needs.

Repeated measurements 3-way ANOVA was performed with metabolite, pre vs. post electrical stimulation and subjects as factors (Fig. 6.4). Results showed no significant difference in the mean ratio of metabolites between pre vs. post-electrical stimulation ($p = 0.988$). In opposition, the mean metabolite ratio between metabolites and subjects were statistically different ($p < 0.001$). Further, multiple comparisons between pre vs. post-electrical stimulation for each metabolite showed no statistical difference for all metabolite peaks (Fig. 6.5), with the estimated marginal means for each metabolite for both experimental conditions shown in Table 6.4.

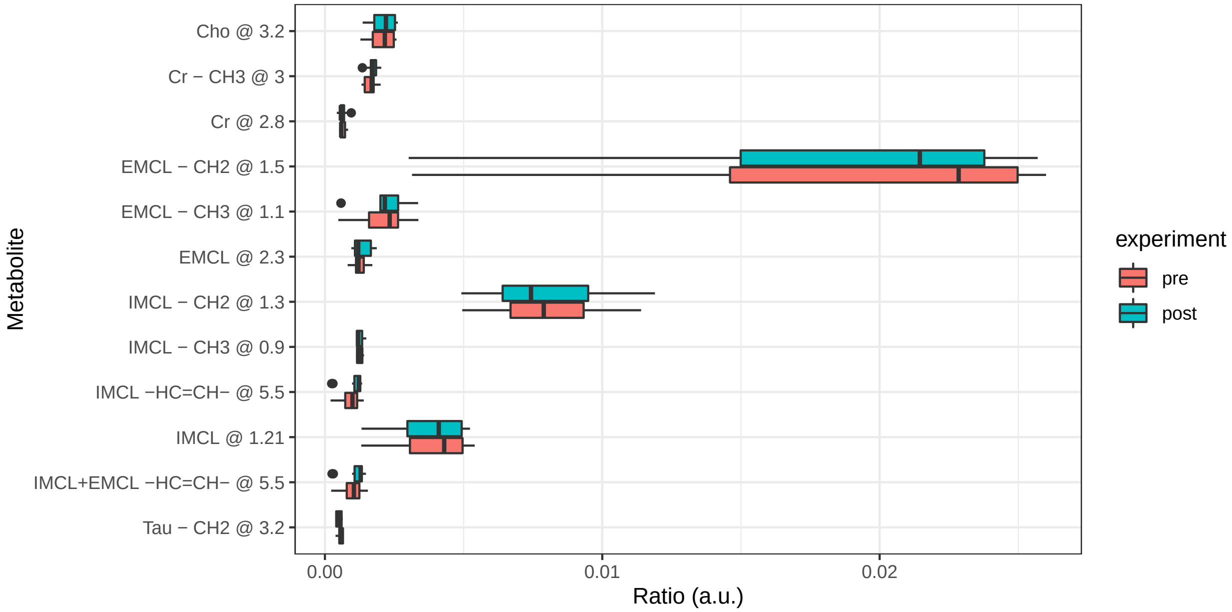

Figure 6.3: Exploratory boxplot for each metabolite ratio across subjects by experiment (pre vs. post-EMS). Similar to Chapter 4, the metabolites that showed high variability were both IMCL and EMCL. On the other hand, Tau, Cr and Cho showed low variability. The mean ratio between experiments (pre vs. post-EMS) for each metabolite showed no differences.

```
## Type III Analysis of Variance Table
##                          Sum Sq    Mean Sq DF F value    Pr(>F)
## metabolite            0.0065011 0.00059101 11 81.1727 < 2.2e-16 ***
## experiment            0.0000000 0.00000000  1  0.0002    0.9878
## subject               0.0003043 0.00010143  3 13.9307 2.055e-08 ***
## ---
## Signif. codes:  0 '***' 0.001 '**' 0.01 '*' 0.05 '.' 0.1 ' ' 1
```

Figure 6.4: Repeated measurements 3-way ANOVA results. The model included the metabolites, pre vs. post-electrical stimulation, and subjects as factors. Results show no statistical difference in the mean metabolite ratio between pre vs. post-electrical stimulation (p = 0.988). On the contrary, the mean metabolite ratio was significant between metabolites and subjects (p < 0.001).

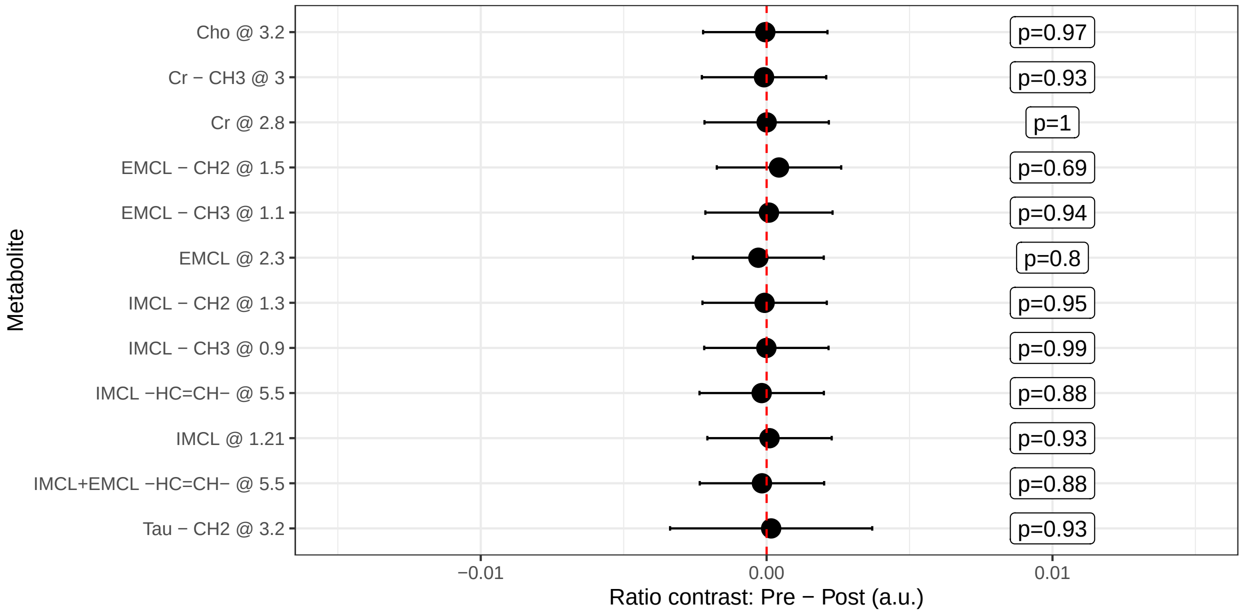

Figure 6.5: Post hoc contrasts analysis of the mean metabolite ratio between experiments (pre vs. post-EMS). Confirming that none of the metabolites analyzed showed a statistically significant change in the mean metabolite ratio pre vs. post-EMS.

Table 6.4: Estimated mean and standard error of the metabolite ratio between pre vs post-electrical stimulation.

Metabolite	Pre-exercise	Post-exercise
Cho @ 3.2	0.00204 ± 8e-04	0.00209 ± 8e-04
Cr - CH3 @ 3	0.00164 ± 8e-04	0.00173 ± 8e-04
Cr @ 2.8	0.00065 ± 8e-04	0.00064 ± 8e-04
EMCL - CH2 @ 1.5	0.01816 ± 8e-04	0.01773 ± 8e-04
EMCL - CH3 @ 1.1	0.00207 ± 8e-04	0.00198 ± 8e-04
EMCL @ 2.3	0.00122 ± 8e-04	0.00151 ± 9e-04
IMCL - CH2 @ 1.3	0.00802 ± 8e-04	0.00809 ± 8e-04
IMCL - CH3 @ 0.9	0.00125 ± 8e-04	0.00126 ± 8e-04
IMCL -HC=CH- @ 5.5	0.00089 ± 8e-04	0.00106 ± 8e-04
IMCL @ 1.21	0.00379 ± 8e-04	0.00369 ± 8e-04
IMCL+EMCL -HC=CH- @ 5.5	0.00095 ± 8e-04	0.00111 ± 8e-04
Tau - CH2 @ 3.2	0.00019 ± 0.0014	3e-05 ± 0.0011

6.4 Discussion

Similar to Chapter 4, the statistical difference between metabolites and subjects was expected since each metabolite shows a different concentration in skeletal muscle and across subjects, depending on diet and exercise, respectively. Since the MRI system showed good shim across ^{1}H-MRS acquisitions, the FWHM was not included as a covariate in the model.

From the analyzed metabolites, lipids (IMCL) is the only metabolite that has shown changes in endurance exercise using ^{1}H-MRS [21]. Tau and Cho are involved in muscle metabolism, contributing to the anabolic effects on skeletal muscle [30]. Cr is a source of energy during high-intensity exercise, but it is thought that ^{1}H-MRS shows the total Cr concentration *i.e.* Cr + PCr, thus no changes were expected pre vs. post-EMS.

Overall, ^{1}H-MRS have shown no significant differences in the metabolic profile of skeletal muscle from the lower leg following electrical muscle stimulation. This suggests that ^{1}H-MRS is less sensitive than other MRS nuclei (such as ^{31}P) to study the effects of electrical stimulation on skeletal muscle. It was believed that using EMS and its advantages against voluntary exercises, such as its high metabolic demand (Tbl. 2.4), would cause observable changes in the metabolic profile that would be relevant to characterize healthy skeletal muscle.

6.4.1 Limitations

The following points are considered to be limitations of the current study:

- None of the participants reported pain or discomfort during the localization of the common peroneal nerve or the EMS exercise application. However, they did report an ‘unusual’ feeling related to their inability to control their exercise contractions. Although participants decided to continue the experiments, this sensation could have introduced some stress on the volunteers that might have affected the ^{1}H-MRS scans.
- EMS offers the advantage of a higher reproducibility in the exercise routine. In this experiment, the EMS current was not adjusted to a target MVC to standardize the relative effort of each participant. The reason is related to the bullet point above, where increasing the current only augmented the unusual feeling. It is recognized that the need for relative effort standardization is a drawback.
- The duration and the relative effort of the EMS exercise applied in this study could not have been enough to reflect changes in the biochemical environment (compared to other studies (Tbl. 6.1, 6.2 and 6.3)).
- Overall, in the future, it would be ideal to use a relatively high MVC and standardize it across subjects. A possibility to achieve this would be to include a pre-training session to reduce the participant’s stress/discomfort.

6.5 Appendix

6.5.1 Code

The code used for programming the Digitimer constant current stimulator is shown below. The sequence of steps to apply the stimulation is as follows:

1. The user inputs the frequency (`nmesFrequency`), duration (`nmesDuration`), and duty cycle (`nmesCycle`)
2. Code is loaded to the ATmega328P, and the stimulation parameters are fed to the input/output variables of the system
3. The ATmega328P waits until a button is pressed to start the electrical stimulation

```
int nmesPin = 4;
int dButton = 0;

// Stimulation parameters
float nmesFrequency = 30; // frequency (Hz)
float nmesDuration = 5; // total duration (min)
float nmesCycle = 1; //  stim-rest cycle 50%-50% (s)

float cycle;
float endTime;
float duration;
float frequency;
float cycleTime;

void setup() {
  pinMode(nmesPin, OUTPUT);
```

```
  digitalWrite(nmesPin, LOW);
  Serial.begin(9600);
}

void loop() {
  // Menu
  Serial.println("\nStart? 0 - No, 1 - Yes");
  while (Serial.available() == 0) { }
  dButton = Serial.parseInt();

  // Unit conversion to ms
  frequency = 1000 / (nmesFrequency * 2.0);
  duration = nmesDuration * 60.0 * 1000;
  cycle = nmesCycle * 1000 / 2.0;

  // Start
  if (dButton == 1) {
    Serial.print("Stimulation running!");
    endTime =  millis() + duration;
    // Total stimulation loop
    while (endTime-millis() > 0.0){
      cycleTime = millis() + cycle;
      // Cycle stimulation loop
      while (cycleTime-millis() > 0.0){
        digitalWrite(nmesPin, HIGH);
        delay(frequency);
        digitalWrite(nmesPin, LOW);
        delay(frequency);
```

```
      }
      delay(cycle);
    }
    Serial.print(”\nStimulation finished!”);
  }
  // No start
  if (dButton == 0) {
    Serial.print(”Waiting to start!”);
  }
}
```

References

1. Prompers, J. J. *et al.* Dynamic MRS and MRI of skeletal muscle function and biomechanics. *NMR Biomed.* **19,** 927–953. doi:`10.1002/nbm.1095` (2006).
2. Murphy, K. *et al. Health state descriptions for Canadians: musculoskeletal* (Statistics Canada, 2006).
3. Olsen, N. J., Qi, J. & Park, J. H. Imaging and skeletal muscle disease. *Curr. Rheumatol. Reports* **7,** 106–114. doi:`10.1007/s11926-005-0062-3` (Apr. 1, 2005).
4. Schiffenbauer, A. Imaging: seeing muscle in new ways. *Curr. Opin. Rheumatol.* **26,** 712. doi:`10.1097/BOR.0000000000000105` (Nov. 2014).
5. Kuo, G. P. & Carrino, J. A. Skeletal muscle imaging and inflammatory myopathies. *Curr. Opin. Rheumatol.* **19,** 530. doi:`10.1097/BOR.0b013e3282efdc66` (Nov. 2007).
6. Argov, Z. *et al.* Intracellular phosphates in inclusion body myositis—A 31P magnetic resonance spectroscopy study. *Muscle & Nerve* **21,** 1523–1525. doi:`10.1002/(SICI)1097-4598(199811)21:11<1523::AID-MUS22>3.0.CO;2-#` (1998).
7. Cea, G. *et al.* Reduced oxidative phosphorylation and proton efflux suggest reduced capillary blood supply in skeletal muscle of patients with dermatomyositis and polymyositis: a quantitative 31P-magnetic resonance spectroscopy and MRI study. *Brain* **125,** 1635–1645. doi:`10.1093/brain/awf163` (July 1, 2002).
8. Santos-Díaz, A. & Noseworthy, M. D. Phosphorus magnetic resonance spectroscopy and imaging (31P-MRS/MRSI) as a window to brain and muscle metabolism: A review of the methods. *Biomed. Signal Process. Control.* **60,** 101967. doi:`10.1016/j.bspc.2020.101967` (2020).
9. Boesch, C. Musculoskeletal spectroscopy. *J. Magn. Reson. Imaging* **25,** 321–338. doi:`10.1002/jmri.20806` (2007).
10. Bendahan, D. *et al.* Non-invasive investigation of muscle function using 31P magnetic resonance spectroscopy and 1H MR imaging. *Revue neurologique* **162,** 467–484. doi:`10.1016/s0035-3787(06)75038-x` (Apr. 1, 2006).
11. Valkovič, L., Chmelík, M. & Krššák, M. In-vivo 31P-MRS of skeletal muscle and liver: A way for non-invasive assessment of their metabolism. *Anal. Biochem. Introduction to in vivo Magnetic Resonance Spectroscopy (MRS): A method to non-invasively study metabolism* **529,** 193–215. doi:`10.1016/j.ab.2017.01.018` (July 15, 2017).
12. Lieber, R. L. *Skeletal muscle structure, function, and plasticity* (Lippincott Williams & Wilkins, 2002).
13. Ratkevičius, A. *et al.* Energy metabolism of the gastrocnemius and soleus muscles during isometric voluntary and electrically induced contractions in man. *The J. Physiol.* **507,** 593–602. doi:`10.1111/j.1469-7793.1998.593bt.x` (Pt 2 Mar. 1, 1998).
14. Vanderthommen, M. *et al.* Human Muscle Energetics During Voluntary and Electrically Induced Isometric Contractions as Measured by 31P NMR Spectroscopy. *Int. J. Sports Med.* **20,** 279–283. doi:`10.1055/s-2007-971131` (July 1999).
15. Akbari, A. *et al.* Safe MRI-Compatible electrical muscle stimulation (EMS) system: Concurrent MRI and Electrical Stimulation. *J. Magn. Reson. Imaging* **44,** 1530–1538. doi:`10.1002/jmri.25316` (Dec. 2016).
16. Meyerspeer, M. *et al.* 31P magnetic resonance spectroscopy in skeletal muscle: Experts' consensus recommendations. *NMR Biomed.* **34,** e4246. doi:`10.1002/nbm.4246` (2021).
17. Vanderthommen, M. *et al.* A comparison of voluntary and electrically induced contractions by interleaved 1H- and 31P-NMRS in humans. *J. Appl. Physiol.* **94,** 1012–1024. doi:`10.1152/japplphysiol.00887.2001` (Mar. 1, 2003).
18. Jouvensal, L., Carlier, P. G. & Bloch, G. Practical implementation of single-voxel double-quantum editing on a whole-body NMR spectrometer: Localized monitoring of lactate in the human leg during and after exercise. *Magn. Reson. Med.* **36,** 487–490. doi:`10.1002/mrm.1910360325` (1996).
19. Kreis, R. *et al.* Non-invasive observation of acetyl-group buffering by 1H-MR spectroscopy in exercising human muscle. *NMR Biomed.* **12,** 471–476. doi:`10.1002/(SICI)1099-1492(199911)12:7<471::AID-NBM591>3.0.CO;2-A` (1999).
20. Schrauwen-Hinderling, V. B. *et al.* Intramyocellular lipid content is increased after exercise in nonexercising human skeletal muscle. *J. Appl. Physiol.* **95,** 2328–2332. doi:`10.1152/japplphysiol.00304.2003` (Dec. 1, 2003).
21. Vermathen, P. *et al.* Skeletal muscle 1H MRSI before and after prolonged exercise. I. muscle specific depletion of intramyocellular lipids. *Magn. Reson. Med.* **68,** 1357–1367. doi:`10/fznjv8` (2012).
22. Ren, J. *et al.* Dynamic monitoring of carnitine and acetylcarnitine in the trimethylamine signal after exercise in human skeletal muscle by 7T 1H-MRS. *Magn. Reson. Med.* **69,** 7–17. doi:`10.1002/mrm.24249` (2013).
23. Kreis, R. *et al.* Effect of Exercise on the Creatine Resonances in 1H MR Spectra of Human Skeletal Muscle. *J. Magn. Reson.* **137,** 350–357. doi:`10.1006/jmre.1998.1683` (1999).

24. Meyerspeer, M. *et al.* Direct noninvasive quantification of lactate and high energy phosphates simultaneously in exercising human skeletal muscle by localized magnetic resonance spectroscopy. *Magn. Reson. Med.* **57,** 654–660. doi:`10.1002/mrm.21188` (2007).
25. Krumpolec, P. *et al.* Multinuclear MRS at 7T Uncovers Exercise Driven Differences in Skeletal Muscle Energy Metabolism Between Young and Seniors. *Front. Physiol.* **11,** 644. doi:`10.3389/fphys.2020.00644` (2020).
26. Lake, D. A. Neuromuscular Electrical Stimulation. *Sports Med.* **13,** 320–336. doi:`10.2165/00007256-199213050-00003` (May 1, 1992).
27. Vanderthommen, M. & Duchateau, J. Electrical Stimulation as a Modality to Improve Performance of the Neuromuscular System. *Exerc. Sport Sci. Rev.* **35,** 180–185. doi:`10.1097/jes.0b013e318156e785` (2007).
28. Maffiuletti, N. A. Physiological and methodological considerations for the use of neuromuscular electrical stimulation. *Eur. J. Appl. Physiol.* **110,** 223–234. doi:`10.1007/s00421-010-1502-y` (2010).
29. Botter, A. *et al.* Atlas of the muscle motor points for the lower limb: implications for electrical stimulation procedures and electrode positioning. *Eur. J. Appl. Physiol.* **111,** 2461. doi:`10.1007/s00421-011-2093-y` (2011).
30. Moretti, A. *et al.* Choline: An Essential Nutrient for Skeletal Muscle. *Nutrients* **12,** 2144. doi:`10.3390/nu12072144` (July 18, 2020).

Simultaneous Studies of Muscle Blood Oxygen Level Dependent Signal and Electromyography: a safety and quality assessment analysis

7.1 Introduction

Some experiments presented in this thesis required the simultaneous acquisitions of muscle BOLD dataset with an EMG recording. Simultaneous acquisitions of the brain (fMRI) or muscle (BOLD) with surface EMG is a non-invasive combination that provides functional and electrophysiological information on brain or muscle activation, combining the high spatial resolution of MRI with the temporal resolution of EMG [1] (Fig. 7.1). Analogous to a typical concurrent study of fMRI/EEG, simultaneous functional MRI/EMG acquisitions are able to strengthen brain studies by investigating the relationship between brain activity and the muscle motor areas of interest. Moreover, muscle BOLD/EMG can also benefit by studying the correlation between muscle electrical and physiologic activity.

Several brain fMRI studies have investigated the mechanisms and effects of stroke recovery [2], multiple sclerosis [3], and the effect of exercise-induced changes on the brain [4–6]. Nonetheless, there is an increasing need to record, characterize and correlate the motor task with brain fMRI or skeletal muscle BOLD response to better understand the regional variation in brain or muscle activation and its modulation [7, 8]. EMG can fill this gap, as it is an inexpensive, non-invasive and well-established technique used frequently in clinical research [9].

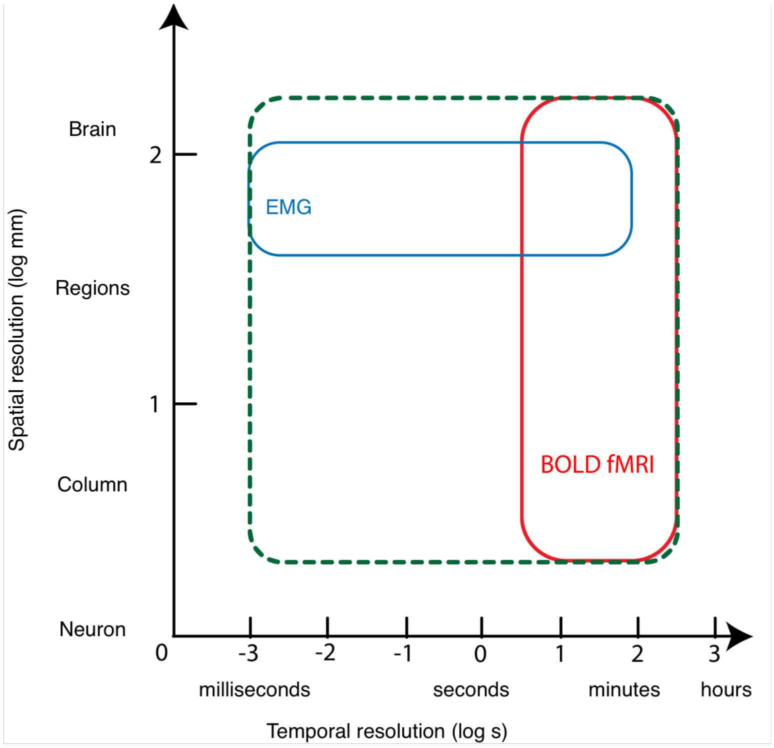

Figure 7.1: Ideal spatial and temporal resolution of both fMRI (in red) and EMG (in blue) techniques. Simultaneous studies of fMRI/EMG (green, dashed) would provide a wider perspective of the motor task being performed by connecting the high spatial resolution of fMRI and the high temporal resolution of EMG.

Similar to fMRI/EEG, the coupling of these two techniques is complex. Problems such as the gradient artifact (GA) and the use of additional hardware equipment (such as MRI-compatible surface electrodes, electrode leads, and amplifiers) can interfere with the characterization of muscle activation from the EMG and fMRI signal, respectively [10–12]. For example, while using the MRI, the GA arises from the MRI scanner rapidly switching gradients for spatial encoding, causing a severe interference pattern in the EMG recording. This pattern will mask the electrophysiological EMG signal, leaving the recording useless [13, 14] (artifact from MRI → EMG). In opposition, the EMG will affect the MRI acquisitions indirectly through the hardware introduced into the MRI environment required to acquire the EMG signal (artifact from EMG → MRI).

7.2 Safety assessment

7.2.1 Background

Simultaneous fMRI/EMG acquisitions inside the MRI require using compatible hardware, such as carbon electrodes, high-impedance electrode leads and amplifiers. The use of RF pulses during any MRI sequence can cause burns in the areas where atypical hardware is in contact with the volunteer, such as the electrodes on the skin, raising safety concerns. Previous case reports have raised concerns about this type of injury [15, 16]. Therefore, tests were conducted on the EMG hardware to ensure the safety of the volunteers during the experiments, mainly monitoring the temperature of the surface electrodes and the specific absorption rate (SAR) of the volunteer while scanning. SAR is a measurement of the amount of energy deposited by the RF pulses on the total mass of the volunteer [17, 18].

7.2.2 Methods

The test consisted of setting up the EMG as described in Chapter 3.2. Since the electrodes are MRI safe (*i.e.* MRI-compatible) and are routinely used during cardiac research studies at the IRC, little to no temperature changes were expected during scanning. The temperature was monitored using optical temperature probes fed into the MRI room and recorded on a PC system in the MRI control room. Each temperature probe was placed under its respective electrode. SAR measurements were recorded manually from the MRI control console concurrently.

The MRI sequences used in the test were a ^{1}H-MRS, an fMRI and a Fast Imaging Employing Steady-state Acquisition (FIESTA). The latter was chosen because it is one of the most intensive RF sequences available in the MRI system. The details and parameters of each sequence are:

A. ^{1}H-**MRS**: as described in Sequence B.

B. **BOLD**: as described in Sequence E.

C. **FIESTA**: 2D fast imaging employing steady state acquisition with 15 slices, 256 × 256 matrix, 5mm thickness, TE/TR/flip = 2/5.1ms/90°, RB = 125kHz.

To ensure volunteer safety, a 12cm diameter × 25cm long QA/QC cylindrical phantom with a dimethyl silicone fluid, gadolinium and colourant was used first (Fig. 7.2) before testing any subjects. After observing no significant change in both temperature and SAR, the same experiment was performed on a volunteer.

7.2.3 Results

SAR recordings over the entire duration of each sequence are shown in Fig. 7.4. For both cases, for the phantom and the volunteer, the SAR did not change significantly for the three sequences tested, as shown in Table 7.2. Temperature recordings of the three electrodes used for the EMG system (E1, E2 as the differential electrodes. Ref as the reference) of the phantom and volunteer for each of the three tested sequences (Fig. 7.3) with its respective means and standard deviations shown in Table 7.1. It was observed that the FIESTA sequence had the most significant change in SAR (phantom: 2.25±0.53 W/kg, volunteer: 0.77±0.16 W/kg) and temperature (phantom: ΔE1 = 0.9°C, ΔE2 = 0.5°C, ΔReference = 0.4°C; volunteer: ΔE1 = 1°C, ΔE2 = 0.3°C, ΔReference = 0.7°C) compared to the ^{1}H-MRS or fMRI sequence.

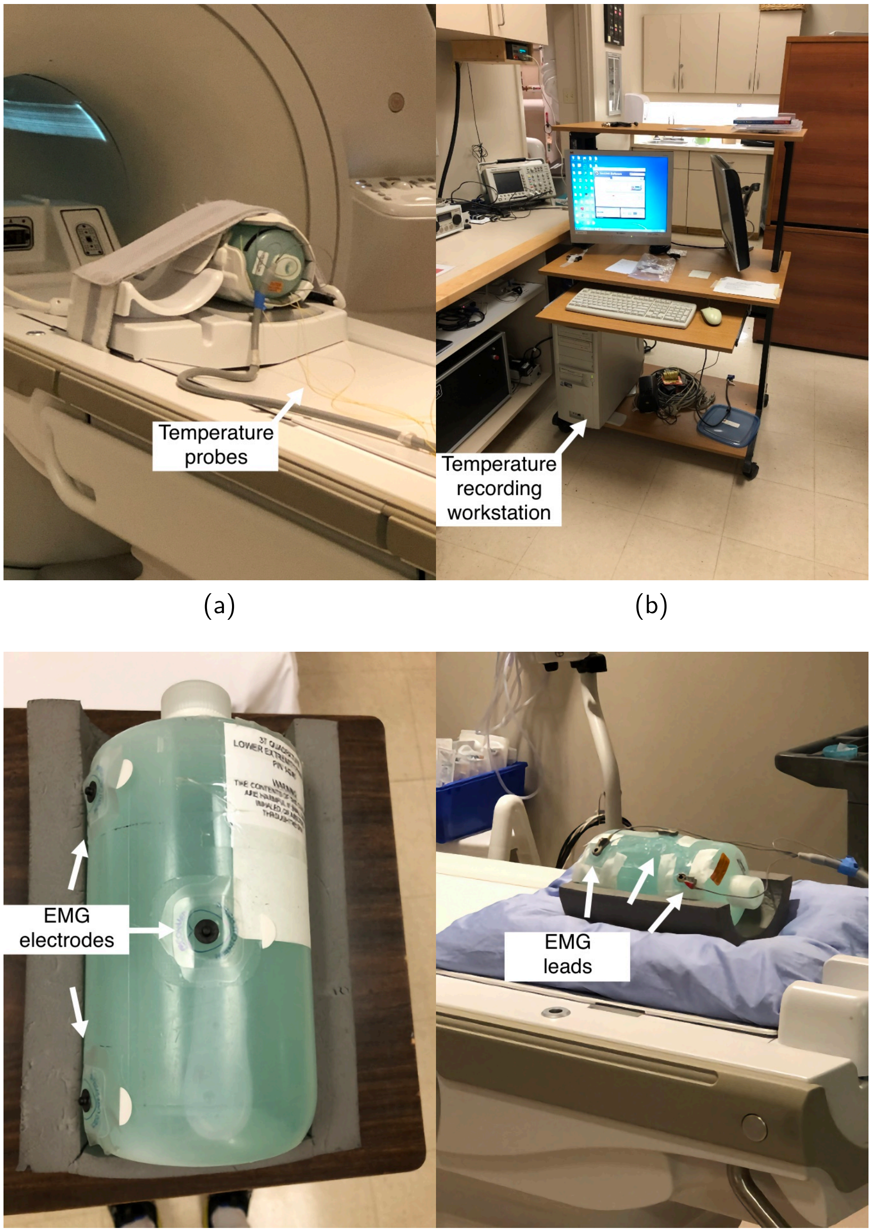

(a) (b)

(c) (d)

Figure 7.2: EMG and temperature hardware setup for the cylindrical phantom. The temperature recording workstation was outside the MRI room, in the control room.

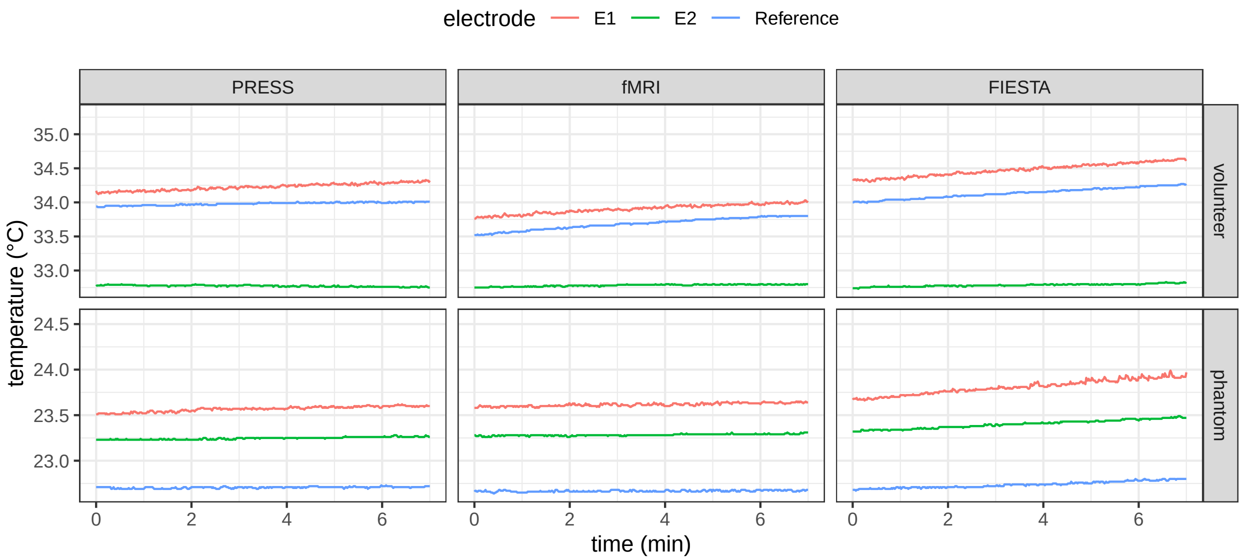

Figure 7.3: Temperature recordings over time of the phantom and volunteer under the three sequences tested. Each EMG electrode was monitored alone.

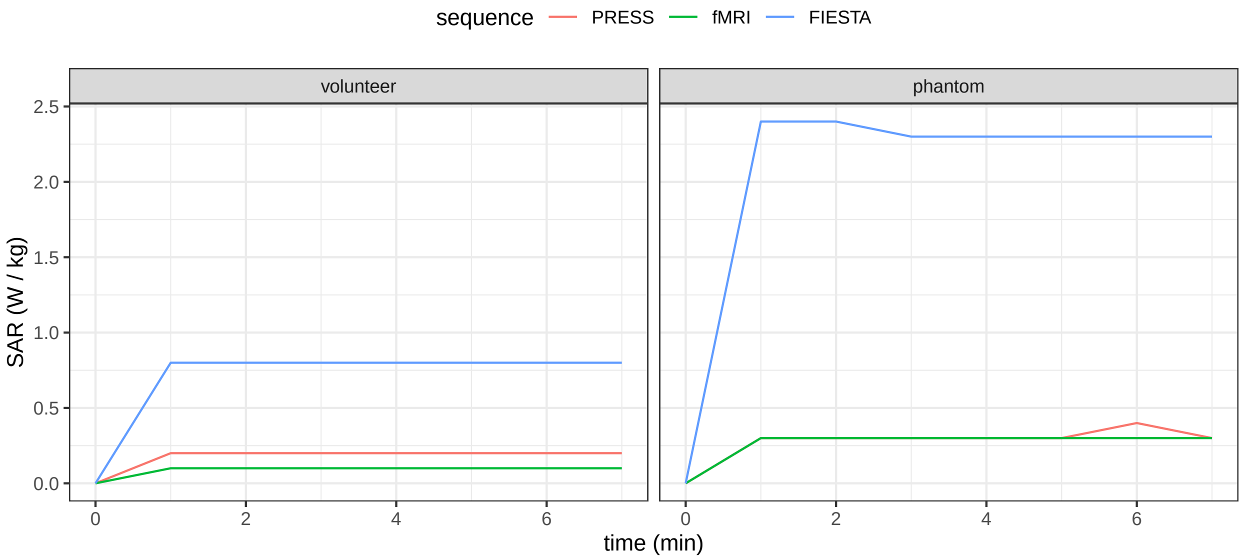

Figure 7.4: SAR recordings over time of both the phantom and volunteer under the three sequences tested. As observed for all the recordings, the SAR seems to reach a steady value after ∼1min.

Table 7.1: Temperature [1]minimum, maximum of both the phantom and volunteer under the three sequences tested. Temperature units: °C.

	phantom			**volunteer**		
Electrode	**FIESTA**[1]	**fMRI**[1]	**PRESS**[1]	**FIESTA**[1]	**fMRI**[1]	**PRESS**[1]
E1	23.7, 24.6	23.6, 23.7	23.5, 23.6	34.3, 35.3	33.8, 34.1	34.1, 34.3
E2	23.3, 23.8	23.3, 23.3	23.2, 23.3	32.7, 33.0	32.8, 32.8	32.8, 32.8
Reference	22.7, 23.1	22.6, 22.7	22.7, 22.7	34.0, 34.7	33.5, 33.9	33.9, 34.0

Table 7.2: SAR [1]mean (standard deviation) of both the phantom and volunteer under the three sequences tested. SAR units: W/kg.

Sequence	**phantom**[1]	**volunteer**[1]
PRESS	0.28 (0.12)	0.18 (0.07)
fMRI	0.27 (0.09)	0.09 (0.03)
FIESTA	2.25 (0.53)	0.77 (0.16)

7.2.4 Discussion

Three sequences were tested to guarantee the safety of volunteers during the simultaneous acquisition of fMRI/EMG. Even though the FIESTA sequence was not used during any of the experiments, it was included as the 'worst case scenario' because it is an intensive RF sequence. Unlike FIESTA, the ^{1}H-MRS and fMRI sequences were thoroughly used during the experiments (Sequence B. and D., respectively).

The SAR and temperature limits according to the IEC standard 60601-2-33 is 2.0 W/kg and 39°C, during a typical whole-body MRI scan [18]. As seen from the experiments executed, none of the sequences exceeded the SAR limit (maximum for volunteer: 0.77 ± 0.16W/kg) nor the temperature limit (maximum for volunteer, electrode E1: 35.3°C). In conclusion, this experiment has shown that the safety of the volunteer during simultaneous acquisitions of fMRI/EMG is guaranteed with the proposed in-house developed hardware.

7.3 Denoising of the Gradient Artifact

7.3.1 Disclosure

This chapter was written by Alejandro Amador-Tejada with the intention of publishing as a technical note and is part of a collaboration with Joshua Ethan McGillivray and Dr. Michael D. Noseworthy. The intended author's order is Alejandro Amador-Tejada, Joshua Ethan McGillivray and Dr. Michael D. Noseworthy. The planned publication is awaiting the acquisition of more EMG datasets from 4 more subjects to confirm the results.

In addition, this chapter will be submitted as an abstract for the *2023 ESMRMB Annual Meeting & Exhibition* from the $04^{\text{th}} - 07^{\text{th}}$ October 2023 in Basel, Switzerland.

7.3.2 Background

During simultaneous acquisitions of muscle BOLD/EMG or brain fMRI/EMG, the GA is the primary source of interference on the EMG recordings caused by the MRI environment. Since the GA is virtually the same artifact that affects both EMG and EEG recordings, techniques already described to denoise simultaneous fMRI/EEG recordings from the GA can be applied to simultaneous acquisitions of BOLD-fMRI/EMG. These techniques include the average artifact subtraction (AAS) algorithm [19, 20], or more complex and computationally intensive methods such as temporal independent component analysis [21], temporal principal component analysis [22], and independent vector analysis [23].

In contrast to a typical simultaneous acquisition of fMRI/EEG, there is no dedicated hardware to remove the GA easily, *i.e.* there is no specific system to record the EMG signal while saving the slice-timing information from the MRI scanner used as input for the AAS algorithm. To compensate for this issue, study groups have focused on improving the coupling of fMRI and EMG by adapting an MRI-compatible EEG acquisition system to serve as an EMG recording system [13, 24, 25]. However, several drawbacks arise with this technique, such as the requirement of additional and expensive MRI-compatible hardware (which not every MRI centre has access to), the extra time to set up this hardware (taking up to ∼15 min per scan), and the use of electrodes and system electronics not optimized for EMG acquisitions. Other study groups have recorded EMG prior/post scanning outside the MRI environment [7], yet, this yields two different muscle activation events. *i.e.* the activation from EMG does not correspond to the one from BOLD, as they were not recorded simultaneously. Thus, the use of simultaneous BOLD-fMRI/EMG acquisitions is hampered by the need for more development to denoise the EMG signals from the GA in a cost-effective and time-efficient form. The objective of this research was to investigate denoising procedures that require different setup times, hardware and post-processing levels to remove the GA from simultaneous BOLD/EMG recordings.

7.3.3 Methods

Simultaneous BOLD signals and surface EMG recordings (Chapter 3.2) were acquired from one volunteer (age = 23 yrs, height = 178 cm, weight = 65 kg). The BOLD sequence used during these acquisitions is described elsewhere (Sequence E.). All the MRI setup followed the steps already described in Chapter 3.1. EMG recordings were taken simultaneously (*inside MRI, BOLD*) for 5 minutes, following a block design of rest/activation of 1 min. The rest/activation pattern consisted of 30s of rest followed by 30s of plantar flexion exercise (yielding five rest-activation repetitions as shown in Fig. 7.5), using the in-house MRI-compatible EMG acquisition system and ergometer, described in Chapter 3.2 and 3.3, respectively. The weight loads of the ergometer were adjusted to 40% MVC of the subject.

To investigate the optimal approach to denoise the EMG signal from the gradient artifact, three denoising methods (requiring different levels of hardware and processing pipelines) were tested. These denoising methods were:

M1: This method is similar to a typical brain fMRI/EEG simultaneous acquisition. The MRI scanner internal clock output is connected via a BNC connector to a BrainVision SyncBox system (*Brain Products GmbH, Montreal QC, Canada*) as shown in Fig. 7.6. While scanning, the MRI generates a TTL pulse received and stored by the BrainVision SyncBox, which is finally used as the slice-timing

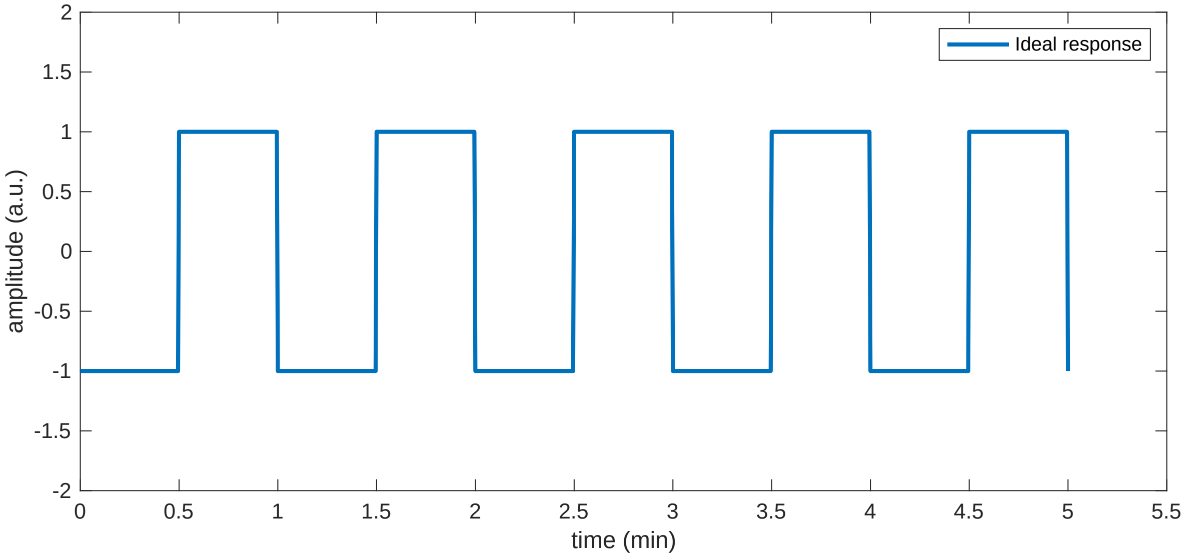

Figure 7.5: Plot showing the ideal response function, *i.e.* the exercise sequence used for the acquisition of simultaneous BOLD/EMG. The exercise was 5min long, with a block design of 1 min consisting 30s of rest followed by 30s of exercise.

trigger for denoising the signal [20]. Thus, this method requires the use of extra hardware such as the BrainVision SyncBox along with the BrainVision Recorder, MRI-compatible amplifiers, BrainVision software and workstation (Fig. 7.7), with an average setup time of ∼15 min.

Once the slice-timing triggers are collected, the file is recovered and fused with the EMG recordings. Both are initialized simultaneously to ensure proper temporal alignment between the TTL and EMG recording systems.

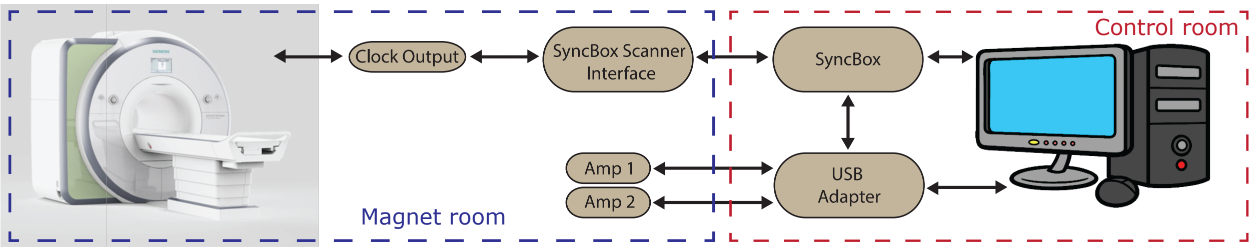

Figure 7.6: A typical brain fMRI/EEG setup requires the connection of the EEG workstation to the EEG amplifiers and the SyncBox to retrieve the MRI slice-timing information. The hardware required in the control room is shown in Fig. 7.7.

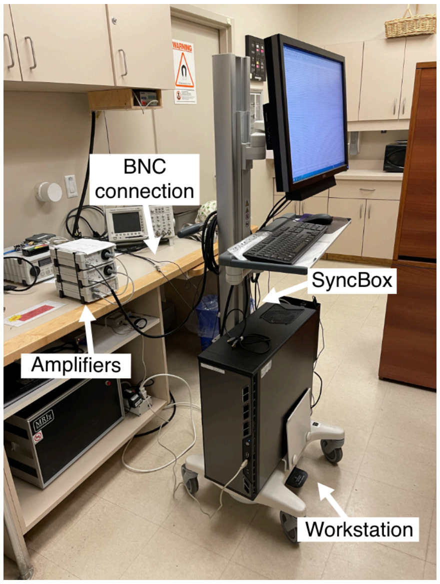

Figure 7.7: MRI-compatible fMRI/EEG hardware used for simultaneous acquisitions of muscle BOLD/EMG. The EEG workstation, the BrainVision SyncBox system, BNC connections, and amplifiers (*Brain Products GmbH, Montreal QC, Canada*) are shown. This setup was used for method *M1* and to assess the periodicity of the GA.

M2: If the slice-timing triggers are equally distant in time, *i.e.* if the slice selection gradient is played periodically without any significant variation in time, then an alternative to **M1** can be used. This method artificially builds a constant slice-timing trigger template without using extra hardware to record the TTL pulses from the MRI, reducing setup time and processing steps. For this method, the periodicity of the slice selection gradient is determined using previous slice-timing triggers from the MRI.

M3: In the case where the slice selection gradient has significant time variations, *i.e.* **M2** is not feasible, this method proposes to manually build the slice-timing triggers from the local maxima of the gradient artifact in the EMG recordings. As with **M2**, this method would not require any additional hardware, although it will need extra processing steps.

The AAS algorithm

The temporal nature of the GA has been well characterized [14, 19], suggesting that the GA is relatively periodic, which boosted the development of denoising techniques to suppress it from EEG signal, such as the AAS algorithm. This algorithm has been thoroughly reviewed elsewhere [20, 22]. Briefly, the AAS is based on subtracting an average artifact template from a signal. Given that the artifact is relatively periodic, the artifact template is built from the raw signal, starting with the division of the signal into segments ($\mathrm{W}_{\mathrm{i}'\mathrm{s}}$) of the length of the period, then a selected number of windows are averaged $[\cdots \mathrm{W}_{\mathrm{i}-2}, \mathrm{W}_{\mathrm{i}-1}, \mathrm{W}_{\mathrm{i}}, \mathrm{W}_{\mathrm{i}+1}, \mathrm{W}_{\mathrm{i}+2} \cdots]$ creating the artifact template, as shown in Fig. 7.8. The AAS method has been proven highly effective to denoise the GA from EEG recordings in simultaneous studies of brain fMRI/EEG [14].

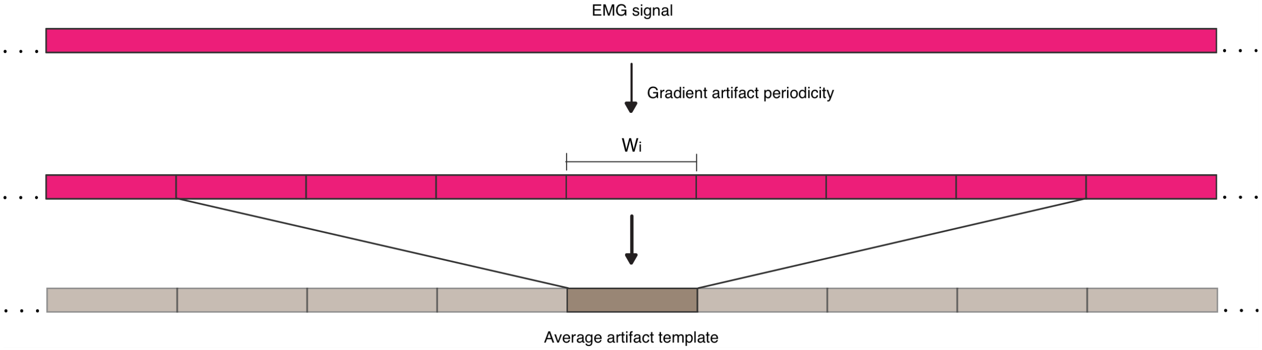

Figure 7.8: Schematic showing the process of building the average artifact template.

The AAS algorithm is the basis of the previously described denoising methods (*M1*, *M2*, *M3*). As such, the main objective of this experiment was to create slice-timing trigger templates. These templates would contain the periodicity of the GA, used to feed the AAS algorithm to denoise the EMG signals. All the denoising procedures were performed using the FMRIB plug-in [22, 26].

In addition, to compare the quality of the EMG signal after the denoising process, EMG recordings were taken inside the MRI without any sequence running (*inside MRI, no BOLD*) and outside the MRI magnet room (*outside MRI*). Two EMG recordings were taken for each condition: *inside MRI, BOLD*; *inside MRI, no BOLD*; and *outside MRI* (Fig. 7.9).

Following the denoising of the EMG recordings that were taken inside the MRI (*inside MRI, BOLD*), all recordings were post-processed with a band-pass filter @20-500Hz and line filter @60Hz. Finally, an SNR analysis was performed to assess the efficacy of the denoising methods and to compare any differences with both *inside MRI, no BOLD* and *outside MRI* conditions. After all EMG recordings were denoised and preprocessed, the SNR of each rest-activation repetition was computed, yielding a total of 5 SNR measurements per EMG recording. Subsequently, two repeated measures ANCOVA were used to investigate the hypothesis shown below. The EMG root mean square (RMS), a metric indicative of muscle fatigue, was calculated for each rest-activation pair and used as a covariate.

- 1-way ANCOVA, with the denoising methods as a factor and the EMG RMS as a covariate.
  - Are there any differences in the SNR between denoising methods (*M1*, *M2*, *M3*)?
    i.e. $\mathrm{H_0(SNR)} = \mu_{\mathrm{M1}} = \mu_{\mathrm{M2}} = \mu_{\mathrm{M3}}$
- 2-way ANCOVA, with the conditions and rest-activation repetitions as factors and the EMG RMS as a covariate.
  - Are there any differences in the SNR between conditions (*inside MRI, BOLD*; *inside MRI, no BOLD*; and *outside MRI*)?
    i.e. $\mathrm{H_0(SNR)} = \mu_{\mathrm{insideMRI,noBOLD}} = \mu_{\mathrm{insideMRI,BOLD}} = \mu_{\mathrm{outsideMRI}}$
  - Are there any differences in the SNR between rest-activation repetitions ($\mathrm{i} = 1, 2, 3, 4, 5$)?
    i.e. $\mathrm{H_0(SNR)} = \mu_1 = \mu_2 = \mu_3 = \mu_4 = \mu_5$

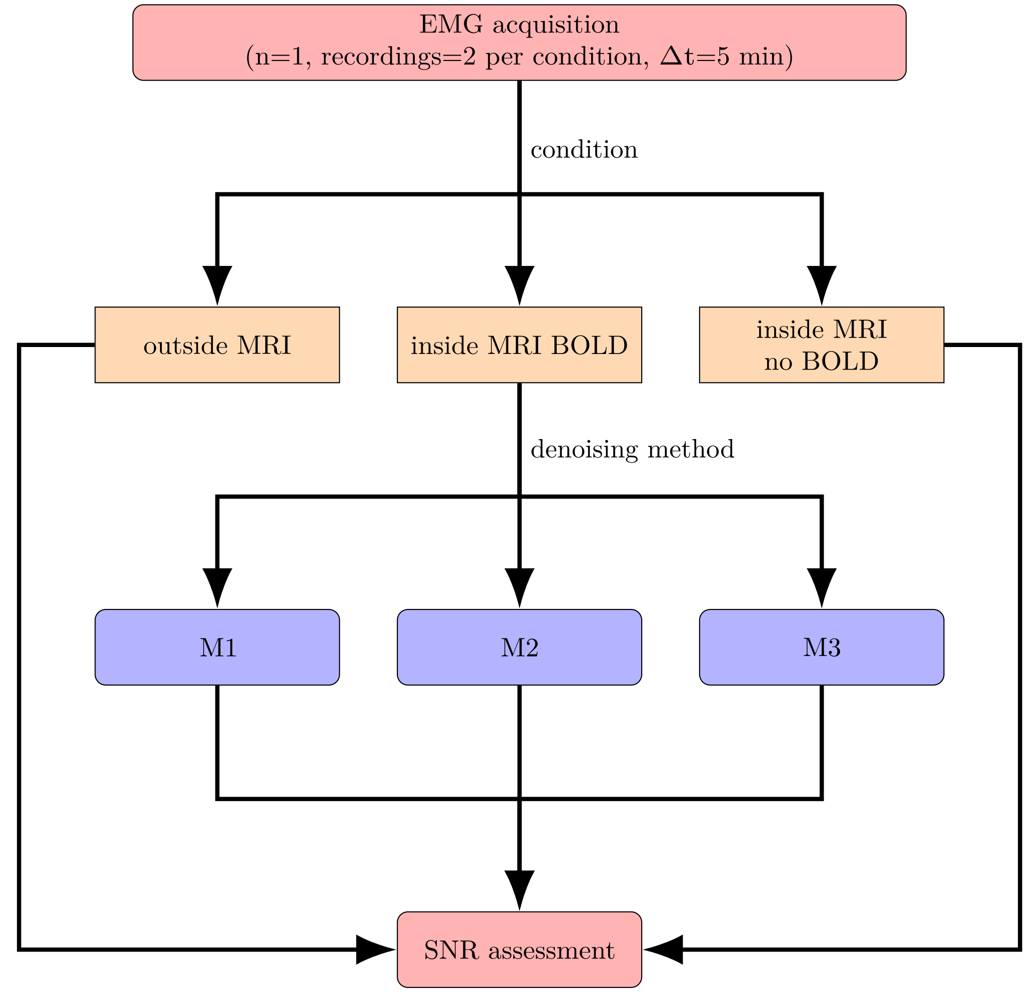

Figure 7.9: Flowchart of EMG acquisition during three different conditions (*inside MRI, BOLD*, *inside MRI, no BOLD*, and *outside MRI*) with three different denoising methods (*M1*, *M2*, *M3*). To assess the effectiveness of each method, the SNR was compared between conditions. A total of 6 EMG recordings (3 conditions × 2 recordings × 1 subject) were collected. Five SNR measurements, corresponding to 5 rest-activation repetitions, were extracted from each recording, yielding a total of 50 SNR measurements.

7.3.4 Results

Six EMG recordings (3 conditions × 2 recordings × 1 subject) were collected. Raw recordings inside the MRI with the muscle BOLD sequence (condition of *inside MRI, BOLD*) are shown in Fig. 7.10(blue). As seen, the GA hides the EMG content leaving the EMG acquisitions of no use. Amplification of a raw EMG recording with the GA can be observed in Fig. 7.11(top), where the periodicity of the artifact is seen.

Slice-timing information was collected from the BrainVision EEG hardware, where the period of the gradient artifact was $0.125 \pm 4.89 \times 10^{-5}$s as shown in Fig. 7.12(left). Thus, showing a relatively well-behaved periodicity which enabled the utilization of the denoising method *M2*.

After the characterization of the GA, the three denoising methods were tested:

- by using the slice-timing information collected directly from the EEG hardware (*M1*)
- by artificially building a slice-timing template assuming a regular artifact with a period of $\mathrm{T_R}/\#$ slices (*M2*)
- by manually finding the artifact period of the contaminated EMG signal (*M3*).

Method *M3* consisted of a band-pass filter @5-500Hz followed by a peak detection as shown in Fig. 7.12(right), yielding an average artifact period of $0.125 \pm 6.39 \times 10^{-5}$s. The results of the three methods can be seen in Fig. 7.10(orange), where visually, there seem to be no apparent differences in the denoised signals. The denoised and post-processed EMG recordings for the three conditions are shown in Fig. 7.13 and 7.14, where for all conditions, denoising methods and trials, the rest-activation repetitions are clearly distinguishable.

The SNR of the five rest-activation repetitions was computed for all the EMG recordings (Fig. 7.15), yielding a total of 50 SNR calculations. Two EMG recordings sections that showed movement artifacts were excluded from the SNR. A repeated measures 1-way ANCOVA was performed to assess the effectiveness of the denoising methods, and a repeated measures 2-way ANCOVA was conducted to compare the SNR between conditions and rest-activation repetitions. First, the statistical test between denoising methods failed to reject the null hypothesis (p = 0.982) as seen in Fig. 7.16 and 7.18(bottom) suggesting any of the denoising methods could be used. Moreover, testing for differences in the mean SNR between environment conditions (*inside MRI, BOLD* = High noise, *inside MRI, no BOLD* = Moderate noise, and *outside MRI* = Low noise) failed to reject the null hypothesis (p = 0.748) as seen in Fig. 7.18(top, right). Finally, testing for differences in the mean SNR between rest-activation windows, *i.e.* the SNR of each period (p = 0.48) as shown in Fig. 7.17 and 7.18(top, left). Finally, the EMG RMS measurement used as a covariate showed no statistical difference for both ANCOVA tests (Fig. 7.16 and 7.17).

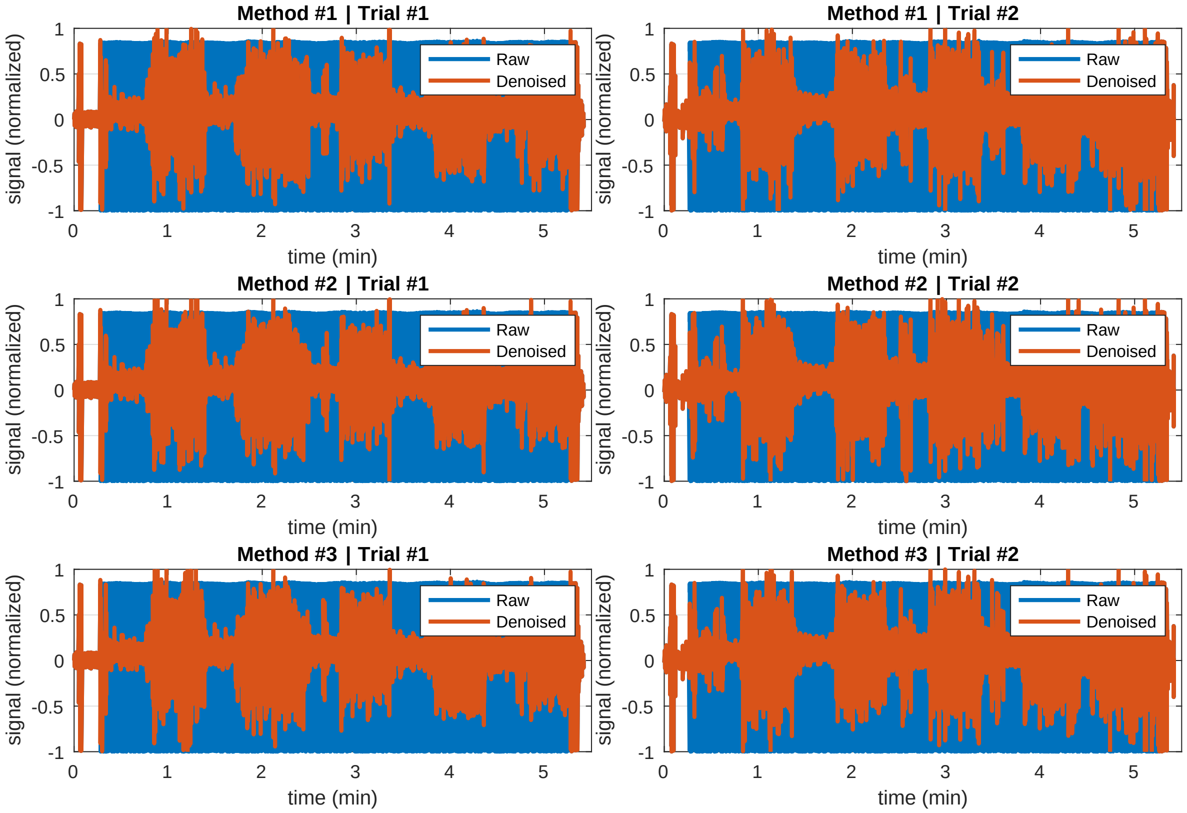

Figure 7.10: (Blue) Raw EMG recordings with the GA, because it is relatively periodic, the AAS algorithm can be used, provided that an artifact template can be obtained. (Orange) Denoised EMG recordings for the three used methods (*M1*, *M2*, *M3*) and the two recordings taken. The raw data plot shows that the GA masks the real EMG signal, making it useless unless denoised correctly.

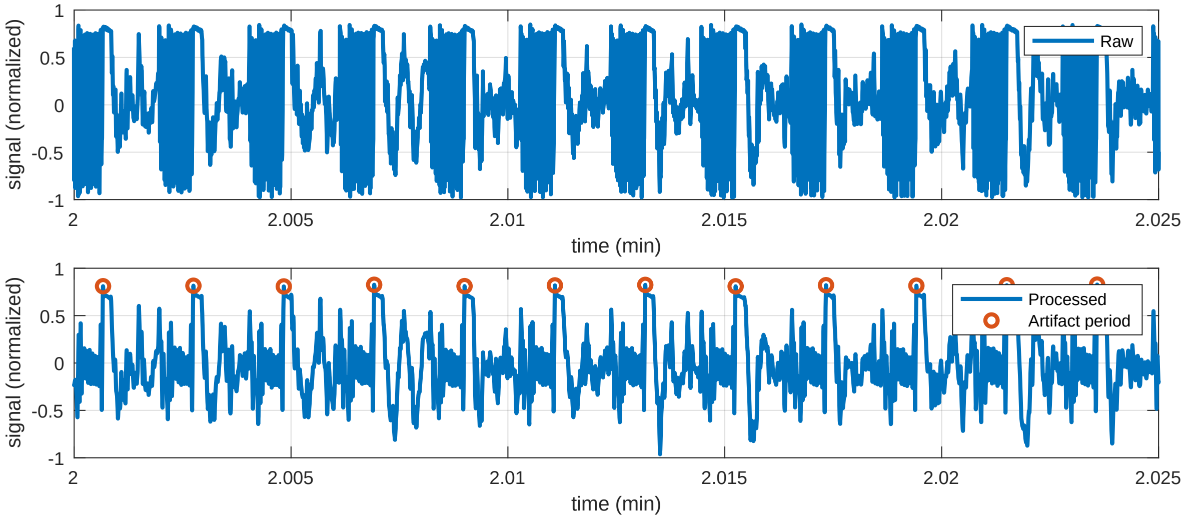

Figure 7.11: EMG raw signal amplified within 2-2.025s (top) and after band-pass filtering to enhance the peak detection of the GA periodicity (bottom). Without the filtering, there is no clear peak to use as the start/end of the GA, thus difficulting the building of the slice-timing template for method *M3*.

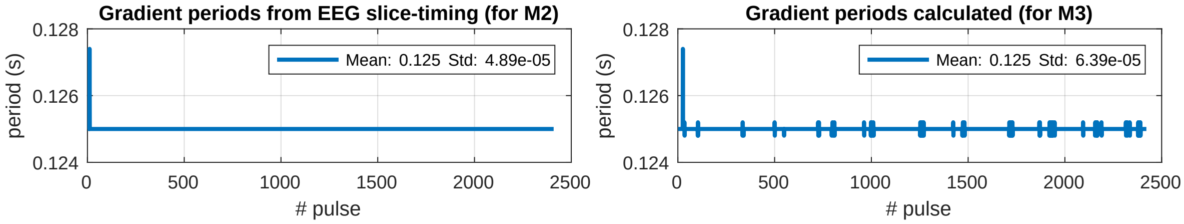

Figure 7.12: (Left) Extracted timing pulse information from the BrainVision system from method *M1*. The plot shows the consistent timing between TTL pulses, *i.e.* slice-timing information, as a function of the pulse/slice selection gradient number. Aside from only one period measuring ∼ 0.128s at the beginning, no significant variations were found in the gradient artifact signal. Furthermore, the average periodicity of the GA was $0.125 \pm 4.89 \times 10^{-5}$s. (Right) The manually slice-timing template built from the EMG signal (for method *M3*, Fig. 7.11) showed small variations in the periodicity, slightly increasing the standard deviation from 4.89×10^{-5}s to 6.39×10^{-5}s.

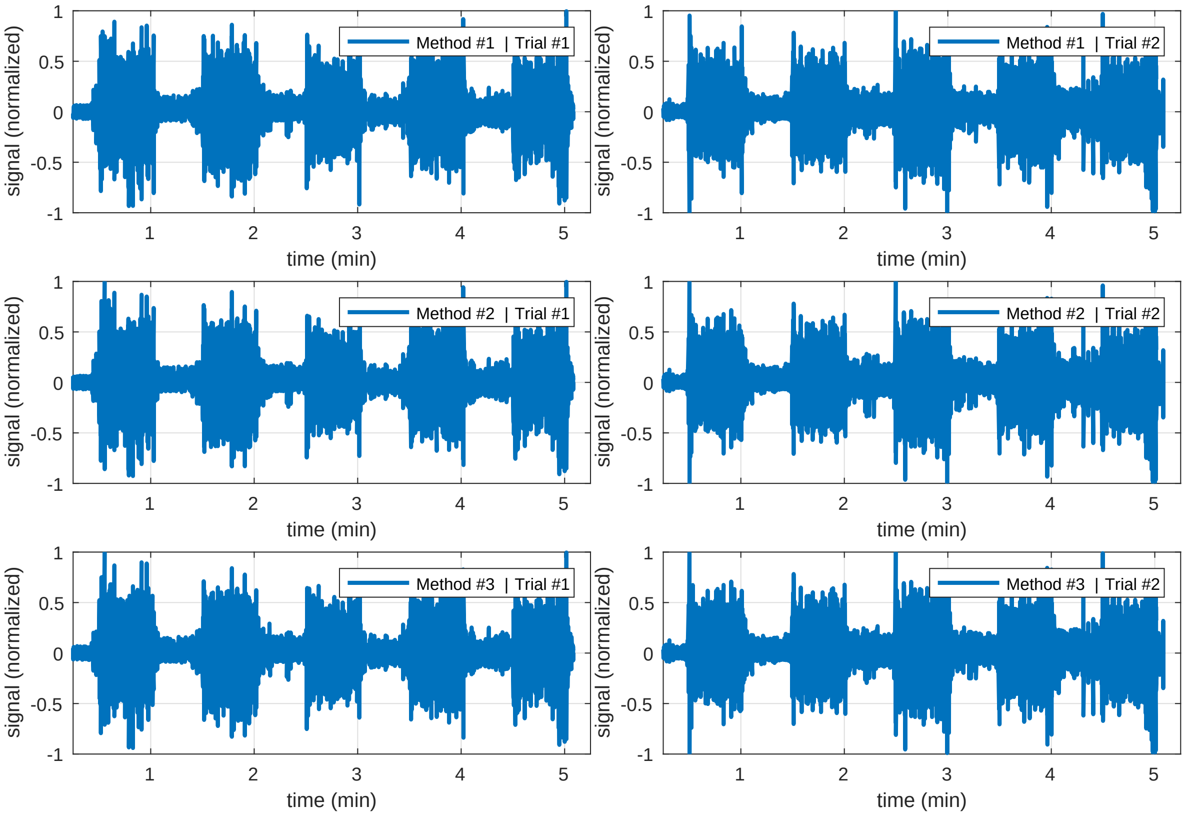

Figure 7.13: EMG recordings *inside MRI, BOLD* after GA denoising (*M1*, *M2*, *M3*) and filtering.

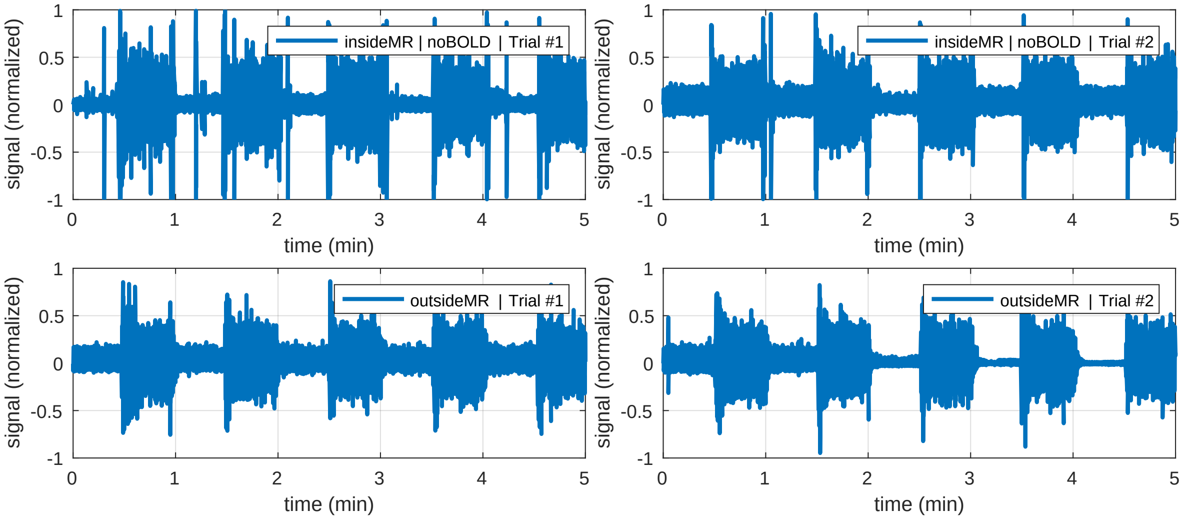

Figure 7.14: Post-processed EMG recordings *inside MRI, no BOLD*(top) and *outside MRI*(bottom).

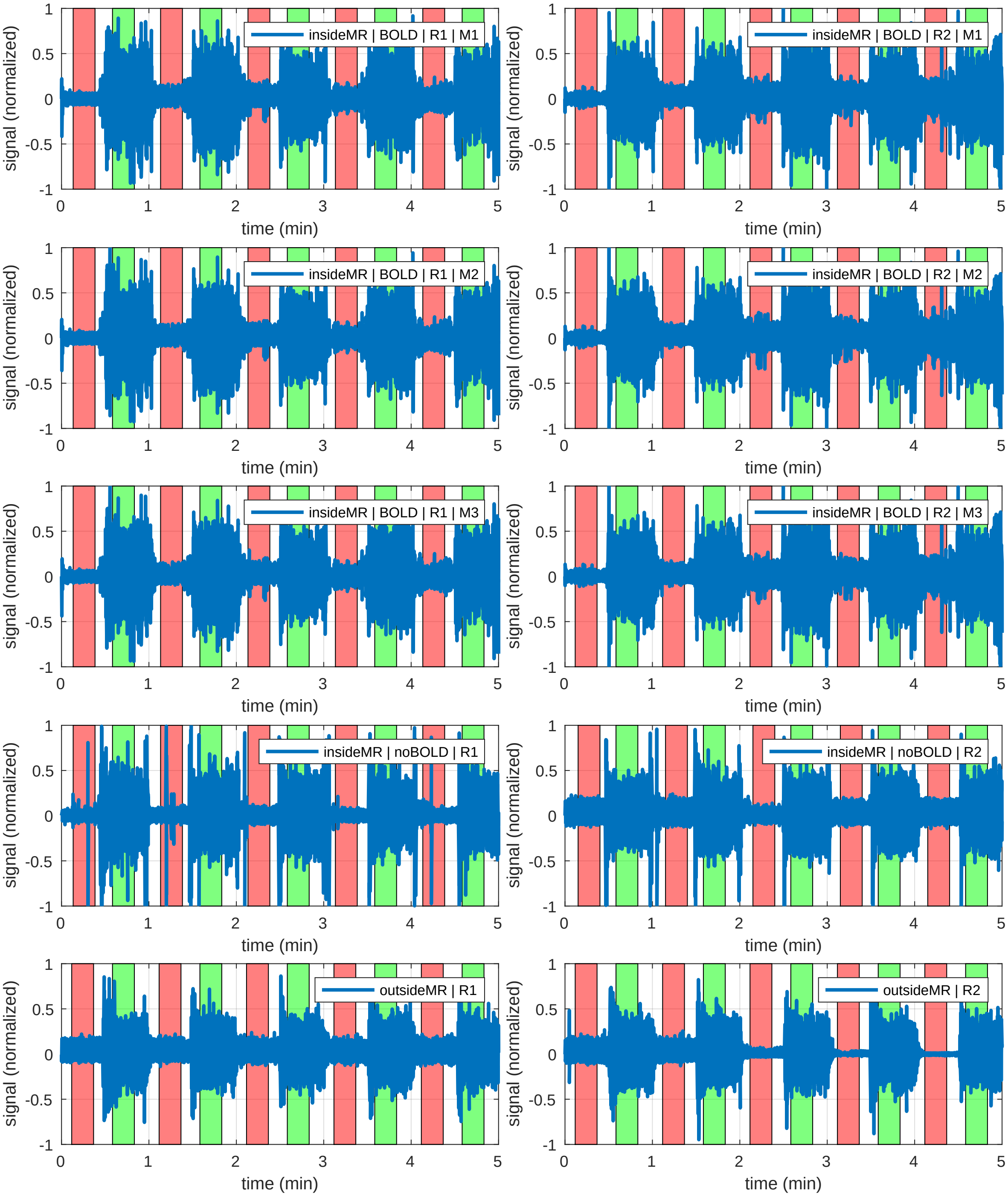

Figure 7.15: SNR windows or rest(red)-activation(green) pairs selection for all the EMG recordings. A total of 50 SNR measurements were computed: [2 conditions (*inside MRI, no BOLD*, *outside MRI*) + 1 condition (*inside MRI, BOLD*) × 3 denoising methods] × 5 rest-activations repetitions × 2 recordings. (Left column) Recordings #1, (Right column) Recordings #2.

```
## Type III Analysis of Variance Table
##        Sum Sq Mean Sq DF F value Pr(>F)
## method  0.503   0.251  2  0.0185 0.9817
## rms    37.804  37.804  1  2.7831 0.1074
## ---
## Signif. codes:  0 '***' 0.001 '**' 0.01 '*' 0.05 '.' 0.1 ' ' 1
```

Figure 7.16: Repeated measures 1-way ANCOVA results testing differences in the mean SNR for the three denoising methods (*M1*, *M2*, *M3*). With p = 0.982, it has failed to reject the null hypothesis that the mean SNR is the same for the three denoising methods. (significance level was set to p<0.05).

```
## Type III Analysis of Variance Table
##           Sum Sq Mean Sq DF F value Pr(>F)
## window    72.670 18.1674  4  0.8944 0.4758
## condition 30.302 15.1512  2  0.7459 0.4805
## rms        2.130  2.1301  1  0.1049 0.7477
## ---
## Signif. codes:  0 '***' 0.001 '**' 0.01 '*' 0.05 '.' 0.1 ' ' 1
```

Figure 7.17: Repeated measures 2-way ANCOVA results testing differences in the mean SNR for the five rest-activations repetitions, and the three conditions (*inside MRI, BOLD*, *inside MRI, no BOLD*, and *outside MRI*). With p = 0.48, it has failed to reject the null hypothesis that the mean SNR is the same for the five rest-activations pairs. Finally, with p = 0.748, it has failed to reject the null hypothesis that the mean SNR is the same for the three conditions (significance level was set to p<0.05).

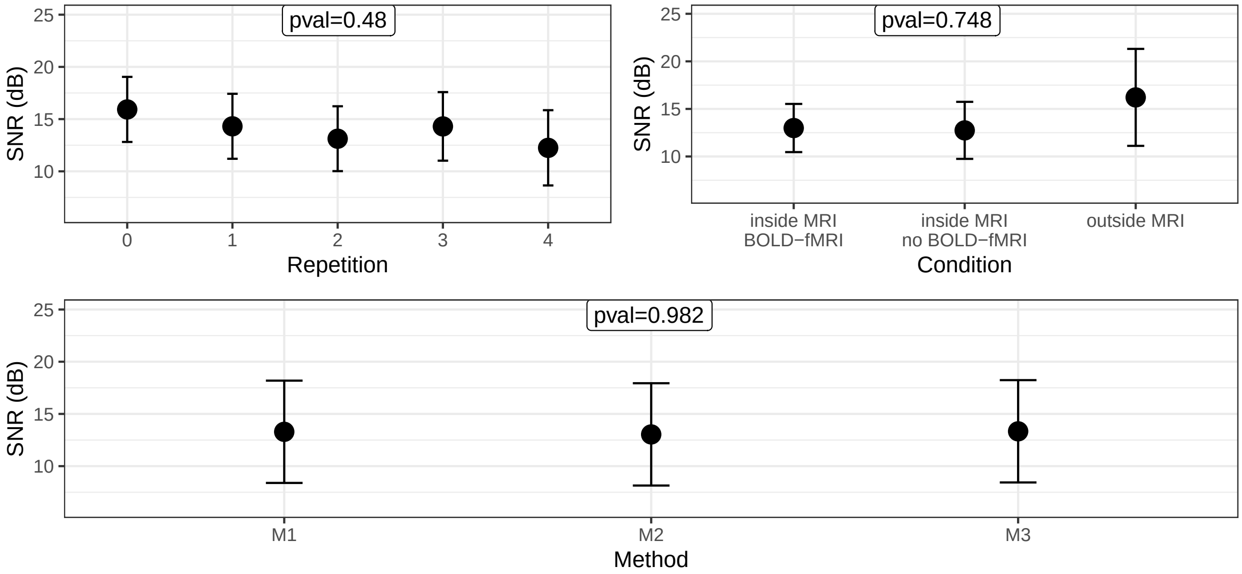

Figure 7.18: Estimated mean and confidence intervals for the SNR measurements between windows or rest-activation pairs (top, left), between conditions (top, right) and between denoising method (bottom).

7.3.5 Discussion

Through the characterization of the GA, it has been shown that the artifact is periodic with a negligible variation, therefore allowing the execution of method M2 and facilitating the processing of method M3. Manually building of the slice-timing triggers from the raw EMG recording presented no significant challenges, mainly due to the high periodicity of the artifact.

The test performed within the denoising methods suggested no statistically significant differences in the mean SNR across methods, suggesting that any of the three methods can be chosen to denoise the EMG signal from the GA. Even though the three methods are equally helpful, the hardware and post-processing required for each were different. First, method M1 requires the highest amount of hardware, including the EEG workstation, along with the BrainVision SyncBox system, BNC connections and amplifiers (*Brain Products GmbH, Montreal QC, Canada*) plus extra setup time ($\sim$15min) and additional post-processing steps ($\sim$10min). On the contrary, given the fact that the GA is periodic, methods *M2* and *M3* can be used, these methods do not require additional settings saving time and the acquisition of specialized hardware.

It is well-known that the MRI environment adversely impacts simultaneous fMRI/EMG acquisitions. Even though there are several procedures to reduce the interference between both techniques, the effect of the MRI environment on EMG recordings has yet to be compared to a typical EMG recording outside or inside the MRI magnet room without any sequence running. This study aimed to fill this gap, showing that there is no significant difference in the mean of SNR between the three conditions under which the EMG recordings were taken. This suggests that electrical sources of noise inside the MRI environment, which were previously reported to be an issue [27], are not contributing to the EMG signal compared to an EMG recorded outside the MRI magnet room.

The use of an exercise protocol of 5min at 40%MVC could introduce some variability in the SNR measurements due to muscle fatigue. The EMG RMS, which typically increases with fatigue [28, 29], shows no statistically significant differences as a covariate, suggesting that fatigue did not influence the experimental design. In addition, the statistical non-significance in the SNR measurement across rest-activation pairs supports the consistency of muscle contraction throughout the EMG recordings.

In conclusion, the current research proposes that EMG recordings contaminated with the gradient artifact, coming from simultaneous acquisitions of fMRI/EMG, can be denoised using the AAS algorithm with the methods presented here. Method M2 was the easiest to run, requiring no extra hardware, no additional setup time and a simple post-processing pipeline. These advantages could increase the use of EMG during fMRI studies. The decision as to which method would be optimal will exclusively rely on the available hardware, time availability and processing capabilities of each MRI centre. Nonetheless, each MRI centre should confirm the periodicity of the gradient artifact to apply method *M2* or *M3*.

Limitations

The following points are considered to be limitations of the current research:

- The objective of this chapter was to assess the quality of a denoising method to clean electrophysiological signals contaminated with the GA from the MRI environment. As such, the interest was focused mainly on the denoising technique rather than the EMG acquisition. For this reason, only one participant was recruited for all the experiments. It is recognized that the sample size for publication purposes is extremely low, and the authors are aiming to recruit 5 more participants. The authors do not expect significant changes in the results as what is being tested is the denoising method, not the quality of the exercise from the participants.

References

1. Mullinger, K. J., Morgan, P. S. & Bowtell, R. W. Improved artifact correction for combined electroencephalography/functional MRI by means of synchronization and use of vectorcardiogram recordings. *J. Magn. Reson. Imaging* **27,** 607–616. doi:`10.1002/jmri.21277` (2008).
2. Johansen-Berg, H. *et al.* The role of ipsilateral premotor cortex in hand movement after stroke. *Proc. National Acad. Sci.* **99,** 14518–14523. doi:`10.1073/pnas.222536799` (Oct. 29, 2002).
3. White, A. *et al.* Brain activation in multiple sclerosis: a BOLD fMRI study of the effects of fatiguing hand exercise. *Multiple Scler. J.* **15,** 580–586. doi:`10.1177/1352458508100034` (May 1, 2009).
4. McGillivray, J. E. *et al.* The Effect of Exercise on Neural Activation and Cognition: A Review of Task-Based fMRI Studies. *Crit. Rev. Biomed. Eng.* **49.** doi:`10.1615/CritRevBiomedEng.2021038975` (2021).
5. Fontes, E. B. *et al.* Brain activity and perceived exertion during cycling exercise: an fMRI study. *Br. J. Sports Med.* **49,** 556–560. doi:`10.1136/bjsports-2012-091924` (Apr. 1, 2015).
6. Bigliassi, M. *et al.* Cerebral effects of music during isometric exercise: An fMRI study. *Int. J. Psychophysiol.* **133,** 131–139. doi:`10.1016/j.ijpsycho.2018.07.475` (Nov. 1, 2018).
7. Ehrsson, H. H., Fagergren, A. & Forssberg, H. Differential Fronto-Parietal Activation Depending on Force Used in a Precision Grip Task: An fMRI Study. *J. Neurophysiol.* **85,** 2613–2623. doi:`10.1152/jn.2001.85.6.2613` (June 2001).
8. Liu, J. Z. *et al.* Human Brain Activation During Sustained and Intermittent Submaximal Fatigue Muscle Contractions: An fMRI Study. *J. Neurophysiol.* **90,** 300–312. doi:`10.1152/jn.00821.2002` (July 2003).
9. Al-Mulla, M. R., Sepulveda, F. & Colley, M. A Review of Non-Invasive Techniques to Detect and Predict Localised Muscle Fatigue. *Sensors* **11,** 3545–3594. doi:`10.3390/s110403545` (Apr. 2011).
10. Ritter, P. *et al.* in *EEG-fMRI: physiological basis, technique, and applications* (eds Mulert, C. & Lemieux, L.) (Springer Science & Business Media, 2009).
11. Delorme, A. & Makeig, S. EEGLAB: an open source toolbox for analysis of single-trial EEG dynamics including independent component analysis. *J. Neurosci. Methods* **134,** 9–21. doi:`10.1016/j.jneumeth.2003.10.009` (Mar. 15, 2004).
12. Neuner, I. *et al.* Electrophysiology meets fMRI: Neural correlates of the startle reflex assessed by simultaneous EMG–fMRI data acquisition. *Hum. Brain Mapp.* **31,** 1675–1685. doi:`10.1002/hbm.20965` (2010).
13. Van Duinen, H. *et al.* Surface EMG measurements during fMRI at 3T: Accurate EMG recordings after artifact correction. *NeuroImage* **27,** 240–246. doi:`10.1016/j.neuroimage.2005.04.003` (Aug. 1, 2005).
14. Yan, W. X. *et al.* Understanding gradient artefacts in simultaneous EEG/fMRI. *NeuroImage* **46,** 459–471. doi:`10.1016/j.neuroimage.2009.01.029` (June 1, 2009).
15. Tokue, H., Tokue, A. & Tsushima, Y. Unexpected magnetic resonance imaging burn injuries from jogging pants. *Radiol. Case Reports* **14,** 1348–1351. doi:`10.1016/j.radcr.2019.08.015` (Nov. 1, 2019).
16. Abdel-Rehim, S. *et al.* Burns from ECG leads in an MRI scanner: Case series and discussion of mechanisms. *Ann. Burn. Fire Disasters* **27,** 215–218 (Dec. 31, 2014).
17. International Electrotechnical Commission. Medical electrical equipment. Particular requirements for the safety of magnetic resonance equipment for medical diagnosis. *Int. Stand. IEC60601-2-33* (2002).
18. Seo, Y. & Wang, Z. J. Measurement and evaluation of specific absorption rate and temperature elevation caused by an artificial hip joint during MRI scanning. *Sci. Reports* **11,** 1134. doi:`10.1038/s41598-020-80828-7` (Jan. 13, 2021).
19. Allen, P. J. *et al.* Identification of EEG Events in the MR Scanner: The Problem of Pulse Artifact and a Method for Its Subtraction. *NeuroImage* **8,** 229–239. doi:`10.1006/nimg.1998.0361` (Oct. 1, 1998).
20. Allen, P. J., Josephs, O. & Turner, R. A Method for Removing Imaging Artifact from Continuous EEG Recorded during Functional MRI. *NeuroImage* **12,** 230–239. doi:`10.1006/nimg.2000.0599` (Aug. 1, 2000).
21. Liu, Z. *et al.* Statistical feature extraction for artifact removal from concurrent fMRI-EEG recordings. *NeuroImage* **59,** 2073–2087. doi:`10.1016/j.neuroimage.2011.10.042` (Feb. 1, 2012).
22. Niazy, R. K. *et al.* Removal of FMRI environment artifacts from EEG data using optimal basis sets. *NeuroImage* **28,** 720–737. doi:`10.1016/j.neuroimage.2005.06.067` (Nov. 15, 2005).
23. Acharjee, P. P. *et al.* Independent Vector Analysis for Gradient Artifact Removal in Concurrent EEG-fMRI Data. *IEEE Trans. on Biomed. Eng.* **62,** 1750–1758. doi:`10.1109/TBME.2015.2403298` (July 2015).
24. Dimitrova, A. *et al.* Cerebellar Responses Evoked by Nociceptive Leg Withdrawal Reflex as Revealed by Event-Related fMRI. *J. Neurophysiol.* **90,** 1877–1886. doi:`10.1152/jn.00053.2003` (Sept. 2003).

25. MacIntosh, B. J. *et al.* Improving functional magnetic resonance imaging motor studies through simultaneous electromyography recordings. *Hum. Brain Mapp.* **28,** 835–845. doi:`10.1002/hbm.20308` (2007).
26. Iannetti, G. D. *et al.* Simultaneous recording of laser-evoked brain potentials and continuous, high-field functional magnetic resonance imaging in humans. *NeuroImage* **28,** 708–719. doi:`10.1016/j.neuroimage.2005.06.060` (Nov. 15, 2005).
27. Nierhaus, T. *et al.* Internal ventilation system of MR scanners induces specific EEG artifact during simultaneous EEG-fMRI. *NeuroImage* **74,** 70–76. doi:`10.1016/j.neuroimage.2013.02.016` (July 1, 2013).
28. Cifrek, M. *et al.* Surface EMG based muscle fatigue evaluation in biomechanics. *Clin. Biomech.* **24,** 327–340. doi:`10.1016/j.clinbiomech.2009.01.010` (May 1, 2009).
29. Merletti, R., Rainoldi, A. & Farina, D. Surface Electromyography for Noninvasive Characterization of Muscle. *Exerc. Sport Sci. Rev.* **29,** 20–25. doi:`10.1097/00003677-200101000-00005` (Jan. 2001).

Skeletal muscle metabolism assessment: a multimodal approach to understand water dynamics using Magnetization Transfer and muscle activation using Blood Oxygen Level Dependent Signal

8.1 Disclosure

This chapter was written by Alejandro Amador-Tejada with the intention of publishing as an original research paper and is part of a collaboration with Dr. Michael D. Noseworthy. The intended author's order is Alejandro Amador-Tejada, and Dr. Michael D. Noseworthy. The planned publication is awaiting the final submission.

In addition, this chapter will be submitted as an abstract for the *2023 ESMRMB Annual Meeting & Exhibition* from the 04th – 07th October 2023 in Basel, Switzerland.

8.2 Background

After the first report on Magnetization Transfer (MT) was published in 1989 [1], MT has been predominantly used to study the brain (as discussed in Chapter 2.2.3). Nevertheless, during the subsequent decade, MT was used to study other organs, such as the heart, due to the relative insensitivity of MT sequences to motion artifact [2] or in the liver, to enhance the tissue contrast [3]. These applications established MT as a unique way of generating contrast in MRI, with several clinical and research applications [4].

As musculoskeletal disorders increase globally [5], the ability to identify healthy vs. diseased tissue has become a priority. In the MRI field, MT has become a recognized quantitative and non-invasive technique to study the interaction between free and bounded tissue proton pools. MT can be used to identify biomarkers of diseased skeletal muscle in clinical settings. For instance, studies on the skeletal muscle of rabbits have shown high MT contrast [1], which encouraged researchers to study human skeletal muscle by means of this MRI technique. A couple of years after, researchers assessed the feasibility of MT as an indicator between healthy and diseased muscle at lower magnetic fields (< 0.1T) [6] and to measure the exchange range between the free and bounded proton pools [2].

Further studies focused on the change of the MT signal before vs. after exercise. In particular, the MT ratio (MTR) in healthy volunteers performing a knee flexion in the standing position was studied at 0.26T, founding that highly engaged muscles showed higher MTR contrast compared to less engaged muscles, attributed to an increase in the extracellular water content [7]. Additionally, they found a widespread MT signal decrease for all muscles after exercise. These results are supported by another study, where the T_1 and T_2 of skeletal muscle increase after exercise [8]. Another research group looked at the effect of ankle dorsiflexion exercise MT images on ten subjects [9], finding that the ratio $\mathrm{M}_{\mathrm{SAT}}/\mathrm{M}_0$ increased in the TA muscle group after exercise, along with an increase in muscle cross-sectional area, attributed to an increase in the free water content. Likewise, the MTR has been studied in patients with chronic inflammatory demyelinating polyneuropathy (CIDP) [10], finding a decrease in the MTR in CIDP patients compared to healthy controls and a high correlation between MTR and muscle strength.

The research mentioned earlier suggests that there is clinical value in studying skeletal muscle with MT. Nevertheless, these studies faced significant challenges, such as:

- The need to reposition the patient after exercise, which decreased the accuracy of the measurements as there is no standard space for muscle MRI.

- The use of low magnetic fields
- The lack of reproducibility in the exercise performed because the Maximum Voluntary Contraction (MVC) was not standardized across subjects
- The absence of characterization of the exercise, as no other imaging or electrophysiological technique was used to correlate or evaluate the MT images with the exercise performed, leaving little to no information about muscle activation.

Thus, there is an opportunity to study skeletal muscle using MT at higher magnetic fields (*i.e.* = 3T), with the advantages of using an MRI-compatible leg ergometer to standardize exercise load to have comparable results across subjects. In addition, muscle activation can be characterized with a BOLD sequence. Further correlation analysis can be done between the muscle activation information and MT to understand the interaction between the free and bounded water pools and the metabolic dynamics of skeletal muscle. Therefore, this study aimed to assess the MT ratio in healthy volunteers performing a plantar flexion exercise and correlate the MTR with the BOLD response. To the authors' knowledge, no study has attempted to correlate these two MRI techniques to understand the metabolic response, and the free and bounded water pool interactions (from MT) and changes in deoxyhemoglobin concentration (from BOLD) of skeletal muscle.

8.3 Methods

Twelve healthy subjects (11 males, age = 25.7±2.2yr, height = 175±8.9cm, weight = 73.5±11.1kg) were recruited. Experiments were performed accordingly to the MRI general methods (Section 3). The MRI-compatible leg ergometer was used (Chapter 3.3), the MVC of each subject was measured at least 24h prior to scanning to adjust the ergometer weight load (as explained in Chapter 3.3.2).

The protocol consisted of a resting period, an anatomical scan, and the acquisition of a pre-exercise MT scan (described in Sequence C.). Then, subjects performed an exercise block design consisting of 66s rest, followed by 66s isometric plantar-flexion exercise, with a total duration of 8.8min (Fig. 8.1). Finally, a post-exercise MT scan was acquired immediately after the exercise block. Each subject dataset consisted of an MT scan ($\mathrm{M_0}$ and $\mathrm{M_{SAT}}$), and a BOLD scan. Data were preprocessed as follows:

- MT: data preprocessed using the FSL [11–13] and AFNI [14, 15].
    - Spatial co-registration using the pre-exercise MT scan as reference
    - Spatial blurring with a kernel size of 5
    - Computation of the MT ratio for each condition (pre and post-exercise) [4]

$$\mathrm{MTR_{pre/post}} = \frac{\mathrm{M_0^{pre/post}} - \mathrm{M_{SAT}^{pre/post}}}{\mathrm{M_0^{pre/post}}} \tag{8.1}$$

    - Computation of the MT ratio change between conditions (post vs pre) [7]

$$\mathrm{MTR_{comparison}} = \frac{\mathrm{MTR_{post}} - \mathrm{MTR_{pre}}}{\mathrm{MTR_{pre}}} \times 100 \tag{8.2}$$

- BOLD: data preprocessed using the FSL [11–13] and AFNI [14, 15].
    - Crop of first 50 time points in order to allow the signal to arrive at a steady state
    - $\mathrm{B_0}$ correction using an acquired $\mathrm{B_0}$ map
    - Spatial co-registration with the first time point
    - Removal of motion artifact using despiking and outlier detection. Motion artifacts were caused by the transition from rest to exercise and vice-versa

- Spatial blurring with a kernel size of 5
- Band-pass filtering @0.001-1Hz
- BOLD signal deconvolution and correlation computation with a Hemodynamic Response Function (HRF), a square wave of 132s period, with a duty cycle of 66s activation and 66s rest

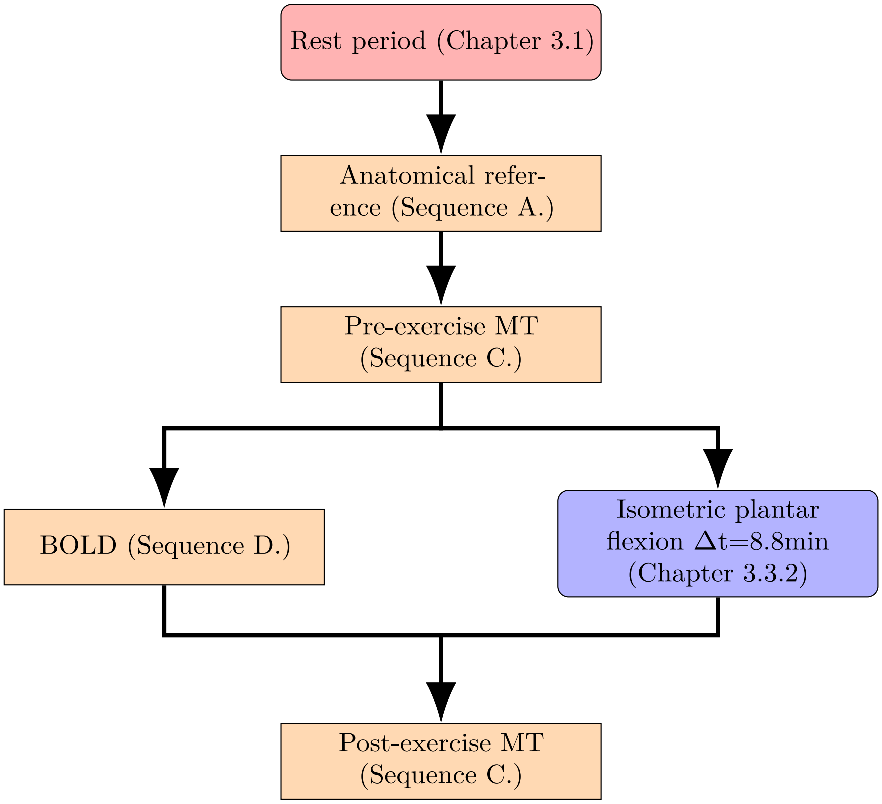

Figure 8.1: Flowchart of the data acquisition protocol. The BOLD and isometric plantar flexion exercise were performed simultaneously. Estimated scanning time: 60min.

Once the MT and BOLD were preprocessed, the final maps (*i.e.* the $\mathrm{MTR}_{\mathrm{comparison}}$ and BOLD correlation) were averaged between the two slices taken and were manually segmented by muscle groups for further statistical comparison. Tissue boundaries and vasculature were avoided during the manual muscle mask segmentation to reflect only muscle activity (Fig. 8.3). In addition, masks were spatially eroded, using the *fslmaths* library from the FSL package, as a conservative measure to decrease the chances of including tissue boundaries, fat septa, or vasculature. As seen in Fig. 2.3, there is a cross-sectional area (CSA) difference between muscle groups (for example, EDL ∼50% CSA TA [16], GM ∼33% CSA SOL, GL ∼12% CSA SOL [17]), which will translate into a sample size difference across muscle groups. Statistical tests such as ANOVA can handle an unbalance in the sample size as long as it is not significant, otherwise, an imposing balance method is required [18]. Therefore, for each muscle group, the statistical maps were randomly subsampled into groups of 10 to 20 samples, followed by an average between these groups. For example, if a muscle group had 45 voxels, then 3 groups of 15 random samples were formed, and they were averaged, yielding 15 samples in total for that muscle group. This method yielded a similar representative sample size across muscle groups.

Muscles in the lower leg can be classified according to their blood supply and innervation in compartments, where the muscles in each operate cooperatively to perform a specific movement. There are three main compartments, each of them focusing on a respective movement [19]:

- Anterior: tibialis anterior (TA), and extensor digitorum longus (EDL). Movement: plantar/dorsiflexion, extend the toes.
- Posterior: tibialis posterior (TP), gastrocnemius medialis (GM), gastrocnemius lateralis (GL) and soleus (SOL). Movement: plantar/dorsiflexion, flex the toes.
- Lateral: peroneus longus (PL). Movement: pronate the foot.

The exercise performed in this experiment was a plantar flexion, where no involvement from the lateral compartment is expected. Therefore, the anterior and posterior compartments were investigated. Therefore only these compartments were selected for the analysis (as shown in Fig. 8.2).

After muscle grouping and segmentation, data were analyzed as follows:

- MT: repeated measurement 3-way ANOVA was performed, assessing the differences in the mean MTR between pre vs. post-exercise, muscle groups and subjects. If significant differences between pre vs post-exercise were found, a 2-way ANOVA was performed testing for differences in the mean $\text{MTR}_{\text{comparison}}$ across muscles and subjects.

- BOLD: correlation maps between the BOLD signal and the HRF were thresholded at a significance level of $p < 0.001$. Negligible correlation values ($| r | < 0.3$) were disregarded as they do not represent significant muscle activation [20]. A 2-way ANOVA was performed, testing the differences in the mean BOLD correlation between muscles and subjects.

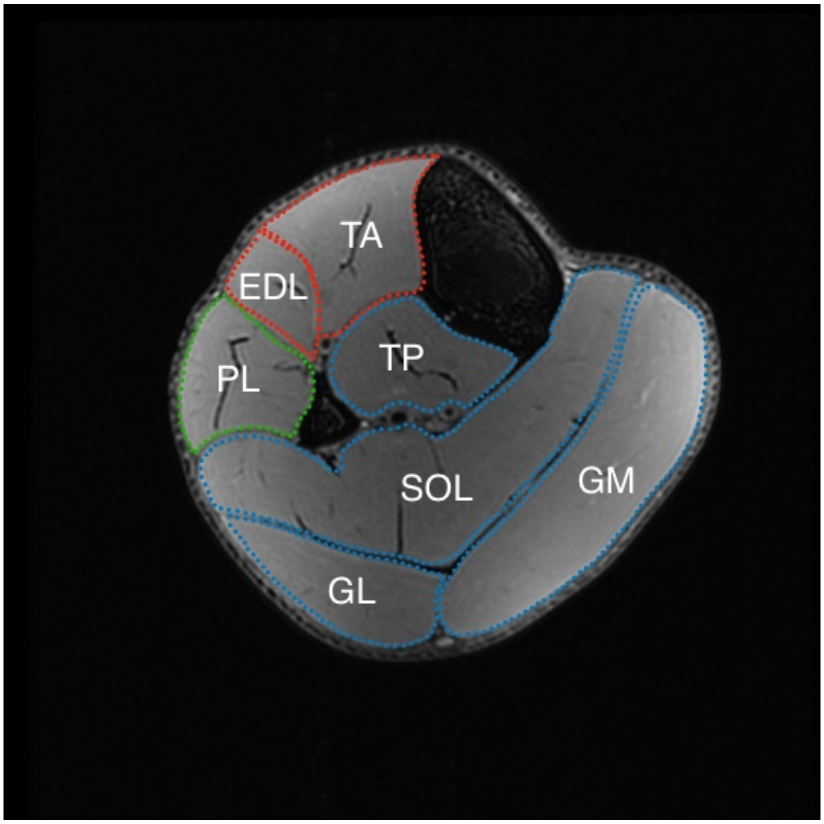

Figure 8.2: Example of muscle group compartments in the lower leg. For the current experiment, muscles were grouped accordingly to their blood supply, innervation and function. (red) Anterior: tibialis anterior (TA), and extensor digitorum longus (EDL). (green) Lateral: peroneus longus (PL). (blue) Posterior: tibialis posterior (TP), gastrocnemius medialis (GM), gastrocnemius lateralis (GL), and soleus (SOL).

8.4 Results

A total of 12 MT, and BOLD were collected. One subject had to be disregarded due to excessive motion during scanning. As described in Chapter 3.3.2, the MVC for each subject was measured at least 24h before the MRI scanning, yielding an average MVC of 15.1 ± 3.9kg. After adjusting the weight loads to the target MVC, the average MVC across subjects was $40.1 \pm 1.1\%$ MVC.

Careful manual muscle segmentation was performed for all muscle groups in both slices (Fig. 8.3), avoiding vasculature and fat septa. As a conservative measure, masks were eroded to decrease the probability of including non-muscle tissue. The muscle segmentation was used to mask the statistical MT and BOLD maps. An example of the preprocessed $\mathrm{MTR}_{\mathrm{comparison}}$ and BOLD maps averaged across both slices are shown in Fig. 8.4. The ideal BOLD response used in the BOLD correlation analysis is shown in Fig. 8.5(yellow). The typical BOLD response to a single stimulus is similar to a Gamma distribution, where there is a dip seconds after the stimuli, then an increase of the signal yielding the BOLD peak, followed by an undershoot phase [21–23]. As the stimulus in this work lasted for more than a minute, a boxcar function was convolved with the Gamma distribution to describe the BOLD signal. The preprocessed maps were prepared for statistical analysis. A box plot showing the distribution of the $\mathrm{MTR}_{\mathrm{comparison}}$ and BOLD correlation for each muscle across subjects is presented in Fig. 8.6 and 8.7.

A repeated measures 3-way ANOVA was performed on the $\mathrm{MTR}_{\mathrm{pre/post}}$, yielding statistical significance in the mean MT ratio across conditions (pre vs post), muscles, and subjects ($p < 0.001$) as shown in Fig. 8.8. The $\mathrm{MTR}_{\mathrm{comparison}}$ mean and standard deviation for each muscle is shown in Fig. 8.9. As for the BOLD correlation analysis, an example of the BOLD time course for a voxel positively and negatively correlated is shown in Fig. 8.5(blue,red). In addition, a 2-way ANOVA was performed on the BOLD correlation, indicating a significant difference in the mean correlation across muscles and subjects ($p < 0.001$) as seen in Fig. 8.10. Similar to the $\mathrm{MTR}_{\mathrm{comparison}}$, the BOLD correlation mean and standard deviation for each muscle are shown in Fig. 8.11.

Until this point, it was confirmed that the mean MT was statistically significant between pre and post-exercise, and both the $\text{MTR}_{\text{comparison}}$ and BOLD correlation were statistically significant between muscles. The final step is to investigate if there is any relationship between these two MRI techniques (MT and BOLD). A linear regression was applied between both metrics, yielding a linear equation model $\overline{\text{BOLD}}_{\text{correlation}} = -0.61 - 0.059\ \overline{\text{MT}}_{\text{comparison}}$ with an R-squared value of 0.62 (Fig. 8.12). Linear regression is used to assess the relationship between two variables, which helps to understand how strong is this relationship, and whether the dependent variable can be predicted using the independent variable. The linear regression was performed using the mean muscle $\text{MTR}_{\text{comparison}}$ as the independent variable and the mean $\text{BOLD}_{\text{correlation}}$ as the dependent variable, yielding a linear model of the form $y = \beta_0 + \beta_1 X$ [24], where y is the predicted value; β_0 is the intercept, *i.e.* the predicted value of y when $x = 0$; and β_1 is the regression coefficient, *i.e.* the slope of the relationship.

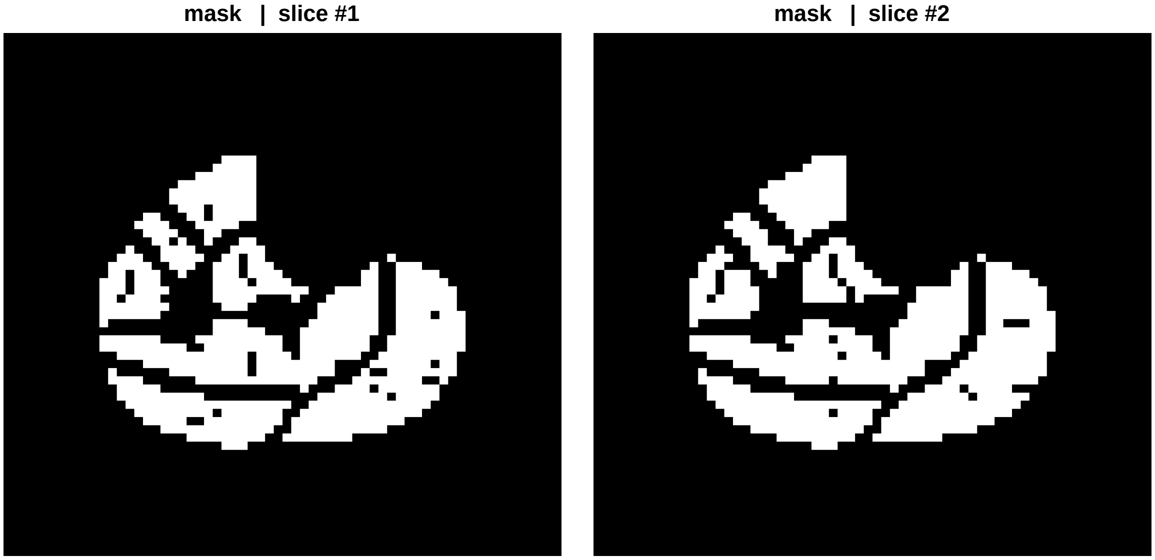

Figure 8.3: Illustration of the manual muscle masks used for the analysis from one of the participants. Each muscle group mask was built using the anatomical scan as a reference. Masks were carefully drawn to avoid vasculature, fat septa and tissue boundaries. In addition, masks were eroded before the multiplication with the MT and BOLD maps.

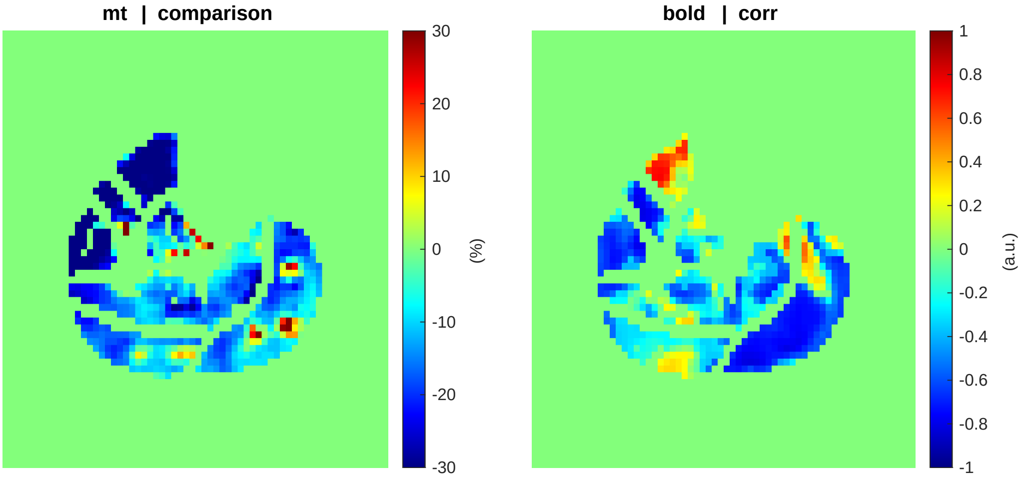

Figure 8.4: Example of the final preprocessed $\text{MTR}_{\text{comparison}}$ (left) and BOLD correlation (right) maps. The final maps were averaged between both slices. For the $\text{MTR}_{\text{comparison}}$, looking at Eqn. 8.2, it can be seen that the range of the pixel value is expected to be within [-100,100]%, but to enhance the contrast, the dynamic range of the plot was adjusted to [-30,30]%. Meanwhile, the BOLD correlation pixel value is expected within [-1,1](a.u.). A general trend is seen in the $\text{MTR}_{\text{comparison}}$, as all muscle shows dominantly negative values, which indicates a decrease in the MTR_{post} compared to the MTR_{pre}. The TA showed a positive correlation for the BOLD correlation, while the other muscles showed a largely negative correlation with the exercise performed.

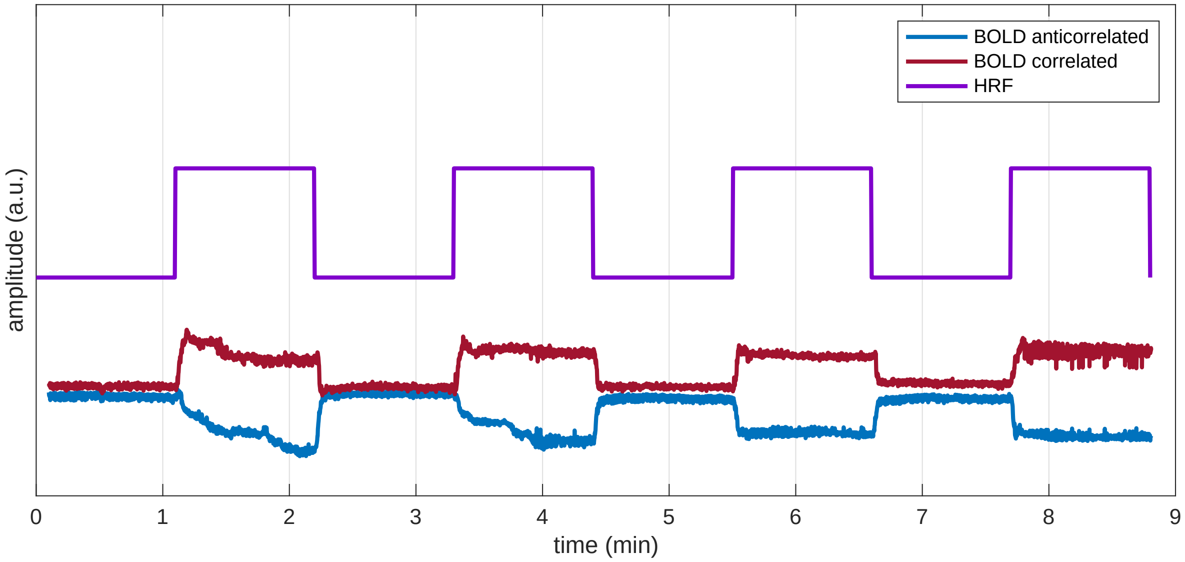

Figure 8.5: Plot showing (yellow) the HRF used for the BOLD correlation analysis. (blue, red) an example of the BOLD time course for a voxel positively and negatively correlated. An offset was added to the BOLD signal sample and the HRF for illustrative purposes.

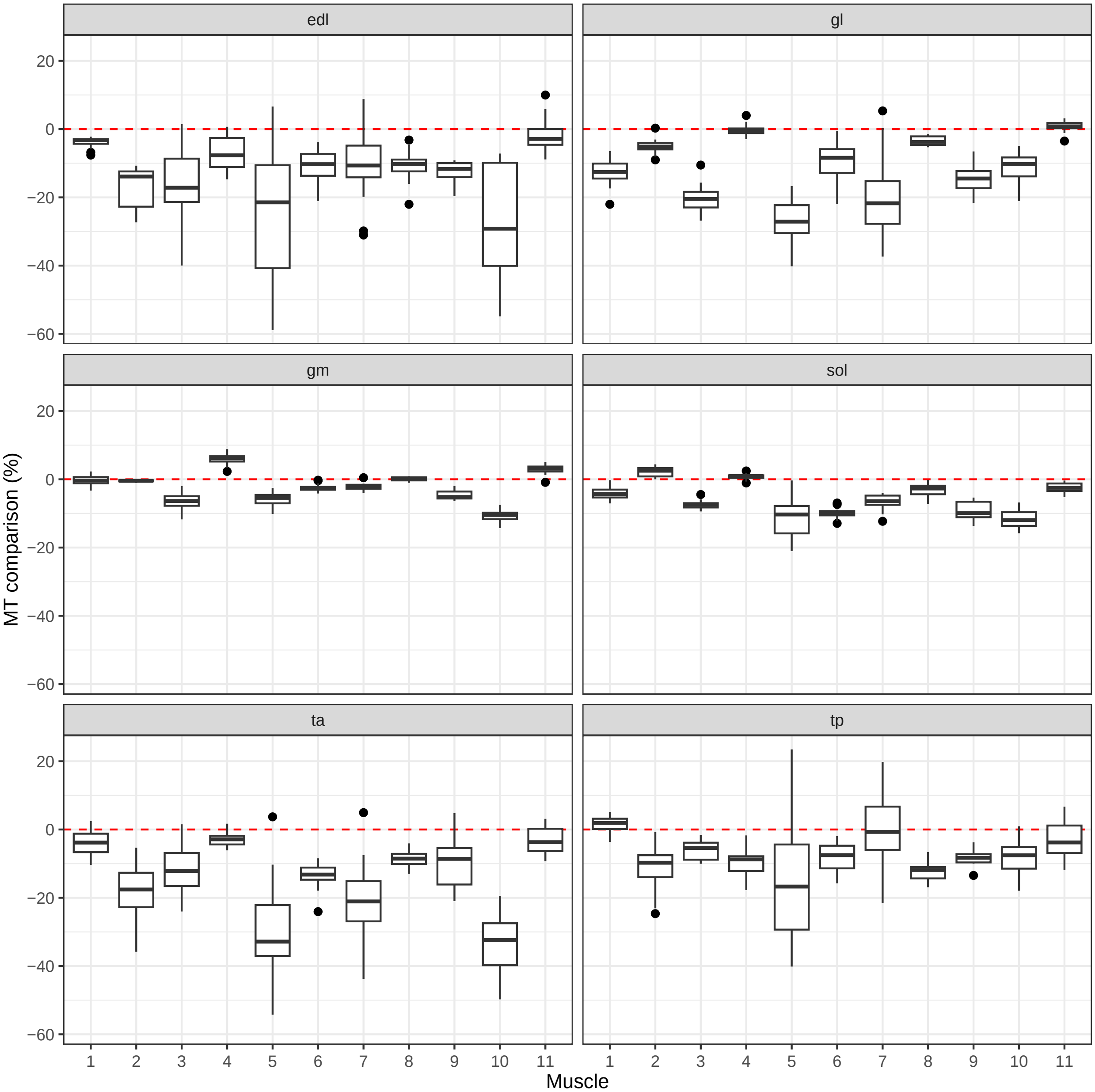

Figure 8.6: Exploratory box plot of the $\text{MTR}_{\text{comparison}}$ for each muscle (each square represents one) for each subject. The horizontal red dashed line represents no change between the MTR_{post} and MTR_{pre}. As an initial observation, it is seen that there is a trend in the $\text{MTR}_{\text{comparison}}$ for all muscles, where the $\text{MTR}_{\text{comparison}}$ is negative, meaning that there was a decrease in the MTRpost compared to the MTR_{pre}.

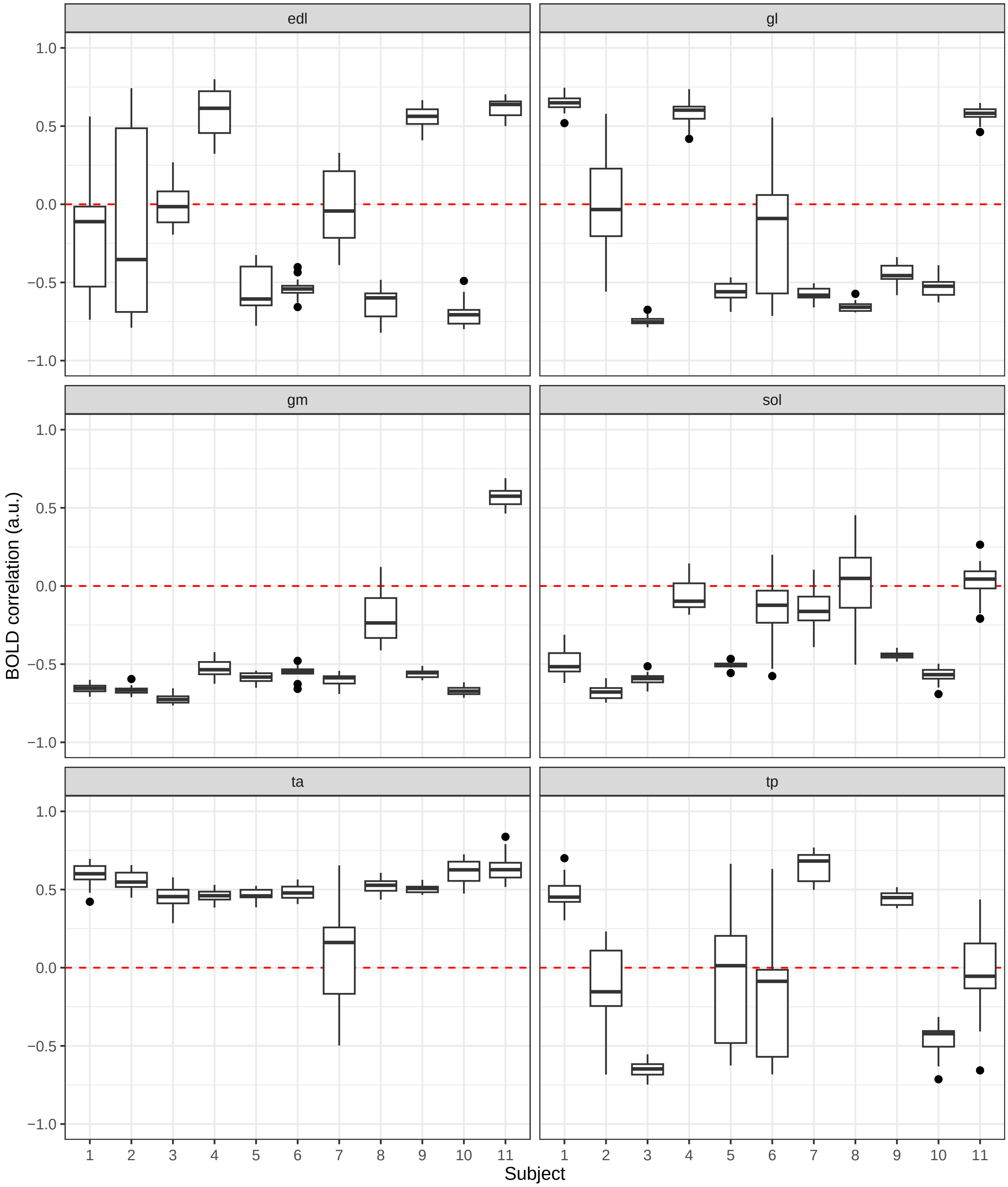

Figure 8.7: Exploratory box plot of the BOLD correlation for each muscle (each square represents one) for each subject. The horizontal red dashed line represents no correlation between the ideal and hemodynamic responses. As a preliminary remark, it is observed that GM and SOL muscles had a general negative correlation trend except for participant #11. In contrast, TA had a positive correlation trend for all subjects except for participant # 7. Meanwhile, GL TP and EDL muscles showed mixed correlation values.

```
## Type III Analysis of Variance Table
##                   Sum Sq Mean Sq DF F value    Pr(>F)    
## condition         391.17  391.17  1 301.337 < 2.2e-16 ***
## muscle            286.74   57.35  5  44.177 < 2.2e-16 ***
## subject           317.29   31.73 10  24.442 6.005e-16 ***
## condition:muscle   67.44   13.49  5  10.390 6.972e-10 ***
## ---
## Signif. codes:  0 '***' 0.001 '**' 0.01 '*' 0.05 '.' 0.1 ' ' 1
```

Figure 8.8: MT repeated measures 3-way ANOVA results. The model included the condition (pre vs. post), muscle groups (Fig. 8.2), and subjects (n = 11). In addition, the interaction between conditions and muscles was included in the model. Results show statistical significance in the mean MT between $\mathrm{MTR}_{\mathrm{pre}}$ and $\mathrm{MTR}_{\mathrm{post}}$ ($p < 2.2 \times 10^{-16}$), muscles ($p < 2.2 \times 10^{-16}$), subjects ($p = 6.005 \times 10^{-16}$) and between the condition and muscle interaction ($p = 6.972 \times 10^{-10}$).

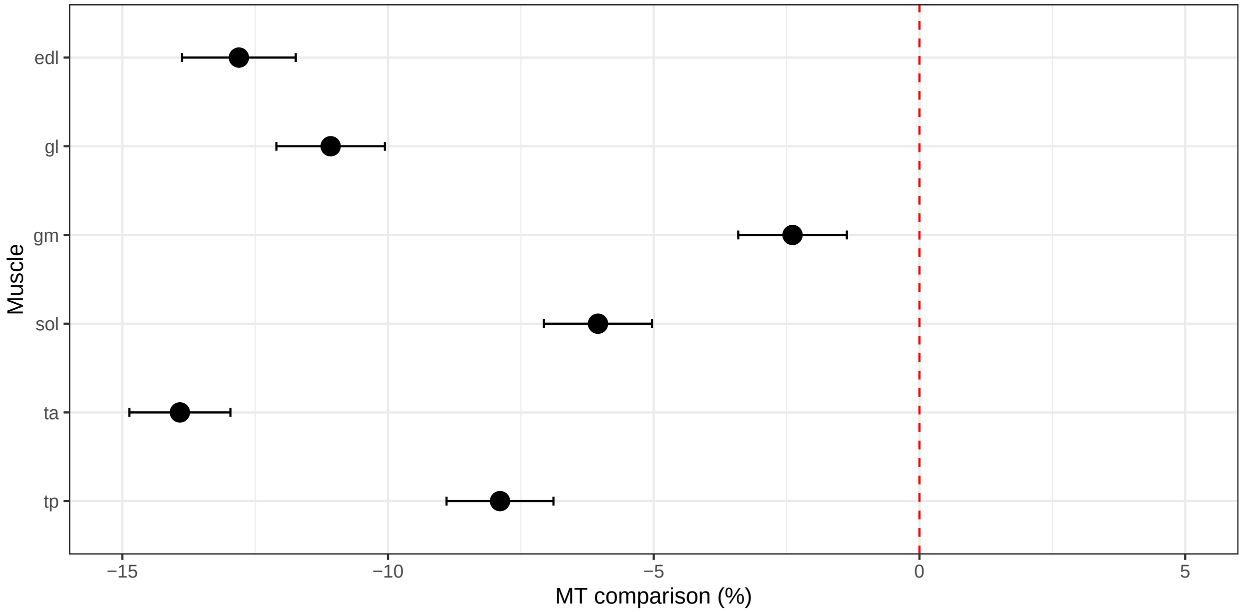

Figure 8.9: Plot showing the estimated mean and confidence intervals for the $\mathrm{MTR}_{\mathrm{comparison}}$ maps for each muscle. TA $(-13.92, [-14.87, -12.97])$ showed the highest change, followed by EDL $(-12.81, [-13.88, -11.74])$, GL $(-11.08, [-12.1, -10.06])$, TP $(-7.89, [-8.9, -6.89])$, SOL $(-6.05, [-7.07, -5.03])$ and lastly GM $(-2.39, [-3.41, -1.37])$ muscle group. The vertical red dashed line represents no change between $\mathrm{MTR}_{\mathrm{post}}$ and $\mathrm{MTR}_{\mathrm{pre}}$.

```
## Type III Analysis of Variance Table
##                   Sum Sq Mean Sq DF F value    Pr(>F)
## muscle            104.75  20.950  5  167.94 < 2.2e-16 ***
## subject            74.54   7.454 10   59.75 < 2.2e-16 ***
## ---
## Signif. codes:  0 '***' 0.001 '**' 0.01 '*' 0.05 '.' 0.1 ' ' 1
```

Figure 8.10: BOLD 2-way ANOVA results. The model included the muscle groups (Fig. 8.2) and subjects (n = 11). Results show statistical significance in the mean BOLD correlation between muscles and subjects ($p < 2.2 \times 10^{-16}$).

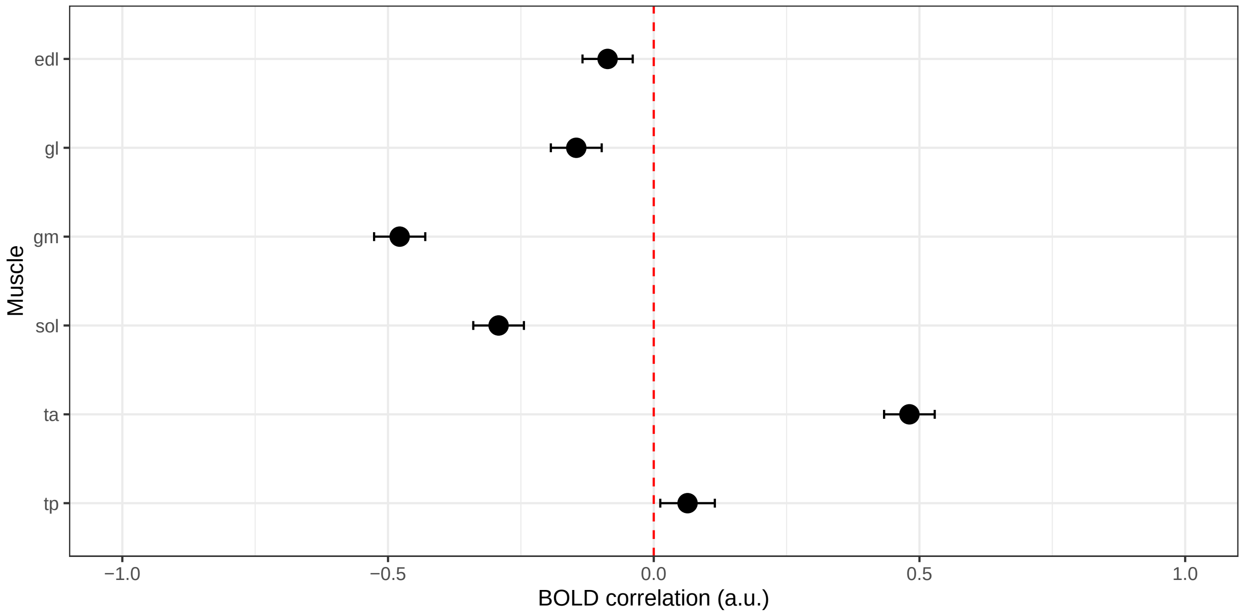

Figure 8.11: Plot showing the estimated mean and confidence intervals for the BOLD correlation maps for each muscle. TA ($0.48, [0.43, 0.53]$) showed the highest positive correlation, followed by TP ($0.06, [0.01, 0.11]$), EDL ($-0.09, [-0.13, -0.04]$), GL ($-0.15, [-0.19, -0.1]$), SOL ($-0.29, [-0.34, -0.24]$) and lastly GM ($-0.48, [-0.53, -0.43]$) muscle group. The vertical red dashed line represents no correlation between the ideal and hemodynamic responses.

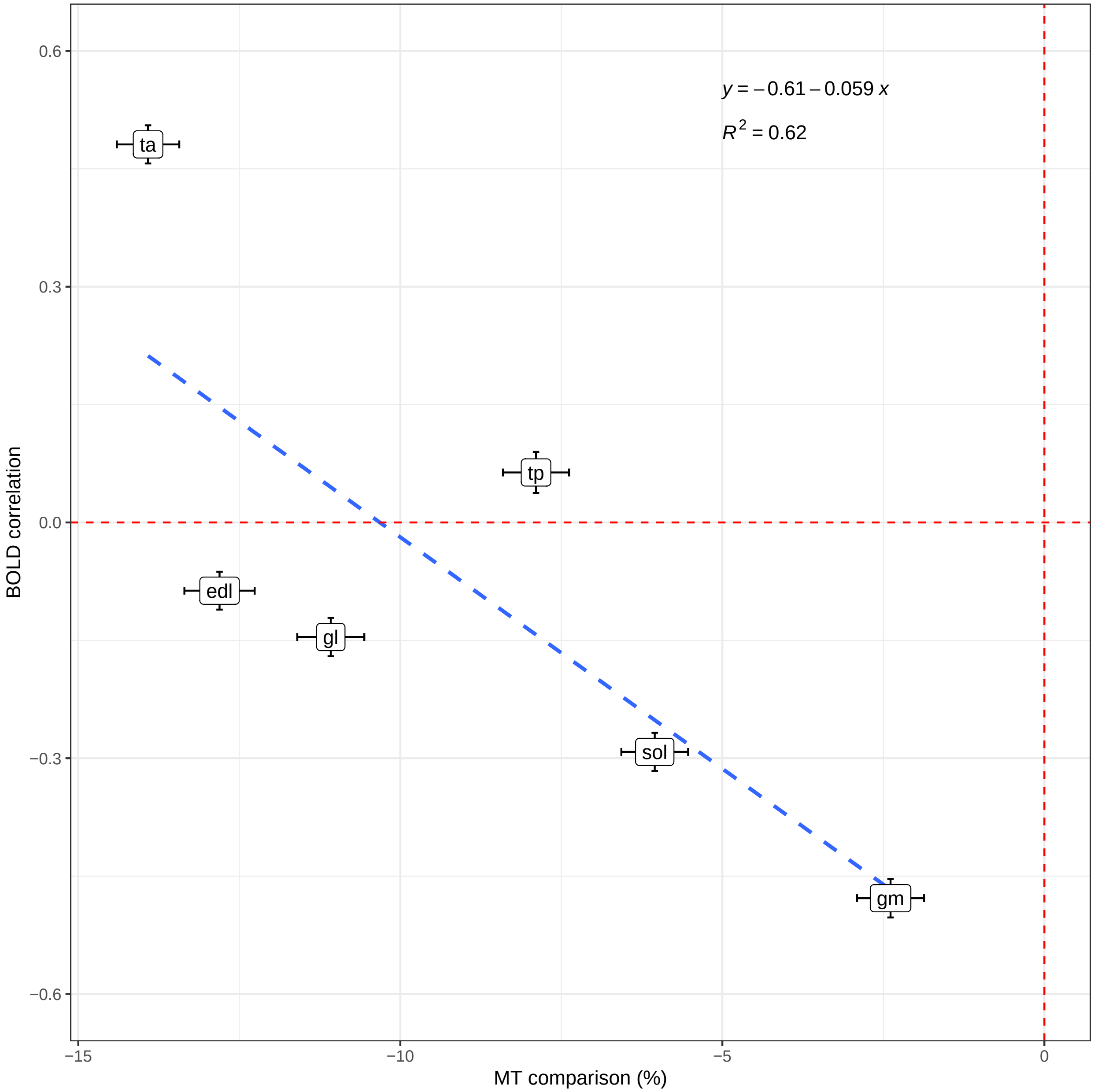

Figure 8.12: Plot showing the linear relationship between the $\text{MTR}_{\text{comparison}}$ and BOLD correlation estimated means along with their standard error. The $\text{MTR}_{\text{comparison}}$ is shown on the x-axis, while the BOLD correlation is on the y-axis. The linear relationship found is $\overline{\text{BOLD}}_{\text{correlation}} = -0.61 - 0.059\ \overline{\text{MTR}}_{\text{comparison}}$ with an R-squared value of 0.62.

8.5 Discussion

This study aimed to explore the possibility of using MT to study muscle metabolism. One of the fundamental steps of this research study was to ensure the isometric plantar flexion exercise was standardized across subjects so that all volunteers executed the same percentage of effort to perform the exercise. The target MVC was 40%, but after adjusting the weight loads, the average MVC was $40.1 \pm 1.1\%$. Previous studies have shown that muscle fatigue can occur depending on the MVC percentage, the target muscle groups and the exercise protocol parameters, such as the duration. For instance, isometric plantar flexion at 100% MVC with 1s contraction/rest and 100 repetitions showed muscle fatigue [25]. Another study with lower MVC (40%) showed muscle fatigue during a sustained isometric contraction after 4min [26]. Using these studies as a reference, no significant muscle fatigue was expected during the current exercise protocol, as theoretically, fiber type I is being recruited (Tbl. 2.1).

The exercise performed was an isometric plantar flexion exercise, where the muscles expected to be more engaged are the TA, the GM and GL muscle groups. By means of visual examination, it can be seen that the final $\mathrm{MTR}_{\mathrm{comparison}}$ map sample (Fig. 8.4, left) showed a negative change trend for all muscles, *i.e.* $\mathrm{MTR}_{\mathrm{post}} < \mathrm{MTR}_{\mathrm{pre}}$. The TA muscle showed the highest change, followed by EDL. Mild changes were observed for TP, SOL, GM and GL. Looking at the final BOLD correlation map sample, it is seen that the TA muscle showed a positive correlation with the HRF. In contrast, EDL and GM showed the highest negative correlation, followed by GM and SOL muscles (Fig. 8.4, right).

The exploratory box plots revealed similar trends to the ones observed in Fig. 8.4 across subjects. The mean $\mathrm{MTR}_{\mathrm{comparison}}$ was negative for all participants for the TA and EDL muscle. Meanwhile, the rest of the muscle groups (GL, GM, SOL and TP) showed a similar negative trend, but certain participants did not follow the pattern (Fig. 8.6). This behaviour was also seen in the BOLD correlation maps, where TA was positively correlated for all subjects. On the contrary, GM and SOL showed a negative correlation trend except for volunteer #11. The rest of the muscle groups had mixed correlation values across subjects (Fig. 8.7).

The first step to understanding the global picture of the experiment was to assess if there were any differences in the mean MTR between pre vs post-exercise. When looking at the ANOVA test performed 8.8, it is observed that there is a significant difference between conditions ($p < 0.001$). Further analysis on the $\mathrm{MTR}_{\mathrm{comparison}}$ yielded the estimated means and confidence intervals for each muscle (Fig. 8.9). To understand the meaning of this measurement, it is necessary to look at Eqn. 8.2, where there are three cases:

$$\mathrm{MTR}_{\mathrm{comparison}} = \begin{cases} < 0, & \Rightarrow \mathrm{MTR}_{\mathrm{post}} < \mathrm{MTR}_{\mathrm{pre}} \\ > 0, & \Rightarrow \mathrm{MTR}_{\mathrm{post}} > \mathrm{MTR}_{\mathrm{pre}} \\ = 0, & \Rightarrow \mathrm{MTR}_{\mathrm{post}} = \mathrm{MTR}_{\mathrm{pre}} \end{cases} \tag{8.3}$$

It is seen for all muscle groups that $\mathrm{MTR}_{\mathrm{comparison}} < 0$, which implies that $\mathrm{MTR}_{\mathrm{post}} < \mathrm{MTR}_{\mathrm{pre}}$. Recalling the equation for the MT ratio, which demonstrates the signal difference between the free and bounded water pools (Eqn. 8.4), it is possible to investigate the meaning of $\mathrm{MTR}_{\mathrm{comparison}}$ being negative. The interaction between the free and bounded water pools is complex, as there are changes in water concentration, pool exchange rates, and metabolism [4]. Studies have shown that post-exercised skeletal muscle exhibits an increase in its transverse relaxation time (T_2) compared to inactive muscle, suggesting a local increase in the water content [8, 27, 28]. When the off-resonance pulse is not applied, the principal signal contributor is the free water pool, *i.e.* M_0. If the total water content increases after exercise, then $\mathrm{M}_0^{\mathrm{pre}} < \mathrm{M}_0^{\mathrm{post}}$. This suggests that the observed negative $\mathrm{MTR}_{\mathrm{comparison}}$ is due to differences in the $\mathrm{M}_{\mathrm{SAT}}^{\mathrm{pre}}$ and $\mathrm{M}_{\mathrm{SAT}}^{\mathrm{post}}$. Because the exchange rate is bidirectional *i.e.* free to the bounded pool and vice versa (Eqn. 8.5), no deduction can be made as to where these changes are coming from. A hypothesis could be that the exchange rate slows down, decreasing the portion of saturated protons in the free water pool.

$$\mathrm{MTR} = \frac{\mathrm{M}_0 - \mathrm{M}_{\mathrm{SAT}}}{\mathrm{M}_0} \tag{8.4}$$

Water is a molecule highly involved in muscle metabolism, specifically during aerobic ATP resynthesis and in ATP metabolism (Tbl. 2.2). The low intensity, 40% MVC plantar flexion exercise performed is assumed to be aerobic exercise, which involves using O_2. On the other hand, as seen in Chapter 2.2.2, an increase in muscle metabolic activity is associated with an increase in the blood oxygenation (oxy-Hb) and hence an increase in the BOLD signal. This makes muscle BOLD an ideal technique to correlate and validate the MT analysis.

$$^{1}\mathrm{H_b} \underset{\text{saturated}}{\overset{\text{unsaturated}}{\rightleftharpoons}} {}^{1}\mathrm{H_f} \tag{8.5}$$

Muscle BOLD was investigated by means of a correlation analysis between the BOLD signal with an HRF (Fig. 8.5:blue,red). The HRF is the exercise protocol itself: a value of -1 indicates rest, while a value of 1 is exercise. A positive correlation value means the ideal function and the BOLD response are aligned, *i.e.* the muscle is metabolically active during exercise compared to baseline. On the other hand, a negative correlation value means the ideal function and the BOLD response are dephased 180°. A negative BOLD signal (compared to baseline) might be counterintuitive because it would suggest a muscle 'deactivation'. Negative BOLD response (NBR) has been a matter of interest in the research community [29–32], being a topic still in debate due to the complexity of the BOLD contrast. Literature suggests that NBR arises from local 'deactivation', or a decrease in blood flow (named 'vascular steal') [30]. For instance, in the brain visual cortex, NBR was associated with a decrease in blood flow and oxygen consumption [33, 34]. In skeletal muscle, NBR has also been associated with a decrease in the oxygenation of muscle tissue [35]. For the current exercise protocol, the TA muscle group showed a positive correlation, while the rest of the muscles showed a negative correlation trend (as seen in Fig. 8.4, right). A 2-way ANOVA was used to test for the differences in the mean correlation value across muscle and subjects, yielding statistical differences for both factors ($p < 0.001$) as seen in Fig. 8.10. Further analysis on the $\mathrm{BOLD_{correlation}}$ yielded the estimated means and confidence intervals for each muscle (Fig. 8.11). It is observed that TA and TP had a positive correlation, meanwhile EDL, GL, GM and SOL muscle groups have a negative correlation.

Integrating the findings from MT and BOLD, it is seen that TA had the highest positive $\mathrm{BOLD_{correlation}}$ (indicating the muscle was metabolically active during exercise) and the greatest change in the $\mathrm{MT_{comparison}}$ (suggesting there are changes in the exchange rates between the free and bounded water pools pre vs post-exercise). Following this idea, on the other side are GM and SOL muscles, which showed the highest negative $\mathrm{BOLD}_{\mathrm{correlation}}$ and the lowest change in the $\mathrm{MT}_{\mathrm{comparison}}$. This indicates that these muscles had a decrease in blood flow, which followed an increase in deoxygenation (from $\mathrm{BOLD}_{\mathrm{correlation}}$). At the same time, they showed inferior changes in the water pool exchange rate (from $\mathrm{MT}_{\mathrm{comparison}}$). Negligible estimated correlation values ($|\, r \,| < 0.3$), either positive (TP) or negative (EDL and GL), showed intermediate $\mathrm{MT}_{\mathrm{comparison}}$ values (Fig. 8.12). The results shown by these muscles could be explained by picturing a 'transition zone', where changes in water dynamics, blood flow, and metabolism are rearranged to support the highly active TA muscle group. The linear regression found between these two techniques is shown in Eqn. 8.6, with and R-squared value of 0.62.

$$\overline{\mathrm{BOLD}}_{\mathrm{correlation}} = -0.61 - 0.059\ \overline{\mathrm{MTR}}_{\mathrm{comparison}} \tag{8.6}$$

In conclusion, the current pilot study showed a correlation between the MT and BOLD techniques in healthy skeletal muscle during an exercise protocol. One of the principal advantages of this study is the use of a relatively short MT sequence (∼1min), which decreases the chances of introducing motion artifacts during scanning. Even more, the short duration of this sequence also reduced the averaging over time effects, decreasing the chances of skeletal muscle returning to its baseline state after exercise. This is advantageous compared to other sequences, such as T_2 mapping, where the increased scanning time could complicate detecting fast changes in exercised skeletal muscle. Water is the main component in skeletal muscle, accounting for almost 76% of its total mass [36–38]. Naturally, the ability to understand the water characteristics and dynamics of skeletal muscle is essential as it could help to classify healthy vs diseased muscle. For example, inflammatory diseases or muscle infarction (an unusual complication of diabetic patients [39, 40]) typically presents muscle inflammation which could be detected with MT. Metabolic diseases that block the normal metabolic pathways and cause an accumulation of abnormal chemicals within the tissue [41] could change the interaction between the free and bounded water pools, and MT scans could detect this. Even more, the clear differences between muscle groups and the correlation from both MT and BOLD could enhance the evaluation and discrimination of muscle recruitment during exercise. Further research is required to understand the exchange rate dynamics *i.e.* between the free and bounded pools in both directions for MT during exercise in healthy skeletal muscle. Another research opportunity would be acquiring multichannel EMG recordings from different muscle groups to compare the electrical activity between muscles and correlate them to MT and BOLD.

Limitations

The following points are considered to be limitations of the current research:

- The MT scans were taken pre and post-exercise. Although this helps to reduce motion artifacts, it does not give the whole picture of the interaction between the free and bounded water pools. In the future, it would be interesting to study the dynamics of MT during the exercise protocol. To accomplish this, either a special MT sequence acquiring multiple time points or several concatenated MT scans would be required.
- The current MT sequence used provides only part of the whole phenomena, *i.e.* there is only information about the water peak without an RF saturation pulse (M_0) and with an RF saturation pulse (M_{SAT}). There are no details regarding the exchange rates (Eqn. 8.5), or the effects of dipolar coupling, if any.
- It has been shown that intensive exercise could increase the concentration of other solutes in muscle (such as lactate) that could interact with the water pools [9]. Although the exercise protocol performed in this study was not ranked as intensive, further research needs to be done to understand the effects of the type of exercise on the relationship between MT and BOLD.

References

1. Wolff, S. D. & Balaban, R. S. Magnetization transfer contrast (MTC) and tissue water proton relaxation in vivo. *Magn. Reson. Med.* **10,** 135–144. doi:`10.1002/mrm.1910100113` (1989).
2. Komu, M. Analysis of longitudinal relaxation rate constants from magnetization transfer MR images of human tissues at 0.1 T. *Magn. Reson. Imaging* **10,** 35–40. doi:`10.1016/0730-725X(92)90370-F` (Jan. 1, 1992).
3. Kahn, C. E. *et al.* Magnetization transfer imaging of the abdomen at 0.1 T: Detection of hepatic neoplasms. *Magn. Reson. Imaging* **11,** 67–71. doi:`10.1016/0730-725X(93)90413-8` (Jan. 1, 1993).
4. Henkelman, R. M., Stanisz, G. J. & Graham, S. J. Magnetization transfer in MRI: a review. *NMR Biomed.* **14,** 57–64. doi:`10.1002/nbm.683` (2001).
5. Jin, Z. *et al.* Incidence trend of five common musculoskeletal disorders from 1990 to 2017 at the global, regional and national level: results from the global burden of disease study 2017. *Ann. Rheum. Dis.* **79,** 1014–1022. doi:`10.1136/annrheumdis-2020-217050` (Aug. 2020).
6. Swallow, C. E. *et al.* Magnetization transfer contrast imaging of the human leg at 0.1 T: A preliminary study. *Magn. Reson. Imaging* **10,** 361–364. doi:`10.1016/0730-725X(92)90506-U` (Jan. 1, 1992).
7. Zhu, X. P., Zhao, S. & Isherwood, I. Magnetization transfer contrast (MTC) imaging of skeletal muscle at 0.26 Tesla — changes in signal intensity following exercise. *The Br. J. Radiol.* **65,** 39–43. doi:`10.1259/0007-1285-65-769-39` (Jan. 1992).
8. Fleckenstein, J. L. *et al.* Acute effects of exercise on MR imaging of skeletal muscle in normal volunteers. *Am. J. Roentgenol.* **151,** 231–237. doi:`10.2214/ajr.151.2.231` (1988).
9. Yoshioka, H. *et al.* Acute change of exercised muscle using magnetization transfer contrast MR imaging. *Magn. Reson. Imaging* **12,** 991–997. doi:`10.1016/0730-725X(94)91229-P` (Jan. 1, 1994).
10. Sinclair, C. *et al.* *Correlation between muscle magnetization transfer ratio and muscle strength in chronic inflammatory demyelinating polyneuropathy* in. Proceedings of the 17th Annual Meeting of ISMRM, Honolulu, Hawaii, USA (2009), 3958.
11. Jenkinson, M. *et al.* FSL. *NeuroImage. 20 YEARS OF fMRI* **62,** 782–790. doi:`10.1016/j.neuroimage.2011.09.015` (Aug. 15, 2012).
12. Smith, S. M. *et al.* Advances in functional and structural MR image analysis and implementation as FSL. *NeuroImage. Mathematics in Brain Imaging* **23,** S208–S219. doi:`10.1016/j.neuroimage.2004.07.051` (Jan. 1, 2004).
13. Woolrich, M. W. *et al.* Bayesian analysis of neuroimaging data in FSL. *NeuroImage. Mathematics in Brain Imaging* **45,** S173–S186. doi:`10.1016/j.neuroimage.2008.10.055` (Mar. 1, 2009).
14. Cox, R. W. AFNI: Software for Analysis and Visualization of Functional Magnetic Resonance Neuroimages. *Comput. Biomed. Res.* **29,** 162–173. doi:`10.1006/cbmr.1996.0014` (June 1, 1996).
15. Cox, R. W. & Hyde, J. S. Software tools for analysis and visualization of fMRI data. *NMR Biomed.* **10,** 171–178. doi:`10.1002/(SICI)1099-1492(199706/08)10:4/5<171::AID-NBM453>3.0.CO;2-L` (1997).
16. Sponbeck, J. K. *et al.* Leg muscle cross-sectional area measured by ultrasound is highly correlated with MRI. *J. Foot Ankle Res.* **14,** 5. doi:`10.1186/s13047-021-00446-y` (Jan. 12, 2021).
17. Fukunaga, T. *et al.* Physiological cross-sectional area of human leg muscles based on magnetic resonance imaging. *J. Orthop. Res.* **10,** 926–934. doi:`10.1002/jor.1100100623` (1992).
18. Shaw, R. G. & Mitchell-Olds, T. Anova for Unbalanced Data: An Overview. *Ecology* **74,** 1638–1645. doi:`10.2307/1939922` (1993).
19. Azam, M., Wehrle, C. J. & Shaw, P. M. in *StatPearls* (StatPearls Publishing, Treasure Island (FL), 2022).
20. Mukaka, M. M. A guide to appropriate use of Correlation coefficient in medical research. *Malawi Med. J.* **24,** 69–71. doi:`10.4314/mmj.v24i3` (2012).
21. Amaro, E. & Barker, G. J. Study design in fMRI: Basic principles. *Brain Cogn.* **60,** 220–232. doi:`10.1016/j.bandc.2005.11.009` (Apr. 1, 2006).
22. Jacobi, B. *et al.* Skeletal muscle BOLD MRI: From underlying physiological concepts to its usefulness in clinical conditions. *J. Magn. Reson. Imaging* **35,** 1253–1265. doi:`10/gqcfz4` (2012).
23. McGillivray, J. E. *et al.* The Effect of Exercise on Neural Activation and Cognition: A Review of Task-Based fMRI Studies. *Crit. Rev. Biomed. Eng.* **49.** doi:`10.1615/CritRevBiomedEng.2021038975` (2021).

24. Vittinghoff, E. *et al. Regression Methods in Biostatistics: Linear, Logistic, Survival, and Repeated Measures Models* doi:`10.1007/978-1-4614-1353-0` (Springer US, Boston, MA, 2012).
25. Kawakami, Y. *et al.* Fatigue responses of human triceps surae muscles during repetitive maximal isometric contractions. *J. Appl. Physiol.* **88,** 1969–1975. doi:`10.1152/jappl.2000.88.6.1969` (June 2000).
26. Mademli, L. & Arampatzis, A. Behaviour of the human gastrocnemius muscle architecture during submaximal isometric fatigue. *Eur. J. Appl. Physiol.* **94,** 611–617. doi:`10.1007/s00421-005-1366-8` (Aug. 1, 2005).
27. Nygren, A. T. & Kaijser, L. Water exchange induced by unilateral exercise in active and inactive skeletal muscles. *J. Appl. Physiol.* **93,** 1716–1722. doi:`10.1152/japplphysiol.01117.2001` (Nov. 2002).
28. Ploutz-Snyder, L. L. *et al.* Different effects of exercise and edema on T2 relaxation in skeletal muscle. *Magn. Reson. Med.* **37,** 676–682. doi:`10.1002/mrm.1910370509` (1997).
29. Jorge, J. *et al.* Mapping and characterization of positive and negative BOLD responses to visual stimulation in multiple brain regions at 7T. *Hum. Brain Mapp.* **39,** 2426–2441. doi:`10.1002/hbm.24012` (2018).
30. Nakata, H. *et al.* Negative BOLD responses during hand and foot movements: An fMRI study. *PLOS ONE* **14,** e0215736. doi:`10.1371/journal.pone.0215736` (Apr. 19, 2019).
31. Mullinger, K. J. *et al.* Evidence that the negative BOLD response is neuronal in origin: A simultaneous EEG–BOLD–CBF study in humans. *NeuroImage* **94,** 263–274. doi:`10.1016/j.neuroimage.2014.02.029` (July 1, 2014).
32. Wade, A. R. The Negative BOLD Signal Unmasked. *Neuron* **36,** 993–995. doi:`10.1016/S0896-6273(02)01138-8` (Dec. 19, 2002).
33. Pasley, B. N., Inglis, B. A. & Freeman, R. D. Analysis of oxygen metabolism implies a neural origin for the negative BOLD response in human visual cortex. *NeuroImage* **36,** 269–276. doi:`10.1016/j.neuroimage.2006.09.015` (June 1, 2007).
34. Shmuel, A. *et al.* Sustained Negative BOLD, Blood Flow and Oxygen Consumption Response and Its Coupling to the Positive Response in the Human Brain. *Neuron* **36,** 1195–1210. doi:`10.1016/S0896-6273(02)01061-9` (Dec. 19, 2002).
35. Muller, M. D. *et al.* Muscle oxygenation during dynamic plantar flexion exercise: combining BOLD MRI with traditional physiological measurements. *Physiol. Reports* **4,** e13004. doi:`10.14814/phy2.13004` (2016).
36. Yamada, Y. *et al.* Extracellular Water May Mask Actual Muscle Atrophy During Aging. *The Journals Gerontol. Ser. A* **65A,** 510–516. doi:`10.1093/gerona/glq001` (May 1, 2010).
37. Yamada, Y. *et al.* The Extracellular to Intracellular Water Ratio in Upper Legs is Negatively Associated With Skeletal Muscle Strength and Gait Speed in Older People. *The Journals Gerontol. Ser. A* **72,** 293–298. doi:`10.1093/gerona/glw125` (Mar. 1, 2017).
38. Lorenzo, I., Serra-Prat, M. & Yébenes, J. C. The Role of Water Homeostasis in Muscle Function and Frailty: A Review. *Nutrients* **11,** 1857. doi:`10.3390/nu11081857` (Aug. 2019).
39. Umpierrez, G. E. *et al.* Diabetic muscle infarction. *The Am. J. Med.* **101,** 245–250. doi:`10.1016/S0002-9343(96)00156-8` (Sept. 1, 1996).
40. Bjornskov, E. K. *et al.* Diabetic muscle infarction: A new perspective on pathogenesis and management. *Neuromuscul. Disord.* **5,** 39–45. doi:`10.1016/0960-8966(94)E0027-6` (Jan. 1, 1995).
41. Olsen, N. J., Qi, J. & Park, J. H. Imaging and skeletal muscle disease. *Curr. Rheumatol. Reports* **7,** 106–114. doi:`10.1007/s11926-005-0062-3` (Apr. 1, 2005).

Discussion

9.1 Unifying research chapters

The primary outlook of this thesis was to understand muscle metabolism and function using non-invasive imaging. As described above, this involved using MRI with unique image acquisition and analysis techniques. This was done in an effort to improve the available techniques for muscle imaging to assist in disease and disorder diagnosis. Additionally, experimental paradigms of rest, muscle stimulation (involuntary contraction) and muscle flexion were tested as different clinical populations have varying movement abilities. The research chapters presented in this work followed a sequential train of thoughts that continually changed as the results of each chapter were obtained.

The first idea was using ^{1}H-MRS to study skeletal muscle metabolism during exercise. After four months of MRI training to have level 3 (which allowed using the MRI system without supervision, only scanning other graduate students with accredited MRI safety training), several ^{1}H-MRS scans were taken to familiarize with the technique. On two occasions, the volunteer entered the scanner, and two ^{1}H-MRS scans were taken (one after the other, same parameters and prescan values). However, when looking at the scans, the spectra were not similar (results not shown in this work). This prompted the first question: are ^{1}H-MRS experiments reproducible within and across scanning sessions? This is an important aspect to investigate, as the lack of reproducibility would difficult the use of this technique in this thesis. This question led to the first research chapter Skeletal muscle proton spectroscopy quantification: a repeatability analysis, where the repeatability of ^{1}H-MRS metabolite quantification within and across scanning sessions was assessed. The experiments and statistical tests showed high repeatability for each skeletal muscle metabolite using ^{1}H-MRS in healthy volunteers. This was achieved by having a proper set-up, which included reducing leg motion with extra padding, careful VOI placement, and a 30min rest period before scanning.

Once the reproducibility of ^{1}H-MRS was confirmed, further experiments were performed. As described in chapter 2.1, skeletal muscles have a high capacity to adapt to external demands/changes, such as diet and training, among others. Thus, before any metabolic assessments of exercised skeletal muscle, it was necessary to understand its metabolic profile at rest, specifically to understand if any differences would influence the results during exercise. This introduced the second question: are there any differences in the ^{1}H-MRS metabolic profile of subjects at rest? It was hypothesized that, if there were any differences, they would increase in athletes who performed more endurance vs. power training. This hypothesis was investigated in chapter An examination of the fiber composition of skeletal muscle using proton spectroscopy, where the skeletal muscle metabolic profile was characterized between predominantly endurance vs. power athletes. This chapter showed differences in the mean metabolite ratio between endurance vs. power athletes for carnosine, creatine, and the TMA complex. At the same time, there were no differences in EMCL and IMCL (lipids) metabolites.

After characterizing the ^{1}H-MRS metabolic profile of skeletal muscle at rest, the next step was to study it during exercise. Certain musculoskeletal diseases can impair the metabolic function of muscles, and these impairments can be amplified by comparing skeletal muscle biochemical environment before and after exercise. The main challenge with previous studies that have characterized the metabolic profile of exercised skeletal muscle is the lack of exercise standardization and the need to leave the MRI facilities to perform the exercise. This opens the opportunity to use other techniques, such as Electrical Muscle Stimulation (EMS), to study exercised skeletal muscle. This was the objective of Chapter An investigation of electrical stimulation exercise and its effects on metabolic changes by means of proton spectroscopy in healthy skeletal muscle, where an EMS protocol was used to study the metabolic profile in the lower leg using ^{1}H-MRS. Compared to voluntary exercise, the main advantage of using EMS is that it provides a repeatable and controlled exercise routine. This chapter showed no significant changes in the muscle metabolic profile pre vs post-electrical stimulation exercise protocol at the current EMS intensity. This suggests that ^{1}H-MRS is less sensitive to metabolic changes for the applied electrical stimulation protocol.

So far, the main interest of this work has been studying the metabolic profile of skeletal muscle by means of ^{1}H-MRS. Nevertheless, from Chapter 6, the use of EMS to exercise muscle was discouraged. As stated in Chapter 2.1, other molecules are highly involved in muscle metabolism, such as water or (de)oxy-Hb. These molecules could be indirectly studied utilizing MT or muscle BOLD, respectively. Altogether, the following steps were to use these three techniques (MT, BOLD, EMG) to study the metabolic environment of healthy skeletal muscle.

Integrating BOLD and EMG is challenging, as there are safety concerns due to the required hardware and induced artifacts from the MRI environment, such as the GA. This took the focus for the research in Chapter Simultaneous Studies of Muscle Blood Oxygen Level Dependent Signal and Electromyography: a safety and quality assessment analysis. The first part focused on performing a safety assessment of the required hardware to record EMG inside the MRI environment, showing no temperature or SAR risks to the volunteer during simultaneous acquisitions of BOLD-fMRI/EMG. The second part of this chapter focused on denoising the EMG recordings contaminated with the GA coming from the MRI during simultaneous acquisitions of BOLD/EMG. Results showed that the denoising procedure successfully removed the GA artifact. Furthermore, experiments showed that minimal hardware, software and data processing is required to denoise the EMG signal, potentially increasing the use of simultaneous acquisitions of BOLD-fMRI/EMG.

After concluding that employing simultaneous acquisitions of BOLD-fMRI/EMG was safe and provided high-quality results, the next step was to look at the water dynamics of skeletal muscle using MT. This technique is used to study the interaction between free and bounded tissue proton pools, which has been shown helpful in examining healthy and diseased skeletal muscle. As both water and O_2 are involved in muscle metabolism, it was expected that the joint of BOLD (looking at the relative concentration of (de)oxy-Hb during muscle activation) and MT (looking at water dynamics) would enhance the metabolic picture of skeletal muscle. This led to the last research Chapter Skeletal muscle metabolism assessment: a multimodal approach to understand water dynamics using Magnetization Transfer and muscle activation using Blood Oxygen Level Dependent Signal. This chapter aimed to assess the MT ratio in healthy volunteers pre vs post-exercise and correlate it with the BOLD response. This pilot study showed that the MT signal statistically decreased after exercise, and the percentage of change was linearly correlated to the BOLD response. This suggests that MT could potentially be used to study muscle metabolism, evaluate and differentiate muscle group recruitment during exercise, and classify healthy vs. diseased muscle.

9.2 Limitations

In addition to the particular limitations of each research chapter, this thesis presented the following general limitations:

- *Sample size*: it is recognized that the sample population is not ideal in some of the experiments presented. Unfortunately, the pool of participants available during this work was highly limited primarily due to COVID-19, as it caused restricted access to the MRI facilities because the project and myself were considered as 'non-essential' staff, limiting the MRI scanning uniquely to other graduate students. Even more, scheduling a comfortable time for our participants to be scanned was challenging as there was limited access to the MRI due to some indirect effects of COVID-19. The consequences of the limited pool of participants were:
    - *Sex balance*: ideally, all studies regarding humans should be sex-balanced (*i.e.* 50% males, 50% females) to account for any biological variability. Nevertheless, for the reasons mentioned above, the ability to consider sex balance in all the research chapters presented in this work was challenging, which could raise some issues in terms of the generalizability of our analysis and results.
    - *Power analysis*: to understand the minimum number of participants needed for an experiment, given a *significance, and power* value, a power analysis can be

done. As a quick example, for Chapter An examination of the fiber composition of skeletal muscle using proton spectroscopy, a power analysis was done for the mean metabolite differences between FT and ST groups for carnosine and creatine metabolites. The analysis yielded a sample size of 10 subjects per group for carnosine and 7 for creatine, *i.e.* around double the number of participants recruited in this Chapter.

Carnosine

```
##
##      Two-sample t test power calculation
##
##               n = 9.544483
##               d = 1.961161
##       sig.level = 0.01
##           power = 0.9
##     alternative = two.sided
##
## NOTE: n is number in *each* group
```

Creatine

```
##
##      Two-sample t test power calculation
##
##               n = 7.413123
##               d = 2.312589
##       sig.level = 0.01
##           power = 0.9
##     alternative = two.sided
##
## NOTE: n is number in *each* group
```

- *MRI studies on skeletal muscle of the lower leg*: an interesting observation during the literature review in this thesis was the tremendous amount of MRI research performed in the brain compared to skeletal muscle. Naturally, there are more tools available for data preprocessing and analysis optimized for the brain (FSL [1–3] and AFNI [4, 5]) than for skeletal muscle. The primary limitations encountered as an effect of this observation are:
  - *Muscle coregistration*: compared to the brain, there is no dedicated coregistration program or script to standardize skeletal muscle images to a standard space (such as the MNI space for the brain). Partially because there is no reference space or atlas of skeletal muscle, specifically of the lower limb. This hindered the use of voxel-by-voxel analysis and statistics in skeletal muscle.
  - *Muscle segmentation*: no reliable programs for automatic skeletal muscle group segmentation are available. Some articles have suggested deep learning algorithms approach [6, 7]. However, they have several limitations (reduced population size for testing, issues with small muscle volumes or fatty tissues), which discourages their daily use.

  These two factors forced the creation of manual segmentation of muscle groups using as reference an anatomical scan, such as the one shown in Fig. 2.3. As the main interest was muscle tissue, fat fascia and blood vessels were avoided as much as possible. However, identifying these areas on anatomical images was challenging on certain occasions, as their boundaries were unclear. This, in turn, increased the likelihood of human error while creating the muscle mask. This error was mitigated by creating conservative masks and eroding them before extracting any statistical maps.

- *Statistical tests*: as noted in the previous bullet point, one of the challenges was the lack of standardized skeletal muscle space to perform voxel-by-voxel comparisons. This was a noticeable issue in Chapter Skeletal muscle metabolism assessment: a multimodal approach to understand water dynamics using Magnetization Transfer and muscle activation using Blood Oxygen Level Dependent Signal, as there was a need to compare different scans (*i.e.* MT^{pre} vs. MT^{post}). The lack of a standard space forced the use of other statistical analyses to compare these scans. In this case, random clusters were taken for each muscle group, and the average value of each cluster was taken as an observation measured from that muscle. The random selection of clusters avoided any bias that could have been introduced during the cluster selection. Meanwhile, the averaging of these clusters is essentially the *Central Limit Theorem*, which indicates that the final distribution was approximately normal, a requirement for the statistical test performed in this thesis.

9.3 Future work

This work encompassed the use of ^{1}H-MRS, MT and BOLD to study the biochemical environment and function of skeletal muscle. Although the presented work is comprehensive, improvements and future work could still be made. Individual future work is listed within each research chapter, but this work has some general improvements. First, derived from the previously listed limitations, it would be ideal to recruit more participants for some of the research chapters presented in this work, specifically for the chapters aimed for publication (*i.e.* Chapter 5 and 7), as this would increase the significance of the presented results. In addition, the recruitment of more participants, especially females, would increase the sex balance of this work, thus reducing the possible biological bias in the results.

All of the work done so far has been at 40% MVC and under aerobic conditions. Although this is a good start, an exciting idea for the future would be to increase the % MVC, as the probability of causing muscle fatigue would increase. Furthermore, as aerobic metabolism is highly dependent on oxygen availability, a concept of particular interest that could have been applied in this work would be causing an oxygen deficit, as it would yield a preference for anaerobic metabolism. This has been done in previous research by using a pressure cuff. Unfortunately, the current HiREB-approved research protocol did not include this protocol, so this would be an idea for future work.

9.4 Conclusions

Skeletal muscle functional and metabolic features were explored and characterized through the development of this M.A.Sc. thesis. The MRI techniques used have not been utilized extensively to study skeletal muscle, but the use of the techniques and novel analysis approach is what makes this work unique. In this work, skeletal muscle was studied by looking at its:

A. Biochemical environment using ^{1}H-MRS, at rest, and during a series of EMS-induced exercise. Several metabolites of interest were investigated, such as Cr, EMCL, IMCL, Car and TMA. This research segment showed that (1) ^{1}H-MRS is highly reproducible in skeletal muscle despite its challenges due to the high structural organization of skeletal muscle, guaranteeing the quality of the metabolite quantification in ^{1}H-MRS. (2) EMS-induced exercise showed no changes in the ^{1}H-MRS spectra, pointing that ^{1}H is not as sensitive as other nuclei such as ^{31}P to track the metabolic changes of skeletal muscle during exercise. This suggests that the use of EMS as an alternative to voluntary exercise is not beneficial to study muscle metabolism employing ^{1}H-MRS at the current level of stimulation, but higher intensities of stimulation or increased exercise duration could demonstrate that EMS is of value. (3) It was demonstrated that Cr, Car, and TMA metabolites showed different ratios against water (used as the metabolite of reference) in power vs. endurance-oriented participants. These differences are attributed to the distinct metabolic, contractile and resistance characteristics of skeletal muscle groups. This result is particularly intriguing as the ability to differentiate between muscle fiber types is of interest in clinical applications, for example, for replacing muscle biopsy as a non-invasive method to identify muscle characteristics, which could help to diagnose and grade diseased muscle.

B. Water dynamics between the free and bounded pools using MT, to understand the evolution of water molecules pre vs. post voluntary exercise while simultaneously studying the blood flow and relative oxygen concentration by means of BOLD to characterize rested vs active skeletal muscle during a voluntary exercise protocol. This research piece showed that (1) the safety of participants was guaranteed during the experiments as all the extra hardware required for simultaneous studies of BOLD-fMRI/EMG were tested. (2) the GA arising during simultaneous studies of BOLD-fMRI/EMG is efficiently removed using the AAS algorithm, with no extra hardware, setup time, or software. This result is fully transferable to research and clinical studies as it proves that any MRI center can obtain high-quality simultaneous studies of BOLD-fMRI/EMG with minimal requirements. (3) the MT signal showed a decrease after exercise and was linearly correlated to the BOLD signal activation. Muscle BOLD was used as a frame of reference because this technique has been characterized in previous studies compared to the relatively unexplored MT technique. The ability of MT to distinguish between highly/lowly activated muscle groups during exercise opens the opportunity to non-invasively investigate muscle group recruitment with a higher spatial resolution (compared to EMG) and lower scanning times (compared to BOLD), making it a technique that is well suited for clinical use as exams need to be kept in the range of 15-30min. Metabolic diseases can disrupt normal metabolic pathways, causing an abnormal chemical environment in tissues that alters the interaction between free and bound water pools. Thus, MT scans hold potential as a technique that could be utilized in clinical studies for detecting these changes.

References

1. Jenkinson, M. *et al.* FSL. *NeuroImage. 20 YEARS OF fMRI* **62,** 782–790. doi:`10.1016/j.neuroimage.2011.09.015` (Aug. 15, 2012).
2. Smith, S. M. *et al.* Advances in functional and structural MR image analysis and implementation as FSL. *NeuroImage. Mathematics in Brain Imaging* **23,** S208–S219. doi:`10.1016/j.neuroimage.2004.07.051` (Jan. 1, 2004).
3. Woolrich, M. W. *et al.* Bayesian analysis of neuroimaging data in FSL. *NeuroImage. Mathematics in Brain Imaging* **45,** S173–S186. doi:`10.1016/j.neuroimage.2008.10.055` (Mar. 1, 2009).
4. Cox, R. W. AFNI: Software for Analysis and Visualization of Functional Magnetic Resonance Neuroimages. *Comput. Biomed. Res.* **29,** 162–173. doi:`10.1006/cbmr.1996.0014` (June 1, 1996).
5. Cox, R. W. & Hyde, J. S. Software tools for analysis and visualization of fMRI data. *NMR Biomed.* **10,** 171–178. doi:`10.1002/(SICI)1099-1492(199706/08)10:4/5<171::AID-NBM453>3.0.CO;2-L` (1997).
6. Ni, R. *et al.* Automatic segmentation of all lower limb muscles from high-resolution magnetic resonance imaging using a cascaded three-dimensional deep convolutional neural network. *J. Med. Imaging* **6,** 044009. doi:`10.1117/1.JMI.6.4.044009` (Oct. 2019).
7. Rohm, M. *et al.* 3D Automated Segmentation of Lower Leg Muscles Using Machine Learning on a Heterogeneous Dataset. *Diagnostics* **11,** 1747. doi:`10.3390/diagnostics11101747` (Sept. 23, 2021).

The end.